ANALYZING SYNERGISTIC EFFECTS OF COMBINED AGING ENVIRONMENTS ON POLYMER DEGRADATION: MICRO-MECHANICAL MODELING OF LOSS OF PERFORMANCE

By

Hamid Mohammadi

A DISSERTATION

Submitted to
Michigan State University
in partial fulfillment of the requirements
for the degree of

Civil Engineering - Doctor of Philosophy
Mechanical Engineering - Dual Major

2022

ABSTRACT

ANALYZING SYNERGISTIC EFFECTS OF COMBINED AGING ENVIRONMENTS ON POLYMER DEGRADATION: MICRO-MECHANICAL MODELING OF LOSS OF PERFORMANCE

By

Hamid Mohammadi

Materials' properties play a crucial role in the selection of processes or design for manufacturing system components. These components should have high resistance to multiple stress factors such as mechanical and environmental stresses in which the component is being used. For this reason, engineers should analyze all possible scenarios and try to model for combined environment conditions before introducing a product to the market.

Polymers are specific materials with significantly high durability and resilience due to their loosely cross-linked polymer matrix made by long interconnected polymer chains. Due to these excellent properties, they are among the most frequently used materials in load-transfer applications in adhesives, joints, sealing, bumpers, coatings, and protection shields. Due to the increasing use of composite materials in the industry, polymers' usage, especially in polymeric adhesive, drastically increased. Since polymeric adhesives are used to join dissimilar material interfaces. However, *degradation* of polymeric adhesives is a menace to joints.

Degradation or aging defined as the loss of properties due to environmental condition. Aging is an irreversible process that changes the network topology of the material. Polymeric adhesives are susceptible to degradation which makes them a critical part with extreme sensitivity to temperature, moisture, and sunlight. Degradation-induced failure occurs due to damage accumulated from mechanical sources and the loss of properties due to aging which cause a premature failure in system. Therefore, reliability of a system can be greatly compromised due to this degradation-induced failure. Consequently, polymeric adhesives are a significant challenge for design reliability of multi-material systems. Reliable theoretical models to predict the degradation-induced failure in polymeric adhesives can substantially reduce the cost and enhance the reliability of adhesive

bonding.

Current approach in Original Equipment Manufacturers (OEM) companies is to use experimental approaches to predict the failure. However, laboratory conditions omit many factors that are present in real-time and might not paint a clear picture of the mechanisms of failure. Most importantly, the time and cost needed for these tests are substantially high. To this end, developing a comprehensive software that would be able to model the real-time conditions of aging seems of great value.

This dissertation objective is to provide micro-mechanical constitutive models that would be able to model damage accumulation in polymers and polymeric adhesives during combined aging environments. These constitutive models provide the necessary modules to build a platform for creating a Finite Element Method (FEM) based model for a 3D modeling of polymers in combined environmental aging condition under mechanical stresses. To this end, the project followed four main steps namely, (I) performing accelerated aging tests, (II) analyzing the tests result to understand the underlying aging phenomena, (III) developing degradation model, (IV) validating the proposed model versus the experimental data. After successfully finishing these steps, the necessary modules to start creating an FEM platform would be ready which should be the next step for this project.

To go in further detail, this project successfully delivered five major tasks that has been defined as the necessary steps for developing the platform. These steps are as follows, (I) providing a model for thermo-oxidative aging of polymers, (II) understanding the effects of decay functions on modeling properties of aging, (III) developing a model for a combined thermo- and photo-oxidative aging, (IV) developing a model that can successfully consider accumulated damage during combined aging, (V) developing a model for cyclic environmental conditions. All of these models are the first ones in the literature that being developed which suggests great novelty and value that this work can bring to the industry. The model proposed in this work can significantly enhance the design process by allowing pre-selection of materials and product geometries with respect to the expected mechanical and environmental loading. Such process will allow agile design evaluation.

"This dissertation is dedicated to my wife, **Shiva**,
for her continued and unfailing love, support and understanding
during my pursuit of PhD degree, also
to my respectful parents and parents-in-law for always believing in me."

ACKNOWLEDGEMENTS

When I had started to write the acknowledgment, I have just realized how difficult a task it is to say “thank you” for all the help, support, and understanding, given by so many people over the time it took to write this dissertation. Thus, my fear is to forgot to acknowledge or under-represent the help of someone or a group. It is suffice to say, it took a great community to help me through completion of this work and the following names are just a few among them.

First of all, I want to thank my adviser, Dr. Roozbeh Dargazany. You helped me become an independent researcher. Thank you for taking a chance on me, I truly appreciate all your support.

Next, I would like to express my deepest appreciation to my committee members, Dr. Thomas Pence, Dr. Weiyi Lu, and Dr. Sara Roccabianca. Being privileged to use their rich experiences through out these years on top of having the honor of sitting in their classes had a major influence on my intellectual development as a graduate student.

I gratefully acknowledge the assistance of my dear peers and friends in the High-Performance Materials (HPM) group, especially Vahid Morovati, Amir Bahrololoumi, Yang Chen, Aref Ghaderi, Ramin Akbari, Sharif Alazhary, Mamoon Shaafaey and Abdo Korayem for sharing ideas, and helping through experimental procedures.

I cannot begin to express my thanks to Dr. Abdol-Hossein Esfahanian, who has been there whenever I needed guidance or help. I am forever grateful for your invaluable advice.

I wish I could name all my friends here, but thank you all for making my journey much more enjoyable and being a second family for me away from home. I wish you all the best in your future endeavors.

The completion of my dissertation would not have been possible without my best friend and my lovely wife Shiva Esfahanian. Her constant support, patience and sacrifice through all my travails, absences, fits of pique and impatience is truly praiseworthy. Furthermore, I am extremely grateful to my dear parents, parents-in-law, my siblings and their families, and specially to my sister and brothers-in-law.

TABLE OF CONTENTS

LIST OF TABLES

LIST OF FIGURES

CHAPTER 1

INTRODUCTION

1.1 Motivation

Materials' properties play a crucial role in the selection of processes or design for manufacturing system components. These components should have high resistance to multiple stress factors such as mechanical and environmental stresses in which the component is being used. For this reason, engineers should analyze all possible scenarios and try to model for combined environment conditions before introducing something to the market.

Polymers are specific materials with significantly high durability and resilience due to their loosely cross-linked polymer matrix made by long interconnected polymer chains. Due to these excellent properties, they are among the first material choices for engineers. Polymers are among the most frequently used materials in load-transfer applications in adhesives, joints, sealing, bumpers, coatings, and protection shields. Due to the increasing use of composite materials in the industry, polymers' usage, especially in polymeric adhesive, drastically increased. Since polymeric adhesives are used to join dissimilar material interfaces (composites to thin metal sheets).

Polymeric adhesives have many advantages compared to the more traditional methods of joining such as bolting, mechanical fasteners, welding, brazing, and others. Some of these advantages are listed in follows. The ability to join dissimilar material interfaces together: e.g., the joining of metals, plastics, rubbers, and composites. Fatigue resistance due to improved stress distribution in the joint. Improving design flexibility since wider choice of materials are available to the designer. Smooth, blemish-free, appearance of the bonded structure. Moreover, by one estimate, 70

pounds of adhesive can replace more than 200 pounds of mechanical fasteners. Therefore, they are widely used in industry, and they should be able to withstand different kinds of environmental and mechanical stressors. However, *degradation* of polymeric adhesives is a menace to joints. *Degradation or aging* defined as the loss of properties due to environmental condition. Aging is an irreversible process that changes the network topology of the material. Furthermore, one of the most frequent case of aging is oxidative aging which is the changes in topology of the material as the result of polymer chain scission and crosslinking due to reaction of polymer chains with oxygen. Polymeric adhesives are susceptible to degradation which makes them a critical part with extreme sensitivity to temperature, moisture, and sunlight. Degradation-induced failure occurs due to damage accumulated from mechanical sources and the loss of properties due to aging which cause a premature failure in system. Therefore, reliability of a system can be greatly compromised due to this degradation-induced failure. Consequently, polymeric adhesives are a significant challenge for design reliability of multi-material systems. Reliable theoretical models to predict the degradation-induced failure in polymeric adhesives can substantially reduce the cost and enhance the reliability of adhesive bonding.

Solar energy batteries are another important usage of polymers. The solar energy that reached the earth in one hour is more than the combined energy consumed by humanity in one year. Therefore, the total average usage of fossil-based energy can be reduced significantly if this energy can be harnessed. With the current energy issues, solar cells have become an attractive area of research. Currently, the global solar electricity market grosses approximately $\$10$ billion per year, with a 30% per annum growth rate.

The fossil fuels are the main source of energy due to hurdles of solar cell conversions and power per dollar ratio. Currently, polymer-based solar cells offer an economical option compared with the traditional inorganic semiconductor technology. The reason for this is the ease of process and design of polymers. Moreover, they offer more novel opportunities for design new devices and applications.

Although polymeric solar cells provided all these advantages, their stability still remain a prob-

lem. Degradation is a menace to many polymeric solar cells in ambient temperatures. However, most of the research thus far has been focused on increasing the efficiency of these cells. But, the focus should be applied on stability questions. Many variables affect the stability of polymeric solar cells such as oxygen, humidity, and light. Presence or absence of these variables can further define the mechanism of the degradation, including photo-oxidative degradation and combined thermo- and photo-oxidative oxidation.

Space industry is another important application of studying aging of polymers. Materials International Space Station Experiment (MISSE) is the name of the series of experimental studies that NASA has been doing for years in which they sent a batch of materials in space for real time degradation. These experiments showed that specifically in Low Earth orbit (LEO) environmental polymers will go under serious degradation due to the following threats:

- Solar radiation (ultraviolet (UV), x-rays)
- Charged particle radiation (electrons, protons)
- Cosmic rays (energetic nuclei)
- Temperature extremes & thermal cycling
- Micro-meteoroids & orbital debris (space particles)
- Atomic oxygen (AO) (reactive oxygen atoms)

These experimental data helped NASA to write the first Technical Standards Handbook "Spacecraft Polymers Atomic Oxygen Durability Handbook" (NASA-HDBK-6024). Yet still, there is an immediate need for precise models.

Current approach in Original Equipment Manufacturers (OEM) companies is to use experimental approaches to predict the failure. However, laboratory conditions omit many factors that are present in real-time and might not paint a clear picture of the mechanisms of failure. Most importantly, the time and cost needed for these tests are substantially high. To this end, developing

a comprehensive software that would be able to model the real-time conditions of aging seems of great value.

This dissertation objective is to provide a micro-mechanical constitutive models that would be able to model damage accumulation in polymers and polymeric adhesives during combined aging environments. This constitutive models provide the necessary modules to build a platform for creating a Finite Element Method (FEM) based model for a 3D modeling of polymers in combined environmental aging condition under mechanical stresses. To this end, the project followed four main steps namely, (I) performing accelerated aging tests, (II) analyzing the tests result to understand the underlying aging phenomena, (III) developing degradation model, (IV) validating the proposed model versus the experimental data. After successfully finishing these steps, the necessary modules to start creating an FEM platform would be ready which should be the next step for this project.

The ideal constitutive model would be the one that can model most of the complex inelastic behavior of the elastomer with the lowest number of material parameters. In order to understand inelastic features of rubber-like materials, extensive studies have been done during the last century [7, 8, 9, 10, 11, 12, 13, 14, 15]. The behavior of elastomers in cyclic deformation including uni-axial tension, compression and shear tests shows many complex and interesting features. Fig. 1.1 shows a typical stress-stretch behavior of filled rubbers under uni-axial cyclic loading. In a uni-axial tension, a considerable stress-softening is observed between the first loading and reloading (a phenomenon known as Mullins effect). The amount of this softening reduces in the subsequent cycle until it reaches a stabilized value, generally referred as hysteresis. In addition, after unloading, there is a time independent residual strain inside the material which is called permanent set.

Modeling efforts can be classified into two major types of formulation, depending on the approach followed by the authors to develop the strain energy function:

- The first kind of models are issued from mathematical developments of strain energy function such as the well-known Rivlin series [16] or the Ogden real exponents [17]. They are classically referred as phenomenological models. Material parameters can be challenging to

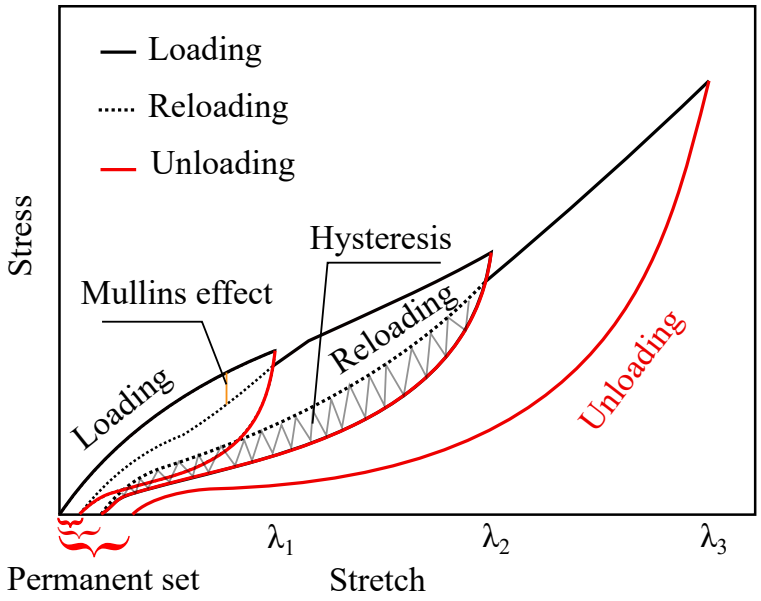

Figure 1.1. Schematics of stress-stretch behavior of the rubber-like elastomers under a uni-axial cyclic test. Inelastic effects such as Mullins effect, permanent set, and hysteresis has been marked.

determine.

- The second kind of models are those developed from physical motivation. Such models are based on both physics of polymer chains network and statistical methods. It leads to different strain energy functions depending on microscopic phenomena accounted for. Therefore, they are referred to as micro-mechanical models. These models use various concepts including the breakage of chains between the rubber and the fillers, slipping of molecules, cluster's rupture of fillers, chain disentanglement, and more complex composite structure formations [18, 19, 20]. In most of the cases, their mathematical formulation is quite complicated.

Lack of a proper micro-mechanical model for modeling constitutive behavior of elastomers motivated us to start this work in that direction. The main objective of this work is to provide a micro-mechanical model which has the capacity to describe the elastic and inelastic response of elastomers exposed to different aging environments. The proposed model will be based on the two concepts of dual network hypothesis [21] and network evolution [22, 23]. We assumed that the rubber matrix will be decomposed over time into two matrices; the original and the reformed network. The developed model demonstrates the changes in the rubber response as well as its

inelastic effects such as the Mullins effect and permanent set during the course of aging. In this work, we mainly focus on thermal and UV induced aging and study effects of different parameters on the material response.

To go in further detail, this project successfully delivered five major tasks that has been defined as the necessary steps for developing the platform. These steps are as follows, (I) providing a model for thermo-oxidative aging of polymers, (II) understanding the effects of decay functions on modeling properties of aging, (III) developing a model for a combined thermo- and photo-oxidative aging, (IV) developing a model that can successfully consider accumulated damage during combined aging, (V) developing a model for cyclic environmental conditions. All of these models are the first ones in the literature that being developed which suggests great novelty and value that this work can bring to the industry. The model proposed in this work can significantly enhance the design process by allowing pre-selection of materials and product geometries with respect to the expected mechanical and environmental loading. Such process will allow agile design evaluation, fast identification of critical zone, and extensive reduction in validation/verification of product performance against the durability standards. Moreover, by predicting the service life of polymers more accurately than before, the model can significantly improve the reliability of the current systems that are in use.

CHAPTER 2

BASICS OF CONTINUUM MECHANICS

The basics of continuum mechanics needed for describing the behavior of materials undergoing large deformation is briefly discussed in this chapter. These fundamental topics include geometric mappings, basic stress measures of a solid body, and first law of thermodynamics for constitutive relations. For a more comprehensive description and better understanding of the topic, the reader is encouraged to refer to continuum mechanics reference materials such as [24, 25, 26].

2.1 Some Notes on Continuum Mechanics

Since matter is formed from molecules which itself is consist of atoms and subatomic particles, it is not continuous. However, when it comes to considering special aspects of materials behaviors, such as deformation of structures under stresses, the rate of discharge of fluids from pipes due to pressure gradient, or even drag force experience by a body moving in air, they can be described independent of the matter molecular structure. The theory that tries to describe the material behavior by neglecting the structure of the material on a smaller scale is called *continuum theory*. Since Continuum theory regards the matter as continuous, it views the matter as infinitely divisible. Therefore, in this theory, there should be infinitesimal volume of materials referred as particles. It should be noted that due to continuity, there should always be neighboring particles in every neighborhood of a particle.

One of the most important requirements in the formulation for a physical law that should be satisfied by all quantities is that they should be coordinate invariant. Hence, continuum mechanics'

laws must be formulated in terms of coordinate invariant quantities. This permits any coordinate system to be used to represent these laws. The relation of various mechanical measurements are briefly reviewed in this section.

2.1.1 Deformation gradient

Fig. 2.1 shows a continuum body (B_{t_0}) in a 3D Euclidean space at the reference time (t_0). P_0 is an arbitrary point on B_{t_0} which can be represented by $\boldsymbol{X} \in \mathbb{E}^3$ with respect to an arbitrary bases. B_t is the body current configuration as it deforms in space through time. Considering that geometrical mapping of body from B_{t_0} to B_t is one to one, any point from reference configuration, P_0, uniquely maps to the current configuration, P, through arbitrary bases of $\boldsymbol{x} \in \mathbb{E}^3$.

The position of P and P_0 in any arbitrary coordinate system, $e^i\ (i = 1, 2, 3)$, can be represented by using the geometrical mapping of the regions of body from reference configuration B_{t_0} to the current configuration B_t as follows

$$\boldsymbol{x} = \hat{\boldsymbol{x}}(\theta^1, \theta^2, \theta^3, t), \quad \boldsymbol{X} = \hat{\boldsymbol{X}}(\theta^1, \theta^2, \theta^3) = \hat{\boldsymbol{x}}(\theta^1, \theta^2, \theta^3, t_0). \quad i = 1, 2, 3\ , \tag{2.1}$$

Therefore, the displacement vector, $\boldsymbol{u}$, of point P can be written as

$$\boldsymbol{u} = \hat{\boldsymbol{u}}(\theta^1, \theta^2, \theta^3, t) = \boldsymbol{x} - \boldsymbol{X} \tag{2.2}$$

Each point of the body can be demonstrated using a set of orthonormal (Cartesian) basis vectors, $\boldsymbol{e}_i \quad (i = 1, 2, 3)$, in an given Euclidean space as

$$\begin{aligned} &\boldsymbol{X} = X^i \boldsymbol{e}_i, \quad X^j = \boldsymbol{X} \cdot \boldsymbol{e}_j, && j = 1, 2, 3, \\ &\boldsymbol{u} = u^i \boldsymbol{e}_i, \quad u^j = \boldsymbol{u} \cdot \boldsymbol{e}_j, && j = 1, 2, 3, \\ &\boldsymbol{x} = x^i \boldsymbol{e}_i, \quad x^j = \boldsymbol{x} \cdot \boldsymbol{e}_j = X^j + u^j, && j = 1, 2, 3, \end{aligned} \tag{2.3}$$

where the Einstein notation, summation over repeated indices, is applied. Tangent vectors of suf-

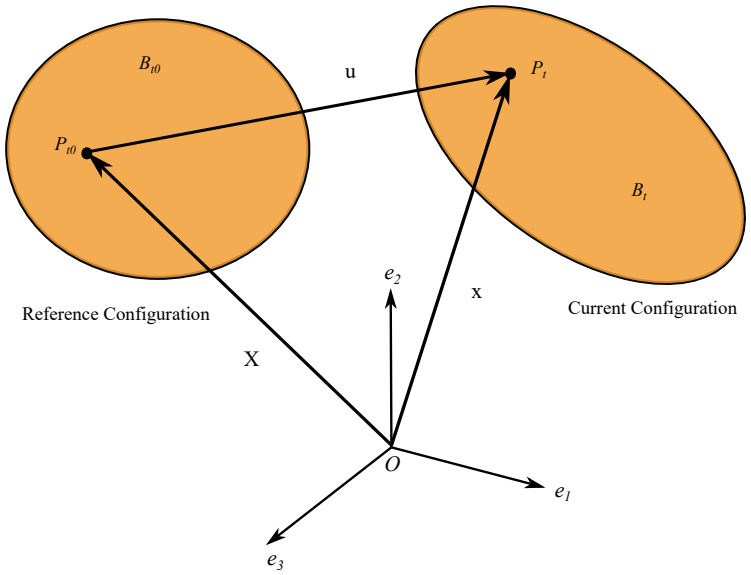

Figure 2.1. Deformation and motion of a continuum body.

ficiently differentiable coordinate lines in each of the configurations, $\boldsymbol{X}$ and $\boldsymbol{x}$, can be written as

$$\boldsymbol{G}_i = \frac{\partial \boldsymbol{X}}{\partial \theta^i} =, \qquad \boldsymbol{g}_i = \frac{\partial \boldsymbol{x}}{\partial \theta^i} \ , \quad i = 1, 2, 3 \ , \tag{2.4}$$

These tangent vectors can be related to the deformation. Using direction derivative, the relative motion of an arbitrary point with respect to its adjacent point in a direction $\boldsymbol{a}$ can be calculated as

$$\frac{d}{ds}\boldsymbol{x}\big(\boldsymbol{X} + s\boldsymbol{a}, t\big)\Big|_{s=0} = \lim_{\Delta s \to 0} \frac{\boldsymbol{x}\big(\boldsymbol{X} + \Delta s\boldsymbol{a}, t\big) - \boldsymbol{x}\big(\boldsymbol{X}, t\big)}{\Delta s} = \big(\mathrm{Grad}\ \boldsymbol{x}\big)\,\boldsymbol{a}. \tag{2.5}$$

Consequently, by using a linear mapping of vector $\boldsymbol{a}$ into vector $\frac{d}{ds}\boldsymbol{x}\big(\boldsymbol{X} + s\boldsymbol{a}, t\big)\Big|_{s=0}$, the second order deformation gradient tensor, $\big(\mathrm{Grad}\ \boldsymbol{x}\big)$, can be defined as

$$\mathbf{F} = \mathrm{Grad}\ \boldsymbol{x} = \frac{d\boldsymbol{x}}{d\boldsymbol{X}}. \tag{2.6}$$

where $d\boldsymbol{X}$ represents an infinitesimal element before deformation and $d\boldsymbol{x}$ shows the same element after deformation on the body. This tensor plays a pivotal role in describing the relative motion of material elements during deformation between reference and current configurations. Thus, this

relation can be described as follows

$$d\boldsymbol{x} = \mathbf{F}d\boldsymbol{X}, \quad d\boldsymbol{X} = \mathbf{F}^{-1}d\boldsymbol{x}. \tag{2.7}$$

Moreover, the change of volume and surface elements can be defined using deformation gradient as well. To this end, a volume in the reference configuration should be defined first. To do so, three non-co-planar vector, $d\boldsymbol{X}_1$, $d\boldsymbol{X}_2$ and $d\boldsymbol{X}_3$, can be used.

$$dV_0 = [d\boldsymbol{X}_1 d\boldsymbol{X}_2 d\boldsymbol{X}_3] = \big(d\boldsymbol{X}_1 \times d\boldsymbol{X}_2\big) \cdot d\boldsymbol{X}_3. \tag{2.8}$$

Using Eq. 2.7, each of these vectors can be represented in the current configuration as

$$d\boldsymbol{x}_1 = \mathbf{F}d\boldsymbol{X}_1, \quad d\boldsymbol{x}_2 = \mathbf{F}d\boldsymbol{X}_2, \quad d\boldsymbol{x}_3 = \mathbf{F}d\boldsymbol{X}_3. \tag{2.9}$$

Thus, the volume of the element in the current configuration can be written as

$$dV = \big[d\boldsymbol{x}_1 d\boldsymbol{x}_2 d\boldsymbol{x}_3\big] = \big(d\boldsymbol{x}_1 \times d\boldsymbol{x}_2\big) \cdot d\boldsymbol{x}_3 = JdV_0,$$

where

$$J = \frac{dV}{dV_0} = \left|\mathrm{F}^i_{\cdot j}\right| = \mathrm{det}\mathbf{F} > 0. \tag{2.10}$$

Additionally, by defining the surface element in reference and current state as $d\boldsymbol{A}_0 = d\boldsymbol{X}_1 \times d\boldsymbol{X}_2$ and $d\boldsymbol{A} = d\boldsymbol{x}_1 \times d\boldsymbol{x}_2$, respectively, the surface element in the current state can be calculated by substituting Eq. 2.9 into $dV_0 = JdV$ as

$$d\boldsymbol{A} = J\mathbf{F}^{-T}d\boldsymbol{A}_0. \tag{2.11}$$

where $dA = |d\boldsymbol{A}|$ and $dA_0 = |d\boldsymbol{A}_0|$ are the surface areas in the current and reference configuration, respectively. The length of an element in reference and current configurations can be calculated

similarly as

$$\|d\boldsymbol{x}\|^2 = d\boldsymbol{x}\cdot d\boldsymbol{x} = d\boldsymbol{X}\big(\mathbf{F}^{\mathrm{T}}\mathbf{F}\big)d\boldsymbol{X} = d\boldsymbol{X}\,\mathbf{C}d\boldsymbol{X},$$
$$\|d\boldsymbol{X}\|^2 = d\boldsymbol{X}\cdot d\boldsymbol{X} = d\boldsymbol{x}\big(\mathbf{F}^{-\mathrm{T}}\mathbf{F}^{-1}\big)d\boldsymbol{x} = d\boldsymbol{x}\mathbf{b}^{-1}d\boldsymbol{x}, \tag{2.12}$$

where $\mathbf{C} = \mathbf{F}^{\mathrm{T}}\mathbf{F}$ and $\mathbf{b} = \mathbf{F}\mathbf{F}^{\mathrm{T}}$ are the right and left Cauchy-Green tensors, respectively. The stretch of a material element, which is defined as the ratio of the length of the material element in current to the reference states, shows the change in the length of a linear element during deformation. Thus, the length of an element $d\boldsymbol{X}$ in direction $\boldsymbol{N}$ in initial state is changed to $d\boldsymbol{x}$ in direction $\boldsymbol{n}$ in the current state due to deformation and defined as

$$\begin{aligned}\lambda\big(\boldsymbol{N}\big) = \frac{dx}{dX} &= \sqrt{\frac{\|d\boldsymbol{x}\|^2}{\|d\boldsymbol{X}\|^2}} = \sqrt{\frac{dX\boldsymbol{N}\mathbf{C}\boldsymbol{N}dX}{dX^2}}\\ &= \big(\boldsymbol{N}\mathbf{C}\boldsymbol{N}\big)^{\frac{1}{2}},\end{aligned} \tag{2.13}$$

and

$$\lambda\big(\boldsymbol{n}\big) = \big(\boldsymbol{n}\mathbf{b}^{-1}\boldsymbol{n}\big)^{-\frac{1}{2}}. \tag{2.14}$$

Another measure of the change in element length during deformation can be written as

$$\begin{aligned}\|d\boldsymbol{x}\|^2 - \|d\boldsymbol{X}\|^2 &= 2d\boldsymbol{X}\,\mathbf{E}d\boldsymbol{X}\\ &= 2d\boldsymbol{x}\mathbf{e}d\boldsymbol{x}\end{aligned} \tag{2.15}$$

where $\mathbf{E} = \frac{1}{2}\big(\mathbf{C}-\mathbf{I}\big) = \frac{1}{2}\big(\mathbf{F}^{\mathrm{T}}\mathbf{F}-\mathbf{I}\big)$ called the Green-Lagrange strain tensor and $\mathbf{e} = \frac{1}{2}\big(\mathbf{I}-\mathbf{b}^{-1}\big) = \frac{1}{2}\big(\mathbf{I}-\mathbf{F}^{-\mathrm{T}}\mathbf{F}^{-1}\big)$ is Almansi strain tensor.

2.1.2 Deformation rate

Just as the deformation gradient one can define the material velocity gradient as

$$\mathbf{L} = \mathrm{Grad}\dot{\boldsymbol{x}} = \frac{\partial}{\partial \boldsymbol{X}}\left[\frac{\partial \boldsymbol{x}(\boldsymbol{X},t)}{\partial t}\right] = \frac{\partial}{\partial t}\left(\frac{\partial \boldsymbol{x}}{\partial \boldsymbol{X}}\right) = \dot{\mathbf{F}}. \tag{2.16}$$

As it can be seen the material velocity gradient is in reference configuration. The spatial velocity gradient is defined as the material velocity configuration in current configuration.

$$\mathbf{l} = \mathrm{grad}\dot{\boldsymbol{x}} = \frac{\partial \boldsymbol{v}}{\partial \boldsymbol{X}}\frac{\partial \boldsymbol{X}}{\partial \boldsymbol{x}} = \dot{\mathbf{F}}\mathbf{F}^{-1}. \tag{2.17}$$

where $\boldsymbol{v}$ is the spatial velocity field.

The spatial velocity gradient can further be decomposed to a symmetric $\mathbf{d} = \frac{1}{2}\Big(\mathbf{l} + \mathbf{l}^{\mathrm{T}}\Big)$ and an skew-symmetric part $\mathbf{w} = -\mathbf{w}^{\mathrm{T}} = \frac{1}{2}(\mathbf{l} - \mathbf{l}^{\mathrm{T}})$. The symmetric portion of the spatial velocity gradient is called deformation rate and is defined as follows

$$\mathbf{d} = \frac{1}{2}\Big(\mathbf{l} + \mathbf{l}^{\mathrm{T}}\Big) = \frac{1}{2}\Big(\dot{\mathbf{F}}\mathbf{F}^{-1} + \mathbf{F}^{-\mathrm{T}}\dot{\mathbf{F}}^{\mathrm{T}}\Big) = \frac{1}{2}\mathbf{F}^{-\mathrm{T}}\dot{\mathbf{C}}\mathbf{F}^{-1}. \tag{2.18}$$

In addition, the skew-symmetric part is called spin (vorticity) tensor and is defined as follows

$$\mathbf{w} = -\mathbf{w}^{\mathrm{T}} = \frac{1}{2}(\mathbf{l} - \mathbf{l}^{\mathrm{T}}) = \frac{1}{2}\Big(\dot{\mathbf{F}}\mathbf{F}^{-1} - \mathbf{F}^{-\mathrm{T}}\dot{\mathbf{F}}^{\mathrm{T}}\Big). \tag{2.19}$$

Green-Lagrange strain tensor rate, $\dot{\mathbf{E}}$, can be written as

$$\dot{\mathbf{E}} = \frac{1}{2}\dot{\mathbf{C}} = \frac{1}{2}\mathbf{F}^{\mathrm{T}}\mathbf{d}\mathbf{F}. \tag{2.20}$$

Volume change rate can be calculated by the time derivative of the determinant of the deformation gradient as

$$\dot{J} = \frac{\partial \det\mathbf{F}}{\partial t} = J\ \mathrm{tr}\mathbf{d} \tag{2.21}$$

2.1.3 Stress measures

Considering the neighbouring continuum points of a body, one can define an infinitesimal area, dA_0. Using this area, stress is defined by traction force vector dF_s per unit of area (see Fig. 2.2). The stress in each arbitrary point in reference configuration, P_0, and in its counterpart in the current configuration, P, is defined based on infinitesimal areas dA_0 and dA with the unit vectors of N and n normal to them, respectively. Therefore, the traction force and stress relation can be written as

$$d\boldsymbol{F_s} = \boldsymbol{T}dA_0 = \boldsymbol{t}dA, \tag{2.22}$$

where the vectors $\boldsymbol{T}$ and $\boldsymbol{t}$ are the traction force in reference and deformed configurations, respectively. Thus, using the Cauchy's stress theorem, second-order tensors $\boldsymbol{\sigma}$ and $\boldsymbol{P}$ can be demonstrated as

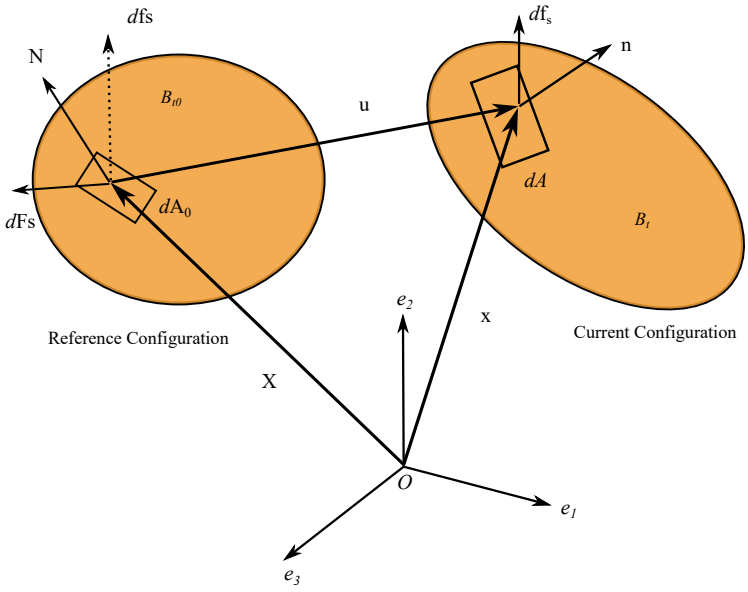

Figure 2.2. Continuum medium with a surface element and corresponding force vectors.

$$\boldsymbol{t} = \boldsymbol{\sigma n}, \quad \boldsymbol{T} = \boldsymbol{PN}, \tag{2.23}$$

where $\boldsymbol{\sigma}$ represents the Cauchy stress tensor which is related to force on the body surface in the current configuration while $\boldsymbol{P}$ is the first Piola-Kirchhoff stress tensor defined based on the surface area in initial configuration. Nanson's formula 2.11 and 2.23 relates the Cauchy stress tensor and the first Piola-Kirchhoff stress as

$$d\boldsymbol{F_s} = \boldsymbol{P}NdA_0 = \boldsymbol{\sigma}nd\boldsymbol{A} = J\boldsymbol{\sigma}\mathbf{F}^{-\mathrm{T}}Nd\boldsymbol{A_0}. \tag{2.24}$$

By mapping the force vector df_s in the current state to the reference configuration, one can calculate the second Piola-Kirchhoff stress tensor $\mathbf{S}$. Similarly, as it is indicated in the following equations, another spatial stress measure called the Kirchhoff stress tensor $\boldsymbol{\tau}$ can be calculated and converted to other measures as well.

$$\mathbf{P} = J\boldsymbol{\sigma}\mathbf{F}^{-\mathrm{T}} = \boldsymbol{\tau}\mathbf{F}^{-\mathrm{T}} = \mathbf{F}\mathbf{S}, \quad \mathbf{S} = J\mathbf{F}^{-1}\boldsymbol{\sigma}\mathbf{F}^{-\mathrm{T}}, \quad \boldsymbol{\tau} = J\boldsymbol{\sigma} \tag{2.25}$$

It should be noted that nominal/first Piola-Kirchhoff stress is not a symmetric tensor due to its two-point coordinate systems.

2.1.4 Balance principles

For a body B with mass M, volume V, and boundary surface A in the current state, linear momentum can be defined by

$$\int_M \boldsymbol{v}dM = \int_V \rho\dot{\boldsymbol{x}}dV,$$

where ρ is the density and $v = \dot{\boldsymbol{x}}$ is the velocity vector of a particle. The rate of change of the linear momentum is directly proportional to the forces applied on the body which can be calculated by summation of the body forces and surface forces as follows

$$\frac{d}{dt}\int_V \rho\dot{\boldsymbol{x}}dV = \int_V \boldsymbol{f}dV + \int_A \boldsymbol{t}dA. \tag{2.26}$$

Cauchy theorem (2.23) and divergence theorem can be used to obtain surface forces

$$\int_A \boldsymbol{t} dA = \int_A \boldsymbol{\sigma} \boldsymbol{n} dA = \int_V \operatorname{div} \boldsymbol{\sigma} dV. \tag{2.27}$$

By substituting Eq. 2.27 into Eq. 2.26, the balance equation is derived

$$\int_V \big(\operatorname{div}\boldsymbol{\sigma} + \boldsymbol{f} - \rho \ddot{\boldsymbol{x}}\big) dV = 0. \tag{2.28}$$

For any arbitrary point on the body, Eq. 2.28 can be rewritten as

$$\operatorname{div} \boldsymbol{\sigma} + \boldsymbol{f} = \rho \ddot{\boldsymbol{x}} \ . \tag{2.29}$$

In order to calculate the balance of mechanical energy, one can multiply Eq. 2.29 with the velocity vector $\boldsymbol{v}$ as

$$\boldsymbol{v} \cdot \operatorname{div} \boldsymbol{\sigma} + \boldsymbol{v} \cdot \boldsymbol{f} = \rho \boldsymbol{v} \cdot \ddot{\boldsymbol{x}}. \tag{2.30}$$

Considering the symmetry of the Cauchy stress tensor, Eq. 2.30 can be further simplified as

$$\boldsymbol{v} \cdot \operatorname{div}\boldsymbol{\sigma} = \operatorname{div} (\boldsymbol{v}\boldsymbol{\sigma}) - \boldsymbol{\sigma} : \operatorname{grad} \boldsymbol{v} = \operatorname{div} (\boldsymbol{v}\boldsymbol{\sigma}) - \boldsymbol{\sigma} : \mathbf{d}, \tag{2.31}$$

which gives

$$\operatorname{div}(\boldsymbol{v}\boldsymbol{\sigma}) - \boldsymbol{\sigma} : \mathbf{d} + \boldsymbol{v} \cdot \boldsymbol{f} = \rho \frac{d}{dt} \left(\frac{1}{2} \boldsymbol{v} \cdot \boldsymbol{v} \right). \tag{2.32}$$

Integrating Eq. 2.32 over the volume of the body and considering Eq. 2.27 yields

$$\frac{d}{dt} \int_M \left(\frac{1}{2} \boldsymbol{v} \cdot \boldsymbol{v} \right) dM + \int_V (\boldsymbol{\sigma} : \mathbf{d}) \, dV = \int_A (\boldsymbol{v} \cdot \boldsymbol{t}) \, dA + \int_V (\boldsymbol{v} \cdot \boldsymbol{f}) \, dV. \tag{2.33}$$

Eq. 2.33 can be represented as follow

$$\dot{K} + \mathcal{W} = \mathcal{P}, \tag{2.34}$$

where $\dot{K}$, $\mathcal{W}$, and $\mathcal{P}$ refer to the changes in the kinetic energy, the the stress power, and the power of external forces, respectively. The latter can be written as

$$\mathcal{P} = \int_A (\boldsymbol{v} \cdot \boldsymbol{t})\ dA + \int_V (\boldsymbol{v} \cdot \boldsymbol{f})\ dV. \tag{2.35}$$

The kinetic energy and the stress power of the system is then formulated by

$$\begin{aligned} K &= \int_V \left(\rho \frac{1}{2} \boldsymbol{v} \cdot \boldsymbol{v}\right)\ dV, \\ \mathcal{W} &= \int_V (\boldsymbol{\sigma} : \mathbf{d})\ dV. \end{aligned} \tag{2.36}$$

Finally, to complete the balance principles, one should define the energy dissipation as well. The total energy dissipation due to the deformation $\mathcal{D}$ can be obtained using the rate of stored energy per unit volume in the reference state, $\dot{\Psi}$, as follows

$$\mathcal{D} = \mathcal{W} - \int_{V_0} \dot{\Psi}\, dV_0. \tag{2.37}$$

2.1.5 Thermo-elasticity

Thermo-elasticity defines the relations between mechanical and thermal energy. It can be derived using the first and second laws of thermodynamics. The first law of thermodynamics states the energy conservation which can be formulated as

$$dU = dQ + dW. \tag{2.38}$$

where dU, dQ, and dW are the changes in the internal energy, the heat absorbed, and the work done on the system. The U and W can be demonstrated as

$$U = \int_V \rho \mathcal{U}\, dV, \quad \mathcal{W} = \frac{dW}{dt} \tag{2.39}$$

where $\mathcal{U}$ represents the internal energy density. Based on the second law of thermodynamics, the changes in the entropy of a reversible process (elastic deformation), dS at absolute temperature T is formulated as

$$dS = \frac{dQ}{T}. \tag{2.40}$$

Moreover, Helmholtz energy changed, $d\mathfrak{H}$, is described as

$$d\mathfrak{H} = dU - SdT - TdS. \tag{2.41}$$

At a constant temperature, Helmholtz energy changes represents the changes in the work done on the system $dW = d\mathfrak{H}$. The work done, dW, due to force f in the small displacement dl of solid-like structures can be written by

$$dW = fdl - p_h dV, \tag{2.42}$$

where p_h and dV denote the hydro-static pressure and the volume change. dV can be neglected in the case of incompressible material such as in elastomers. Thus, the force of an isothermal process can be derived using Eq. 2.41 and Eq. 2.42 as

$$f = \frac{dU}{dl} - T\frac{dS}{dl}. \tag{2.43}$$

The first part of Eq. 2.43 represents the volume change of the body or the energetic interactions of a single molecule [12]. However, experimental evidences suggest that in moderate and large deformations of elastomers, the contribution of energetic force in the total force is negligible . Therefore, entropy component is sufficient to approximate the force of the system as

$$f = -T\frac{dS}{dl}. \tag{2.44}$$

The Helmholtz free energy required to perturb the entropy of the system is

$$d\mathfrak{H} = -TdS. \tag{2.45}$$

2.2 Thermodynamic Consistency

The Clausius–Duhem inequality is a way of expressing the second law of thermodynamics used in derivation of the constitutive relation of materials to prove the relation is thermodynamically allowable. In other words, according to the second law of thermodynamic, elastic energy of the system mainly increases due to the decrease in entropy, therefore

$$\mathcal{D} \geq 0. \tag{2.46}$$

Thus, it is sufficient for a constitutive model to satisfy Clausius-Duhem inequality on all points of the body at any time to be thermodynamically consistent. In other words, during any thermodynamical deformation process, the energy balance should be satisfied. The energy balance can be calculated by substituting Eq. 2.38 to Eq. 2.34 as

$$\dot{K} - P = \frac{d}{dt}\left(U - Q\right) = \dot{U} - \dot{Q}, \tag{2.47}$$

where the thermal power $\dot{Q}$ is defined as

$$\dot{Q} = \int_V \rho\mathcal{Q}\, dV - \int_A \rho\boldsymbol{q}\cdot\boldsymbol{n}\, dA. \tag{2.48}$$

Where $\mathcal{Q}$ and $\boldsymbol{q}$ are the transferred heat and the surface heat flux per unit of mass, respectively. Furthermore, Eq. 2.47 can be rewritten as

$$\boldsymbol{\sigma} : \mathrm{l} = \rho\dot{\mathcal{U}} - \rho\mathcal{Q} + \mathrm{div}\,\boldsymbol{q}. \tag{2.49}$$

Thus, Clausius-Duhem inequality can be expressed by

$$\rho\mathcal{D} = \rho T\dot{\mathcal{S}} - (\rho\mathcal{Q} - \text{div}\ \boldsymbol{q}) \ \geq \ 0, \tag{2.50}$$

where $\mathcal{S}$ is the entropy density. By substitution of mass conservation ($\rho_0 = J\rho$) and energy balance law (2.49), Clausius-Duhem inequality can be simplified as follows

$$\mathcal{D} = T\dot{\mathcal{S}} - \left(\dot{\mathcal{U}} - \frac{1}{\rho_0}\boldsymbol{P} : \dot{\mathbf{F}}\right) \ \geq \ 0. \tag{2.51}$$

The internal variables, $\boldsymbol{\Omega}$, have been adopted to describe the history dependent dissipative effects in most of the constitutive models. Note that all the quantities of the Clausius-Duhem inequality, such as S, $\boldsymbol{q}$, and $\mathbf{P}$ should be functions of internal variables as well. Now, considering the stored energy density per unit of reference volume $\Psi = \hat{\Psi}\left(\mathbf{F}, T, \boldsymbol{\Omega}\right)$ as a function of these set of internal variables and substituting the Helmholtz free energy $\Psi = \rho_0\left(\mathcal{U} - T\mathcal{S}\right)$ into Eq. 2.51 results in

$$\rho J\mathcal{D} = -\dot{\Psi} - \rho J\mathcal{S}\dot{T} + \boldsymbol{P} : \dot{\mathbf{F}} \ \geq \ 0 \tag{2.52}$$

where $\dot{\Psi}\left(\mathbf{F}, T, \boldsymbol{\Omega}\right)$ can be calculated as

$$\dot{\Psi} = \frac{\partial\Psi}{\partial\mathbf{F}} : \dot{\mathbf{F}} + \frac{\partial\Psi}{\partial T}\dot{T} + \frac{\partial\Psi}{\partial\Omega} \cdot \dot{\boldsymbol{\Omega}}. \tag{2.53}$$

Eq. 2.52 can be rewritten with respect to Eq. 2.53 as

$$\rho J\mathcal{D} = -\frac{\partial\Psi}{\partial T}\dot{T} - \frac{\partial\Psi}{\partial\Omega} \cdot \dot{\boldsymbol{\Omega}} - \rho J\mathcal{S}\dot{T} + \left(\boldsymbol{P} - \frac{\partial\Psi}{\partial\mathbf{F}}\right) : \dot{\mathbf{F}} \ \geq \ 0. \tag{2.54}$$

For the case of isothermal process, Eq. 2.54 can be further simplified by considering a physical expression for the first Piola-Kirchhoff stress $\boldsymbol{P} = \frac{\partial\Psi}{\partial\mathbf{F}}$ which leads to an inequality of internal energy dissipation $\mathcal{D}$ as

$$-\frac{\partial\Psi}{\partial\Omega} \cdot \dot{\boldsymbol{\Omega}} \geq \ 0. \tag{2.55}$$

This inequality must always be satisfied during deformation over the body. For a more comprehensive review of thermo-elasticity, the reader is referred to [27, 28].

2.3 Incompressible Materials

Elastomers are widely assumed to be incompressible materials, meaning their volume does not change under applied deformation. Though it should be noted that they are not not truly incompressible, but incompressible enough thus the assumption of incompressibility holds. This is the equivalent of a linear elastic material having a Poisson's ratio close to 0.5. Elastomers' incompressibility condition should be considered in the constitutive modeling. Therefore, the internal energy function of an incompressible material is modified as

$$\Psi = \hat{\Psi}\left(\mathbf{F}, T, \mathbf{\Omega}\right) - p(J-1), \tag{2.56}$$

where p is a Lagrange multiplier to satisfy the boundary conditions and $J = \det\mathbf{F} = \frac{dV}{dV_0} = 1$ satisfies the incompressibility constraint. Now, the rate of the strain energy function, $\dot{\Psi}$, can be calculated as

$$\dot{\Psi} = \left(\frac{\partial\Psi\left(\mathbf{F}, T, \mathbf{\Omega}\right)}{\partial\mathbf{F}} - p\mathbf{F}^{-T}\right) : \dot{\mathbf{F}}, \tag{2.57}$$

where in order to satisfy the incompressibility condition, the rate of volume change considered to be zero, $\dot{V} = \dot{J} = 0$. Substituting Eq. 2.57 to Eq. 2.37, one gets

$$\left(\int_{V_0} \mathbf{P} dV_0 - \int_{V_0} \left(\partial_{\mathbf{F}}\hat{\Psi}\left(\mathbf{F}, T, \mathbf{\Omega}\right) - p\mathbf{F}^{-T}\right) dV_0\right) : \dot{\mathbf{F}} \geq 0. \tag{2.58}$$

For every deformation rate, $\dot{\mathbf{F}}$, Eq. 2.59 should be held true which leads to

$$\mathbf{P} = \frac{\partial\hat{\Psi}\left(\mathbf{F}, T, \mathbf{\Omega}\right)}{\partial\mathbf{F}} - p\mathbf{F}^{-T}, \tag{2.59}$$

Before using Eq. 2.59, one should understand the assumptions and the circumstances around this equation. This equation is valid for the case of

- Incompressible hyperelastic material
- Negligible contribution of internal energy in deformation
- Isothermal deformation
- Moderate and large range of deformation

CHAPTER 3

DEGRADATION

3.1 Introduction

Polymeric materials can be categorized in different ways. First, based on their origin, they can be classified as natural, synthetic, and semi-natural. However, it is more useful to categorize them based on their physical properties such as elastic modulus and degree of elongation. Based on this criterion, polymers can be classified as elastomers, plastics, and fibers [29]. Elastomers have long-range extensibility that is almost reversible at room temperature. Plastics characterized by partially reversible deformability while fibers have low extensibility with high tensile strength. Due to their high extensibility, elastomeric polymers have found extensive applications in industry.

In many applications, elastomeric components are expected to sustain cyclic loads and harsh environmental conditions for a long time. Design of such components is a challenging task since the mechanical, physical, and electrical behavior of elastomers change when they are exposed to various environmental conditions for a long time, a process generally known as *degradation or aging*.

Polymer science defines degradation as a complex process that causes a polymeric material to lose its original properties when exposed to the environment and workload [30]. Usually, a fundamental part of polymer degradation is the cleavage of macro-molecules. Thus, in a narrower sense, oftentimes the process of cleaving macro-molecules into fragments of various structures and sizes is referred to as polymer degradation [31]. It should be noted that if the final product are monomer(s), then the cleaving process is called depolymerization as it is the opposite of

polymerization [30] (see Fig. 3.1).

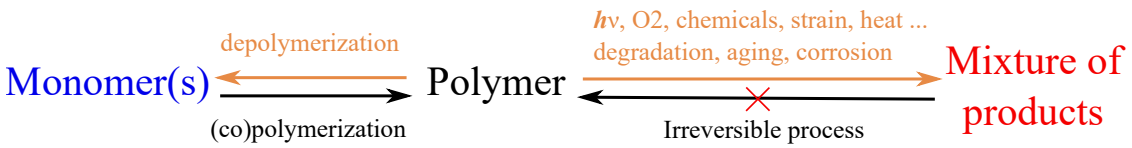

Figure 3.1. Different types of aging [3].

If the cleavage of macro-molecules is not the dominant process in the degradation, it is commonly called as polymer aging or corrosion [31]. Aging can be classified into different types based on their environmental source factor which are temperature, UV radiation (sunlight), and moisture. Accordingly, major types of aging are thermo-oxidative aging, photo-oxidative aging, and hygrothermal aging, respectively. Biodedradation is another notable source of degradation which induced by organisms, isolated enzymes or by a concerted action of natural environment [32] (see Fig. 3.2). Among these, thermo-oxidative aging is the most prevalent aging condition which is the focus of Chapter 4.

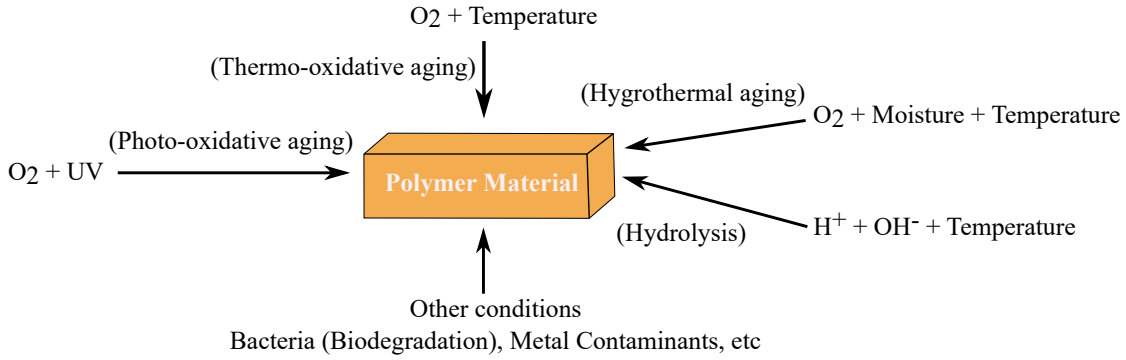

Figure 3.2. Different types of aging.

3.1.1 Initiated cleavage (degradation) of macro-molecules

Due to high activation Gibbs energy of the centers formation, a polymer without active centers is stable at temperatures significantly above its ceiling temperature $T_c \cong \Delta H_p/\Delta S_p$ (where $\Delta S_p < 0$ is polymerization entropy, and $\Delta H_p < 0$ is polymerization enthalpy). Note that by stable we mean kinetically stable since it is still thermodynamically unstable. After initiation, when active centers

are formed inside the polymer, the degradation will start. Thermal, photochemical, mechanochemical centers or the ones that are created by an oxidation process are the dominant active centers of degradation [3]. The type of polymer degradation is designated by these type of initiations.

3.1.1.1 Thermal Degradation

Temperature increase will accelerate conformational changes of macro-molecules by amplifying intra-molecular vibrations. The stress from these vibrations cause intra-chain chemical bonds to homolytically dissociate which increase the fragments with radical end-groups. These radicals, at $T > T_c$, allow depolymerization of the fragments due to reaction with the surroundings.

Under oxygen-rich environment, thermal oxidation plays a major role between T_g and around 200^o C. The thermal oxidation reactions and photo-oxidation reactions are very similar which are shown in Fig. 3.3. Initiation stage is the main difference between the two processes. While in thermal aging high temperature gives rise to bond dissociation, in photo-degradation, UV absorption initiates the chemical bond dissociation [4]. At temperatures higher than 200^o C, the covalent bonds of backbone chains can break due to pure thermolytic processes which causes huge mass loss. It can even char the polymer.

FTIR is one of the most common techniques in the study of thermal oxidation chemistry [33]. FTIR obtains the absorbance profile at different wave-numbers for the under-study material through shining beams consisting of different combinations of frequencies. Each bond in polymer has its own vibration wave-number. Therefore, chemical bond change of materials before and after aging can be inferred, by analyzing the absorbance change at different wave-numbers. These analyses have suggested that thermal oxidation of polymers can cause cross-linking reactions and chain-scission.

3.1.1.2 Photochemical Degradation

In a typical photochemical degradation, depending on the photon energy, there are different processes that might happen. Radiation may electronically excite and thus make some groups in the

polymer to be reactive (light, UV), or dissociate some polymers' bonds to produce radicals (UV, RTG), or eject an electron from the molecule (RTG, γ-rays) giving rise to radical-ions [34]. These photo generated species will depolymerize at $T > T_c$ and depending on the polymer structure and ambient conditions, they enter various subsequent reactions. These reactions result in the cleavage, crosslinking, modification of polymer molecules, or all of the mentioned outcomes. Under oxygen-rich environment, oxidation of the polymer will follow the photochemical initiation process and the overall complex process is called photo-oxidative degradation [31]. Photo-oxidative degradation will be studied extensively in Chapter 5.

UV portion of the solar spectrum plays a major role in degrading the mechanical properties of the polymer. The UV spectrum in solar radiation is categorized into three parts: UVA, UVB, and UVC. UVA has a wavelength ranging from $400nm$ to $315nm$, UVB is from $315nm$ to $280nm$, and UVC is the portion from $280nm$ to $100nm$. All the component of UVC and most of the UVB are filtered from reaching earth, due to the absorption of ozone layer and earth atmosphere. Thus, UVA rays plays a critical role on photo-degradation of polymers. The sensitivity of different polymers are different to UV wavelengths since the molecular structure affect the transition between the different energy levels. Presence of oxygen, such as in earth's atmospheric environment, enhance the detrimental effects of UV. The general photo-oxidative degradation mechanism of polymer includes the following steps [4]

Where PH is the polymer, $P^{\bullet}$ is the polymer radical, $H^{\bullet}$ is the hydrogen radical, O_2 is oxygen molecule, $PO^{\bullet}$ is the polymer oxy radical, $POO^{\bullet}$ is the polymer peroxy radical, $POOH$ is the polymer hydroperoxide, and $HO^{\bullet}$ is hydroxyl radical.

In the initiation stage, UV radiation leads to polymer absorption of high-energy photons, which in turn cause photolysis. This photolysis produces polymer radicals ($P^{\bullet}$). During the chain propagation stage with the help of oxygen, polymer radicals keep consuming polymer molecules (PH) and producing polymer hydroperoxide ($POOH$). In the branching stage, the UV unstable hydroperoxide ($POOH$) decomposes into polymer oxy radical ($PO^{\bullet}$) and hydroxyl radical ($HO^{\bullet}$). These polymer oxy radicals ($PO^{\bullet}$) are the main cause of chain scission (see Fig. 3.4). It is gen-

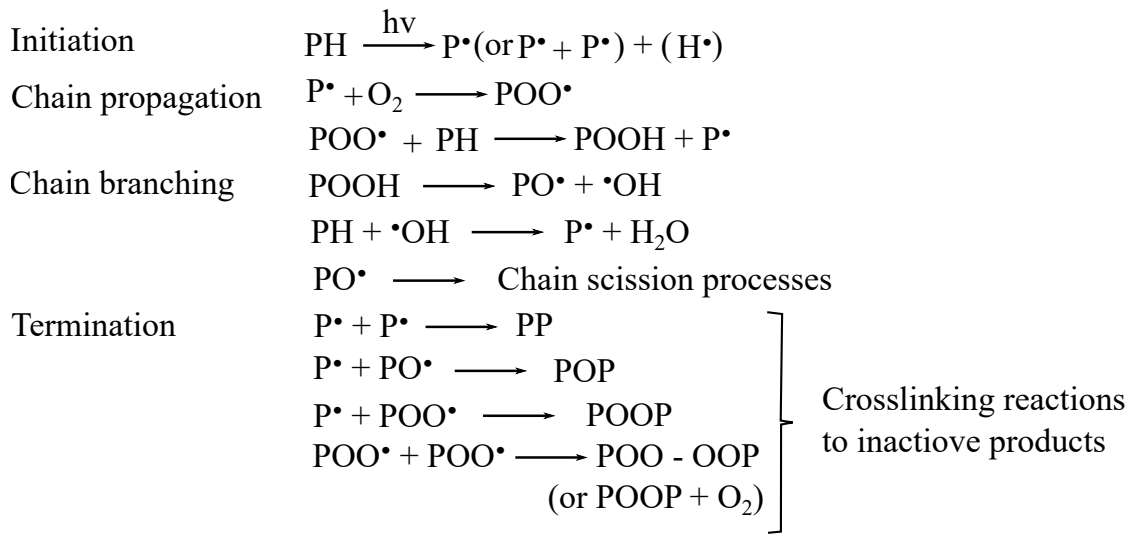

Figure 3.3. General schematic of photo-oxidative degradation mechanism of polymers [4]

erally accepted that the decomposition of polymer oxy radicals and formation of carbonyl groups ($c = O$) during this procedure is one of the main chain scission reactions. An example of the chain scission reaction is shown in Fig. 3.4:

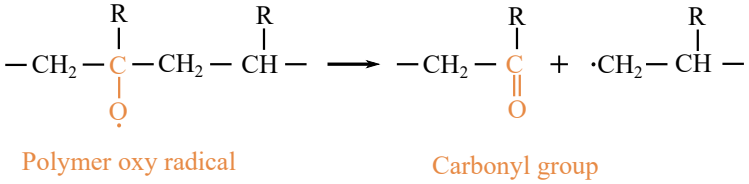

Figure 3.4. An example of scission reaction.

The process of radical recombination into inactive molecules is called termination stage. These reactions increase the chains crosslinking and the molecular length. This free radical mechanism applies to almost all types of polymers [4].

Based on the above mechanism, the effect of UV on polymer's mechanical properties can be described by the results of a competition between chain scission and crosslinking reactions. Generally, chain scission caused by photo-oxidation leads to shorter molecular chains which causes property degradation. Chain scission jeopardizes the mechanical and physical properties of a polymer system, such as reduction in strength, creation of micro-cracks, and discoloration. The cross-linking reactions have the opposite effect that increases the polymer properties. As the cross-links

increase, the Young's modulus and tensile strength will follow suit, but the polymer becomes brittle.

Due to the attenuation during UV penetration and oxygen diffusion, different depth of the material receives different UV intensity when exposed to UV radiation. Therefore, the change in material properties is not homogeneous in the bulk sample. Typically the most severe degradation is experience by the surface layers.

3.1.1.3 Mechanochemical Degradation

Breaking a rubber band actually means breaking a lot of chemical bonds of the original network macro-molecule. If sufficient mechanical work is supplied to a linear macro-molecule, it can break to two radical fragments under flow shear stress [35]. Small molecules can not be ruptured in this way. Efficient energy transfer by shear in flow is only possible on long molecules [31]. Consequently, in this degradation method, the mid-chain cleavage mode is common. An example of shear degradation application is in preparation of rubber mixture by calendering (a process for the production of film or continuous sheet by squeezing the molten polymer between a pair of heated counter-rotating rolls). Some rubbers contain large portions of macro-molecules. These macro-molecules prevent homogenization of the mixture due to high viscosity. Thus, degradation cause cleavage in these macro-molecules which significantly reduces the viscosity of the vulcanization mixture and therefore yield better homogenization of the mixture [36].

CHAPTER 4

THERMO-OXIDATIVE AGING

4.1 Introduction

Thermo-oxidative aging is induced by a combination of physical and chemical changes to the polymer matrix over time which directly affects its constitutive behavior and increases chances of early failure [37]. Aging can be either physical or chemical [38]. Physical aging does not affect the chemical structure of the material and only caused by the polymer chains movement. It can be reversed in sufficiently high temperatures [39]. One of the aspects of physical aging is stress relaxation due to viscoelastic properties of elastomers. Many authors work on the constitutive modeling of this behavior. Khan et al. [40] proposed a phenomenological constitutive model to characterize thermo-mechanical behavior of viscoelastic polymers. Moreover, there are many constitutive models on viscoelastic behavior of polymers [41, 42] in the literature, as well as many experimental results [43]. On the contrary, chemical aging is an irreversible process that change the network topology of the material. During chemical aging, the polymer matrix changes due to chemical reactions of polymer backbone with oxygen [37]. Two types of chemical reactions occur; (1) polymer scission and (2) new cross-linking which often leads to material embrittlement [44]. Both reactions highly affect the length distribution of polymer chains inside the matrix (see Fig. 4.1). Besides, aging also changes the morphology of the matrix. While the original cross-links are facilitated by sulphur links, the cross-links induced by aging have peroxide nature. Therefore, the behavior of aged samples are different than the virgin material. The relative rate of polymer chain scissions and cross-link formation determines whether the material should become ductile or

brittle, softer or harder. It is important to understand, even if these rates are equal hypothetically, the aged material would not have the same toughness as of the virgin material due to the loss of original cross-links. Since, chemical aging is dominant factor in the long run, it is the focus of current chapter.

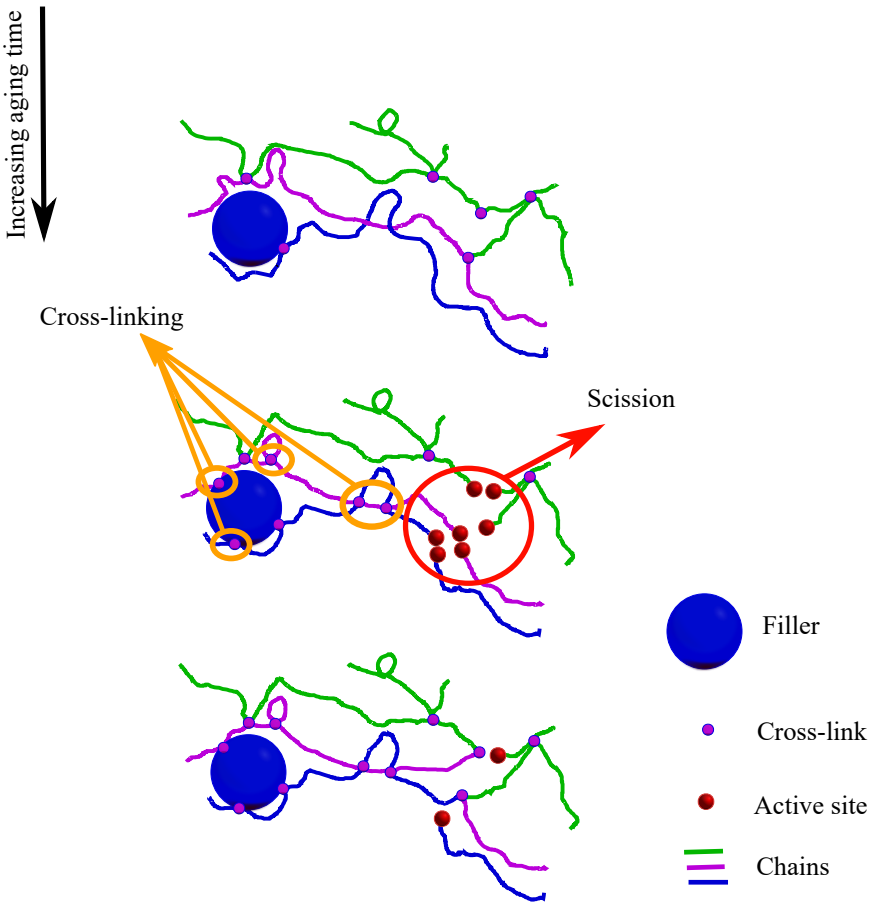

Figure 4.1. Schematic of chain scission and cross-linking processes.

Elastomeric parts in sensitive components may often be out of reach, where visual inspection is not possible. Hence, exact understanding of their service life reduction due to thermal aging is of utmost importance to prevent catastrophic failures. Such unexpected failures may have significant financial and environmental costs, such as Challenger space shuttle disaster. Considering the significant progression of thermal aging at elevated temperatures and its effect on decaying mechanical performance of rubber-like materials, different experimental and theoretical approaches were developed to predict the aging.

In experimental approaches, accelerated aging experiments at elevated temperatures are most popular method to estimate performance decay in service temperatures. Elevated temperatures causes the test to be done in a reasonable time, while emulating service condition may need years to make the effects of aging visible. Then, lifetime estimates at service temperature are often derived based on extrapolating accelerated aging results using Arrhenius relationship [45]. Although Arrhenius relationship shown success in predicting lifetime of elastomers in many cases [46, 47], Gillen et al. [6] raised serious problems regarding using it as a general guideline, since linear Arrhenius relationship cannot describe the observed aging data in many cases due to many factors. In elevated temperature, diffusion limited oxidation (DLO) occurs when the rate of oxygen consumption is higher than oxygen diffusion in the inner layer of matrix. DLO significantly reduces the progress rate of the aging, a feature which cannot be described by Arrhenius function [48]. Furthermore, Arrhenius function is relevant as long as only one mechanism is responsible for the decay. There are cases with different degradation processes in high and low temperatures resulting in variation of activation energy by temperature [49, 50, 51]. Thus, predictions based on non-Arrhenius relation is getting higher interest recently.

There are extensive experimental studies exclusively studying the effects of thermo-oxidative aging on the rubber-like materials using accelerated testing. Such works have been thoroughly reviewed in [5, 45]. In particular, several potential problems associated with accelerated testing methods were studied and reported in [52, 51, 53, 46]. An experimental study on the effect of aging on viscoelastic relaxation, oxidative scission, and thermal expansion of elastomers has been done by Shaw et al. [2]. Rabanizada et al. [54] examined the aging behavior of natural rubber in different media such as air, sea water, distilled water, and freshwater. They further studied the changes in dynamic behavior by means of dynamic mechanical analysis (DMA) tests. Similarly, Pazur et al. [55] studied the effect of thermal aging on bulk properties of peroxide-cured nitrile butadiene rubber (NBR). Their studies showed that understanding the distribution of the cross-link is necessary for comprehending the decay of bulk properties.

In comparison to experimental approaches, theoretical efforts are limited and can be mainly

categorized into two types of phenomenological and micro-mechanical approaches. Phenomenological approaches as mentioned in previous chapters are mostly based on a thermodynamic framework to describe the degradation of elastomers along with a mathematical relation to characterize mechanical behavior [56, 57]. Ha-Anh and Vu-Khanh [58] used an Arrhenius relationship along with Mooney-Rivlin model to predict hyperelastic behavior of aged polychloprene. Lion and Johlitz [39] proposed a three-dimensional phenomenological model to represent the chemical behavior of rubber. They split the Helmholtz free energy to three parts (volumetric material behavior, temperature-dependent hyper-elasticity, and a functional of deformation history) and added it to decomposition of deformation gradient. Their model were able to simulate the experimental data with excellent precision. Furthermore, Johlitz [59] presented a phenomenological model which was rheologically motivated. The model were able to predict both physical and chemical aging behavior. Later on, he presented a model based on finite strain theory and conducted experiments on aged automobile bearing to validate his simulation [1]. Dipple et al. [60] used a coupled chemo-mechanical modelling approach to analyze the aging behavior of an adhesive. They use finite element to simulate geometry dependency of aging between substrate and adhesive. In addition, Naumann and Ihlemann [61] simulated the effects of thermo-oxidative aging on mechanical behavior of rubbers by developing a new model. Their model were based on solving a coupled chemo-mechanical problem. To overcome the time scale difference in chemical and mechanical processes, they proposed an staggered solution algorithm. In their algorithm, the diffusion-reaction problem was solved in large time scale while the mechanical problem was solved intermittently for a defined load spectrum. They also proposed a dynamic network model instead of dual network model a year later [62]. Recently, Musil et al. [63] introduced a continuum mechanical approach to model chemical aging of NBR with regard to its viscoelasticity. Herzig et al. [64] modified reaction-diffusion equation to model heterogeneous aging due to DLO effect. His work showed the high dependency of adsorption, diffusion and reaction mechanisms to temperature. Similarly, Konica and Sain [65] proposed a model in a finite element framework that can analyze numerically the coupled diffusion-reaction and mechanical behavior of polymers undergoing oxidation.

Although phenomenological models can predict the behavior accurately, they can not provide an insight to the effect of material parameters on the behavior. This is due to the fact that their parameters usually comes from mathematical point of view instead of physical one. On the other hand, micro-mechanical models are based on statistical mechanics of polymer structure. Therefore, micro-mechanical model parameters do have physical meaning and come from material properties. Subsequently, a growing interest in micro-mechanical models is developing recently. Schlomka et al. [66] used the staggered solution algorithm presented in [62] along with a hyperelastic mechanical model of Neo-Hookean type to predict component stiffness. Mohammadi et al. [67, 68, 69] used micro-mechanical model based on network evolution and dual network hypothesis to predict the constitutive behavior of elastomers due to thermo-oxidative aging. Their model were able to model inelastic behavior such as Mullins effect and complex loading-unloading profiles. Despite the good agreement of the model with experimental data, the model was based on an an empirical decay function with no physical meaning. Later on they address this shortcoming by studying the effects of decay functions individually [70]. By a similar approach based on network evolution, Bahrololoumi et al. [71, 72] proposed a micro-mechanical model to predict the behavior of polymers going through hydrolytic aging. Recently, Beurle et al. [73] developed a micro-mechanical model for homogeneous aging of elastomers, by classifying the polymer chains into two categories of active and inactive chains. This splitting leaded to a set of coupled, non-linear ordinary differential equations that described the network degradation. They calculated the shear modulus of the material by solving these equations. Moreover, they implemented their concept into the matrix using the micro-sphere concept of Miehe et al. [74].

In this chapter, the necessary concepts to successfully model thermo-oxidative aging of elastomers are discussed. Later on, a micro-mechanical model is developed and validated with regard to experimental data that has been designed exclusively for the sake of thermo-oxidation benchmarking.

4.2 Design of Experiments

During aging, two types of chemical reactions happen, chain scission and cross-linking. Chain scission reactions break the chains and cause degradation of the original network. On the other hand, cross-linking reactions create a whole new polymer matrix. To separate the effect of these reactions and to understand the mechanical sources of thermo-oxidative aging, two types of tests has been used in literature, continuous relaxation test and intermittent test.

- Continuous relaxation test will be carried out to measure network degradation. Here, the specimens are stretched to specific level, and then stored at certain temperatures for aging. During aging, the stress is continuously measured (see Fig. 4.2 a). In continuous relaxation test (as shown in Fig. 4.2 a), a constant decrease in the stress is expected, a damage which occurs due to chain scission.

- Intermittent test will be carried out to characterize formation of a new aged network, by aging virgin samples in constant temperature for a certain time before testing. After aging, the mechanical performance will be characterized which may show stress softening, or hardening with time, although the latter is more prevalent (see Fig. 4.2 b).

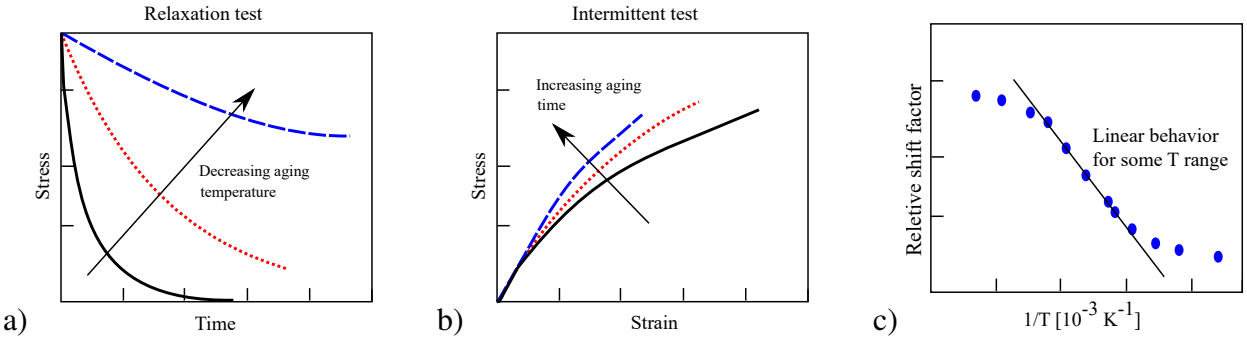

Figure 4.2. Schematic view of a) the relaxation test, and b) the intermittent test. c) Linear Arrhenius behavior and its range in most accelerated aging tests. Non-linear behaviour is expected when a larger temperature range is examined [5]

The rest of this chapter is outlined as follows. First, using the continuous relaxation test results, the concepts of dual network hypothesis and decay functions has been thoroughly discussed in

section 4.3. Then, using the decay function, dual network concept, and intermittent test results, a micro-mechanical model for the elastomer has been provided in sections 4.4-4.7.

4.3 Dual Network Hypothesis

Based on continuous relaxation test results, it is often assumed that in the course of aging, the polymer matrix will reach to a certain state where the virgin matrix is fully transformed into a new matrix, often with more numerous crosslinks. After this point, no further aging will occur at that stretch level. However, these assumptions are based on the homogeneous aging condition, the linear section in Fig. 4.2 c. The hypothesis agrees well with the experimental observations such as Fig. 4.2a where if we eliminate the effect of shrinkage, the stress will decrease till it reaches zero. Based on these observations, Tobolsky [21] offered the *dual network hypothesis*, where aging considered as the transition of polymer matrix from one state, virgin at time 0, to another state, aged at time infinity. Any other state in middle of these two states can be defined as a transition state between those two states. Accordingly, the strain energy of the polymer matrix, ψ_M, at each stage of aging can be simply represented with respect to energies of the network at those two states, namely Ψ_o and Ψ_∞.

$$\Psi_{\mathrm{M}} = \rho_o(t)\Psi_o + \rho_\infty(t)\Psi_\infty \tag{4.1}$$

where the strain energies of the original and totally aged networks are represented by Ψ_o, and Ψ_∞, respectively. Moreover, $\rho_o(t)$ and $\rho_\infty(t)$ represents the share of each network in the matrix with respect to time. Assuming $\rho_o + \rho_\infty = 1$, those two functions can be understood as shape functions to describe the transition between the two states Ψ_o, and Ψ_∞. Thus, they should satisfy continuity and completeness conditions. Subsequently, we have

$$\rho_\infty(t) = 1 - \rho_o(t) \quad \rightarrow \quad \begin{matrix} \rho_o(t=0) = 1 \\ \rho_o(t=\infty) = 0. \end{matrix} \tag{4.2}$$

Eq. (4.2) illustrates why $\rho_o(t)$ and $\rho_\infty(t)$ represent the decay and growth functions of the matrix, respectively. In all micro-mechanical models of aging, **understanding and deriving the decay function is an utmost important challenge** that needs to be handled with extreme care to satisfy the boundary conditions, the underlying assumptions and the behavior of the matrix in different tests. Fig. 4.3 shows an schematic view of dual network hypothesis, where the decaying nature of $\rho_o(t)$ can be seen here.

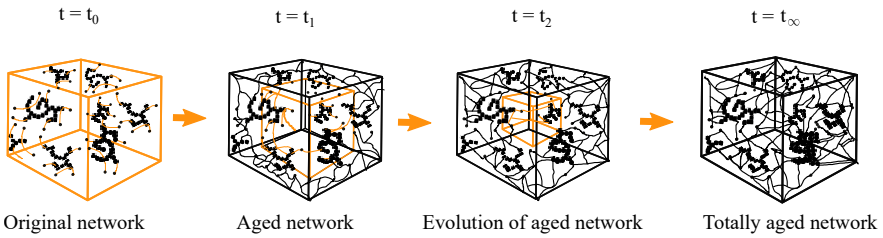

Figure 4.3. Evolution of second network through time (size represent the concentration of each network).

4.3.1 Decay functions

Kinetics of chemical reactions needs to be well-understood in order to define a decay function. The rate of chemical oxidation in the course of thermo-oxidative aging can be defined as [75]

$$-\frac{d\,[Z]}{dt} = k\,[Z]^m\,. \tag{4.3}$$

Where $[Z]$ is the concentration of chemical compound, Z, *k* is the reaction rate coefficient, and *m* is the reaction order. It should be noted that Eq. (4.3) is only meaningful for positive integers values of m [76]. Degradation chemical reactions are often described through first-order kinetic equations ($m = 1$) [77]. Moreover, by assuming homogeneous condition and assuming there is enough oxygen for the reactions to take place, *k* would be only a function of temperature according

to the famous Arrhenius function

$$k = \tau_0 e^{-E'_a} \quad \leftarrow \quad E'_a = \frac{E_a}{RT} \tag{4.4}$$

where $R = 8.314[JK^{-1}mol^{-1}]$ is the ideal gas constant, $\tau_0[s^{-1}]$ a pre-exponential factor, and $E_a[Jmol^{-}1]$ the activation energy of the chemical reaction.

Solving Eq.(4.3) for order 1 reactions and substituting it into Eq.(4.4), one can derive $[Z]$ through following equation, often known as *linear Arrhenius relationship*

$$[Z] = A_0 \quad exp\left(-\tau_0 e^{-E'_a} t\right). \tag{4.5}$$

Where A_0 and τ_0 are functions of temperature to satisfy Eq.(4.3). Since finding an accurate fitting function is challenging, it is more convenient to change them to constant fitting parameters. To do so, the concept of **time-temperature superposition** come in to play. Time-temperature superposition is based on the assumption that temperature can compensate the effect of time in aging. To this end, by plotting the degradation curves at different temperatures against log of the aging time, we should have identical curves just in different time-ranges. Thus, by shifting them through a constant multiplicative factor a_T, often known as horizontal shift factor, the behavior should be similar. This fact has been well documented by a series of experimental works by Celina et al. [78, 53, 46]. Accordingly, a master curve exists which can be considered as a basis to derive decay functions at different temperatures (see Fig. 4.4).

If the experimental data conform with time-temperature superposition approach, it means that no anomaly such as DLO or coupled chemical reactions are present. In that case, the time-temperature superposition approach can be applied to describe the experiments through following steps. First, one reference temperature should be selected, T_{ref}. Then, the time value of the data at the second temperature, T, should be multiplied by a shift factor, a_T such that these data gives the best overlap with the reference values. This shift factor would be determined empirically. If the

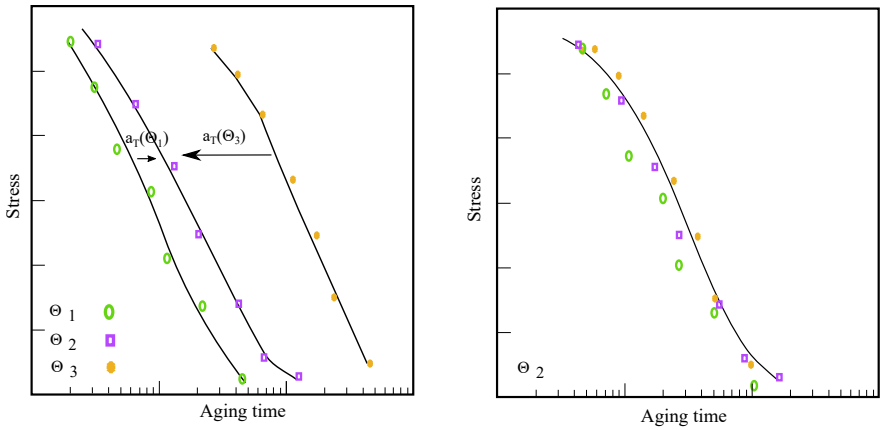

Figure 4.4. An schematic figure to represent time-temperature superposition concept (Based on [6])

data has Arrhenius behavior, then one simple approach is to represent the shift factors by a linear equation as given below[78, 47]

$$\log a_T = E'_a(\frac{T}{T_{ref}} - 1), \tag{4.6}$$

4.3.2 Nonlinear decay functions

Here, I will compare four possible decay functions and how well they can satisfy the aforementioned conditions in Eqs. (4.2), and (4.3). If we assume the decay function follow closely the chemical compound consumption, a simple decay function with few fitting parameters can be used to approximate the exact fitting function. My first proposal started with the linear Arrhenius relationship, as the most popular approach, for extrapolating material performance from one temperature to the other [45, 58]. Thus, the simplest form of a decay function with all the desired features would be a coupled combination of time-temperature superposition and linear Arrhenius function as follow

$$\rho_o(t|A_0, \tau_0) = A_0 exp\left(-\tau_0 e^{-\frac{E_a}{RT_{ref}}}(a_T t)\right), \tag{4.7}$$

where A_0 is the weight factor of decay function (which due to condition presented in (4.2), it is obvious that $A_0 = 1$), and τ_0 is a fitting constant.

In general, most accelerated aging tests are only relevant in the limited temperature range where Arrhenius function is linear (see Fig.4.2c). In a recent work, Celina[5] showed that the decay behavior should be considered nonlinear if the temperature range is wide. From chemo-mechanical aspects, decay in higher temperature ranges may engage several processes at the same time and thus, the kinetics of the involved mechanistic reactions should be taken into account to provide an accurate estimation of degradation rates. In particular, one needs to consider the effects of DLO [64] which is mainly caused by generalization of surface aging mechanisms to bulk aging such as thermo-oxidation and photo-oxidation ([79, 80, 81, 82, 83, 84]), and also the effect of glass transition and possible complications associated with it[85].

Many comprehensive studies in recent years on the aging behavior gave explicit support to insufficiency of linear Arrhenius relation [50, 86, 87, 51]. Thus, non-Arrhenius relations are getting more attention. Therefore, my second proposal for a decay function to approximate non-linear Arrhenius behavior would be a combination of two independent linear Arrhenius functions. These Arrhenius functions should both satisfy Eq. (4.3). Thus, they can be defined as

$$\begin{aligned} \rho_1 &= A_1 exp\left(-\tau_1 e^{-\frac{E_{a_1}}{RT}} t\right) \\ \rho_2 &= A_2 exp\left(-\tau_2 e^{-\frac{E_{a_2}}{RT}} t\right) \end{aligned} \tag{4.8}$$

Where E_{a_1} and E_{a_2} are activation energies for each reaction. I chose a linear combination of these two as my decay function. Using the same approach as the one for calculating Eq. (4.6), one can show that the same equation is still a possible solution for time-temperature superposition.

The only difference would be this time there should be two shift-factors as follow

$$\log a_{T_1} = \frac{E_{a_1}}{RT}(\frac{T}{T_{ref}} - 1), \tag{4.9}$$
$$\log a_{T_2} = \frac{E_{a_2}}{RT}(\frac{T}{T_{ref}} - 1).$$

Using these shift factors, the general form for our decay function with the linear combination of two Arrhenius functions would be as follow

$$\rho_o(t|A_1, \tau_1, A_2, \tau_2) = A_1 exp\left(-\tau_1 e^{-\frac{E_{a_1}}{RT_{ref}}}(a_{T_1}t)\right) + A_2 exp\left(-\tau_2 e^{-\frac{E_{a_2}}{RT_{ref}}}(a_{T_2}t)\right) \tag{4.10}$$
$$\rightarrow \quad A_1 + A_2 = 1$$

where A_1 and A_2 are weight factors of each Arrhenius function.

Any empirical function that satisfies the boundary condition and has a positive curvature can be considered as a possible decay function. It does not even need to be Arrhenius type. In the following, we offer some other decay functions and make a comparison for all of them. Note that for empirical decay functions, Eq. (4.6) will not hold anymore and shift factors should be calculated empirically too.

If we assume that thermo-oxidative aging can occur by two reactions, one of order 1 and the other of order 2. Meaning that in some reaction the rate of reaction is proportional to the concentration of the reactions and in the other one is proportional to the square of the concentrations. Then, by solving (4.3) for values of n equal to 1 and 2 and applying boundary conditions ((4.2)), following decay function can be suggested. It should be noted in this solution, I considered the rate of reaction, k ,for both of the reactions are constant.

$$\rho_o(t|A_1, \tau_1) = A_1 exp\left(-\tau_1 e^{-\frac{E_a}{RT}}(t)\right) + \frac{1}{\tau_1 e^{-\frac{E_a}{RT}}t + \frac{1}{1-A_1}} \tag{4.11}$$

Again, it can be shown as before that one possible solution for time-temperature superposition, would be using Eq. (4.6). This allows Eq. (4.11) to be rewritten as follow:

$$\rho_o(t|A_1,\tau_1) = A_1 exp\left(-\tau_1 e^{-\frac{E_a}{RT_{ref}}}(a_T t)\right) + \frac{1}{\tau_1 e^{-\frac{E_a}{RT_{ref}}}(a_T t) + \frac{1}{1-A_1}} \tag{4.12}$$

In another approach, Gussoni et al. [88] proposed the following decay function with physical based parameters for vibration of the chains. The similarity of this decay function to aging decay function seems worth attention. While the concept is different, we decided to define a similar decay function to check its performance in aging. In this decay function an empirical function for time-temperature superposition should be defined. Since, for a complex function as this, it would be a hard task to do, let's assume that Eq. (4.6) can be used for this function. Thus, the decay function would be

$$\rho_o(t) = A_1 exp\left(\frac{-a_T t}{T_2} - \frac{z M_2 (a_T t)^2}{2}\right) + A_2 exp\left(\frac{-a_T t}{T_2}\right) \quad \rightarrow \quad A_1 + A_2 = 1 \tag{4.13}$$

where all the parameters here are fitting parameters whereas in Gussoni model the parameters A_1 and A_2 represent the cross-links and dangling chain end, respectively. The parameter T_2 is the relaxation time, z the anisotropy parameter and M_2 is the second moment of bi-polar interactions.

To understand the relevance of these models, a numerical comparison between these decay functions is carried out by comparing them against experimental data of Johlitz et al. [1], and Shaw et al. [2]. Levenberg-Marquardt algorithm was used to derive the fitting parameters. Shift factor is the first parameter to fit. To define activation energies the data of lowest temperature for each data set, e.g. 60 °C and 100 °C, were shifted to next temperature, e.g. 80 °C and 125 °C, and the required shift factors for each decay function was derived. Then, I search for activation energies such that Eq. (4.6) or Eq. (4.9) yields the best approximation for the derived shift factors.

Next step would be fitting each decay function to the experimental data. Tables 4.1 and 4.2 provides the list of fitting parameters for each decay function and their corresponding values. These

values has been calculated based on the fitting the decay function to the relaxation data of [1] at 80 °C and [2] at 100 °C. The common approach is to fit to the highest temperature. However, here due to the thickness of the samples that has been used in these experiments [1, 2], the DLO effect at highest temperature would be an issue. Considering the proposed model is developed for homogeneous aging only, we chose the fitting temperature as to be high enough for accelerated aging and low enough to prevent DLO from affecting the results considerably. However, fitting the data to 100 °C and predicting lower temperature does not change the result significantly. The whole reason to choose these fitting temperatures was to avoid adding any unnecessary error to the predictions.

Table 4.1. Reference set of values for material parameters of Johlitz data set [1]

Equation number	E_{a1} $[Jmol^{-1}]$	E_{a2} $[Jmol^{-1}]$	A_0	A_1	A_2	$\tau_0[s^{-1}]$	$\tau_1[s^{-1}]$	$\tau_2[s^{-1}]$	$T_2[s]$	$zM_2[s^{-2}]$
(4.7)	93450	-	1	-	-	$8.896 *10^7$	-	-	-	-
(4.10)	114150	32417	-	0.8283	0.1717	-	$9.153 *10^{10}$	7.962	-	-
(4.12)	115500	-	-	0.9	-	-	$2.63* 10^{11}$	-	-	-
(4.13)	130000	-	-	0.194	0.806	-	-	-	$7.5 * 10^5$	$5 * 10^{-9}$

Table 4.2. Reference set of values for material parameters of Shaw data set [2]

Equation number	E_{a1} $[Jmol^{-1}]$	E_{a2} $[Jmol^{-1}]$	A_0	A_1	A_2	$\tau_0[s^{-1}]$	$\tau_1[s^{-1}]$	$\tau_2[s^{-1}]$	$T_2[s]$	$zM_2[s^{-2}]$
(4.7)	95900	-	1	-	-	$2.11 * 10^8$	-	-	-	-
(4.10)	10000	109000	-	0.36	0.64	-	$1.7* 10^{-3}$	$1.1* 10^{10}$	-	-
(4.12)	84000	-	-	$-4.3 * 10^{-5}$	-	-	$1.2* 10^7$	-	-	-
(4.13)	73000	-	-	2.3	-1.3	-	-	-	$5.7* 10^4$	$-5.5* 10^{-11}$

After fitting, each decay function has been used to predict the behavior of the material in relaxation test at 60 °C and 100 °C for Johlitz data set and at 100 °C and 125 °C for Shaw data set. Figures 4.5 to 4.6 show these predictions for Johlitz data [1] and Figures 4.7 to 4.8 show these

predictions for Shaw data.

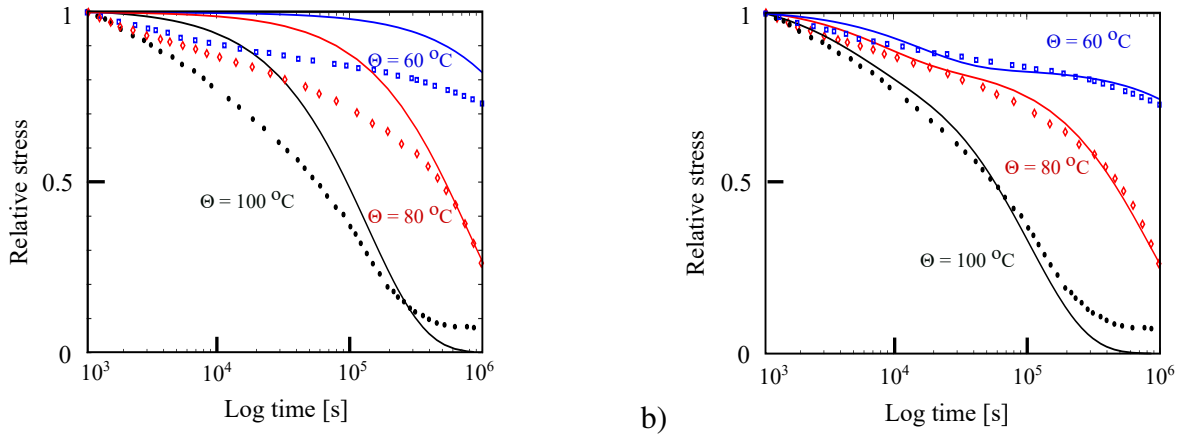

Figure 4.5. Relaxation data predictions a) using linear Arrhenius decay function, and b) using a combination of two independent linear Arrhenius decay functions.

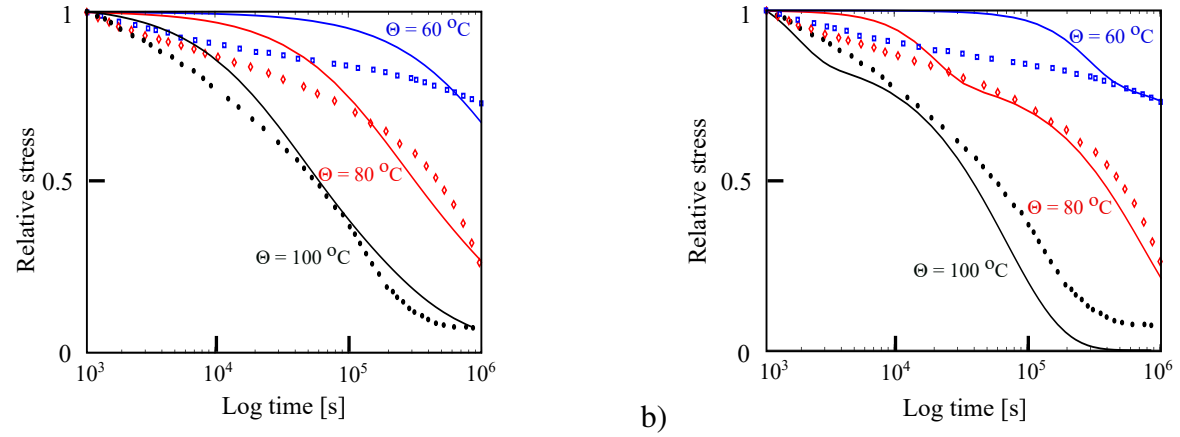

Figure 4.6. Relaxation data predictions a) using decay functions for two different order reactions, and b) using decay functions for Gussoni type reactions.

Tables 4.3 and 4.4 represent average error for each of these decay functions. As it can be seen from the results, the combination of Arrhenius functions yields the best result. For this function, average error for 60 °C and 80 °C are under 10% which is in the acceptable range. Although, the average error for 100 °C in Johlitz data [1] is much higher than acceptable range, the decay function is still usable since experimental data at this temperature is affected by DLO and are not accurate. In Shaw's data set [2], it can be seen that still the combination of linear Arrhenius functions yield the best result. The Average error in this set is higher which can be related to DLO effect as well. Since considering DLO effect is out of scope of this thesis, in the rest of the

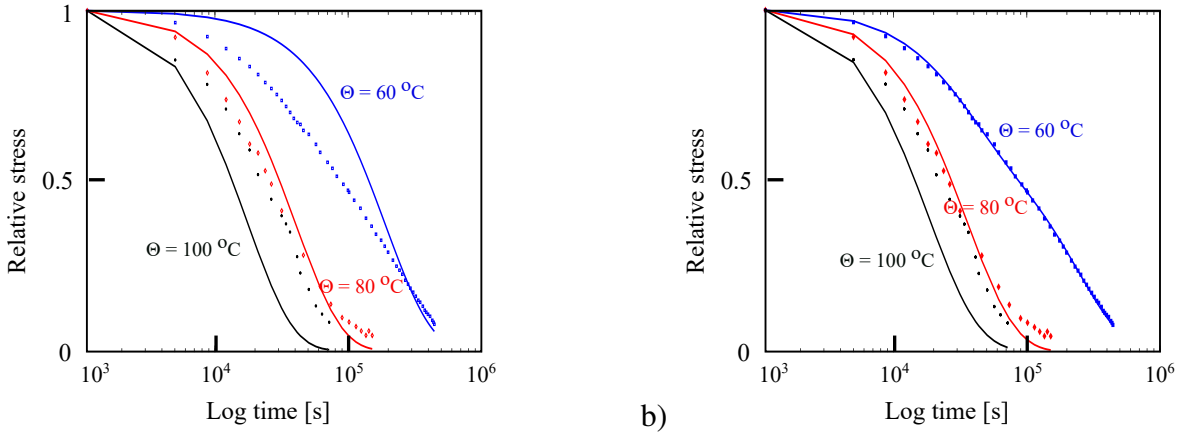

Figure 4.7. Relaxation data predictions a) using linear Arrhenius decay function, and b) using a combination of two independent linear Arrhenius decay functions.

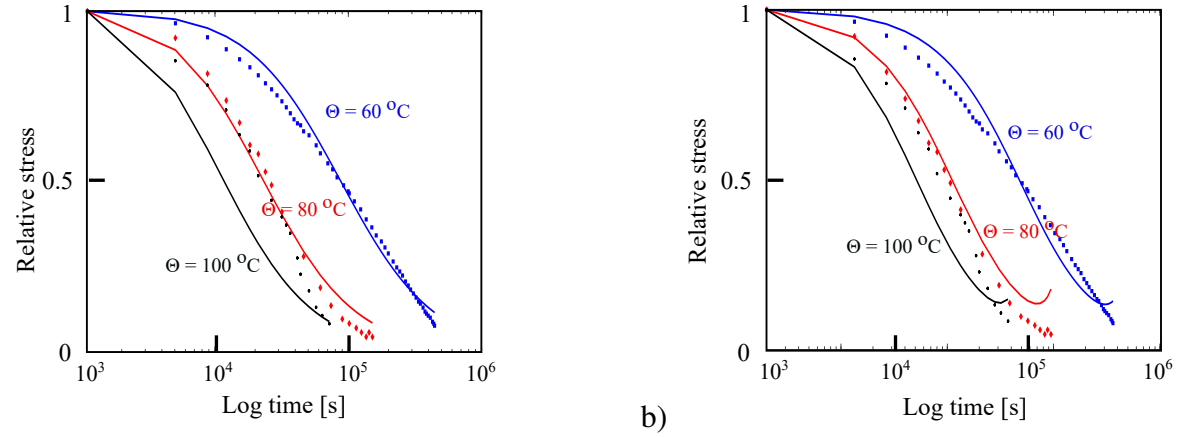

Figure 4.8. Relaxation data predictions a) using decay functions for two different order reactions, and b) using decay functions for Gussoni type decay function.

chapter, I will use combination of two independent Arrhenius functions as my decay function with the material parameters discussed in table 4.1.

Table 4.3. Fitting and prediction error values for Johlitz [1]

Decay function number	(4.7)			(4.10)			(4.12)			(4.13)		
Temperature [°C]	60	80	100	60	80	100	60	80	100	60	80	100
Average Error [%]	12.65	14.52	35.26	1.92	9.21	39.7	10	21	24	8.66	9.37	54

Table 4.4. Fitting and prediction error values for Shaw data set [2].

Decay function number	(4.7)			(4.10)			(4.12)			(4.13)		
Temperature [°C]	100	125	140	100	125	140	100	125	140	100	125	140
Average Error [%]	24	11	40	2.6	14	30	5	16	32	16	22	31

4.4 Statistical Mechanics of Polymers

Polymer molecules in rubber-like materials are bonded between aggregates and cross-link locations. Thus, the whole or a part of a polymer molecule limited between these constraints is called a chain. Each chain is consisted of *n* segments with the Kuhn length *l*. Let us consider the vector that connects two end of a chain by $\boldsymbol{r}$. The length of this vector, *r*, is referred as end-to-end distance, and hereafter, we use $\bar{r} = \frac{r}{l}$ as relative end-to-end distance.

Probability distribution function (PDF) of an isolated chain with n segments and relative end-to-end distance $\bar{r}$ in a dilute solution, i.e. the absence of other chains, can be estimated by $P(n\,|\bar{r}, q)$ which is derived based on the random walk theory [89, 90]. To consider the PDF of a chain in the presence of other chains, e.g. to consider the entanglement and cross-links, the following modified probability function has been introduced [91, 92], where the distribution function, $P\,(n) := P(n\,|\bar{r}, q\,)$ is given as follows

$$P\,(n) = P_0 \left(\frac{3}{2\pi n}\right)^{\frac{3}{2}} (1-q)^n \, exp\left(-\frac{3\bar{r}^2}{2n}\right). \tag{4.14}$$

Here, $q = \frac{N_{CL}}{N_{SG}}$ describes the cross-link density as the ratio between number of cross-links, N_{CL}, and the number of segments, N_{SG}. Since the number of available cross-link sites is always smaller than the number of segments, q should be smaller than 1. Therefore, $0 < q < 1$.

Considering q to represent the state of chemical reactions during aging, higher values of q show that the rate of chain detachment is lower than cross-linking and vice versa. During thermo-oxidative aging, if the temperature is high enough sulfur cross-linking is possible alongside peroxide cross-linking. Hence, in high temperature aging q usually increases through time till it reaches

its final value in a newly-formed aged network.

4.5 Strain Energy of the Matrix

Using the concept of micro-sphere [74, 93], each network is considered as a 3D composition of infinite 1D subnetworks [94, 22, 95]. The underlying assumptions are that each network is assumed to be homogeneous and isotropic, and chains are assumed to be spread equally in all directions. Since subnetworks can only sustain uniaxial deformation, they will experience different deformations based on their directions, $\overset{\boldsymbol{d}}{\lambda}$. Therefore, only a simplified form of entropic energy is needed to develop a model for the subnetwork in direction $\boldsymbol{d}$. Let's denote the parameter $\Psi(\overset{\boldsymbol{d}}{\lambda})$ as the energy of one subnetwork which is subjected to a direction-specific stretch. Then, the energy of a network can be calculated by 3D generalization of that subnetwork by integrating energies of subnetworks in all directions. Finally, the macroscopic energy of an arbitrary network, $\Psi_{\bullet}$, can be written as

$$\Psi_{\bullet} = \frac{1}{A_s} \int_{S} \overset{\boldsymbol{d}}{\psi}_{\bullet} d\overset{\boldsymbol{d}}{u}, \cong \sum_{j=1}^{k} \overset{\boldsymbol{d}_j}{\psi}_{\bullet} w_j. \tag{4.15}$$

where A_s is the surface area of a micro-sphere S, and $\overset{\boldsymbol{d}}{u}$ the unit area of the surface with the normal direction $\boldsymbol{d}$. Moreover, $\overset{\boldsymbol{d_j}}{\psi}$ denotes the strain energy of the ith sub-network in the direction $\boldsymbol{d}$. The parameters w_i are weight factors corresponding to the collocation directions $\boldsymbol{d}_i$ $(i = 1, 2, \ldots, k)$. To calculate the numerical scheme, the 90 integration points presented in [96] has been used. This scheme is selected as a result of trade off between numerical computational costs and the resulted error of the induced anisotropy [97]. The summation here shows that the constitutive behavior of the material is modeled by developing damage in a set of 1D chains. This method of modeling allows a non-uniform damage evolution in each subnetwork.

Energy of a Single Chain Using non-Gaussian distribution of a random walk problem, the free energy of a single polymer chain can be calculated. The Kuhn-Grün (KG) is the most significant approximation of the non-Gaussian theory of rubber elasticity. By combining the Boltzmann's entropy relation and thermodynamic balance, Kuhn-Grün approximation can be written as,

$$\begin{aligned}\psi_c\left(n,\bar{\boldsymbol{r}}\right) &= nk_BT\left(\xi\beta+\ln\frac{\beta}{\sinh\beta}\right)+c_0\\ &= nk_BT\int_0^{\xi}\beta\,d\tau+c_0,\end{aligned} \tag{4.16}$$

where k_B denotes the Boltzmann's constant, T is the absolute temperature and β is the inverse Langevin function (ILF) of the extensibility ratio, $\xi=\frac{\bar{r}}{n}=\mathcal{L}(\beta)=\coth\left(\beta\right)-\frac{1}{\beta}$. To eliminate the free energy in reference configuration, c_0 is added.

The KG model is derived based on the assumption that the chains are sufficiently long (about 5% relative error for $n=40$) [98, 90]. Thus, KG approximation cause considerable error with respect to exact theory for short chains. An enhanced KG is developed recently with much higher accuracy for shorter chains, which is given by [99]

$$\begin{aligned}\hat{\psi}_c\left(n,\bar{r}\right) &= nk_BT\int_0^{\xi}\hat{\beta}\left(\tau;n\right)d\tau,\\ \hat{\beta} &= \left[1-\frac{1+\xi^2}{n}\right]\beta.\end{aligned} \tag{4.17}$$

Since ILF cannot be derived explicitly, it has been approximated by rational functions or calculated implicitly. Here, an approximation presented by Morovati et al. [98] has been used. Based on this approximation, ILF is calculated through a first order fractional approximation with two polynomial terms (relative error of 1.0%) as

$$\mathcal{L}^{-1}\left(x\right)\cong\frac{1}{1-x}+x-\frac{8}{9}x^2. \tag{4.18}$$

4.6 Network Evolution

In the previous section, the evolution of an aging network within the polymer matrix has been described. In this section, the concept of network evolution [100] will be presented. Network evolution deals with the deformation induced phenomena such as stress softening and permanent set.

According to this concept, damage will be described as the competition between two simultaneous processes named polymer detachment and network rearrangement. In the following, these two processes with their contributions to the mentioned effects will be discussed.

4.6.1 Polymer detachment

Consider a set of polymer chains constrained between two crosslinks or aggregates or a combination of two (see Fig. 4.9). Let us denote the averaged inter-aggregate distance in the virgin and elongated network by r_0, and $\lambda_1 r_0(\lambda_2 r_0)$, respectively, where $\lambda_1 < \lambda_2$ represent micro-stretches in the inter-aggregate direction $\boldsymbol{d}$. In the course of deformation, the polymer chains begin to slide on or debond from the aggregates or crosslinks. This debonding starts with the shortest chain and gradually involves longer and longer chains.

The strength of monomer bonds within polymer chains is far higher than that of polymer-filler bonds. Thus, even at large strains polymer chains do not break but rather slide from their bonding sites on the aggregate surface. During consequent unloading, the distance between aggregates again decreases. However, the debonded chains do not reattach back to the aggregates surface. Thus, the maximal micro-stretch λ_m previously reached in the loading history is crucial for the description of the polymer-filler debonding.

In order to formalize the sliding process, we consider Fig. 4.10, in which the distribution profile of polymer chains with initial relative distance $\bar{r_0}$ is plotted versus the number of segments n. The dotted diagram illustrates how the applied force, $F\left(n, \bar{r}\right) = \frac{\partial \psi}{\partial r}$, increases as the length of the chains decreases. Clearly, this force tends to infinity as the length of the chains, nl, becomes close to its end-to-end distance $\bar{r_0}$. It should be noted that since end-to-end distance in totally aged

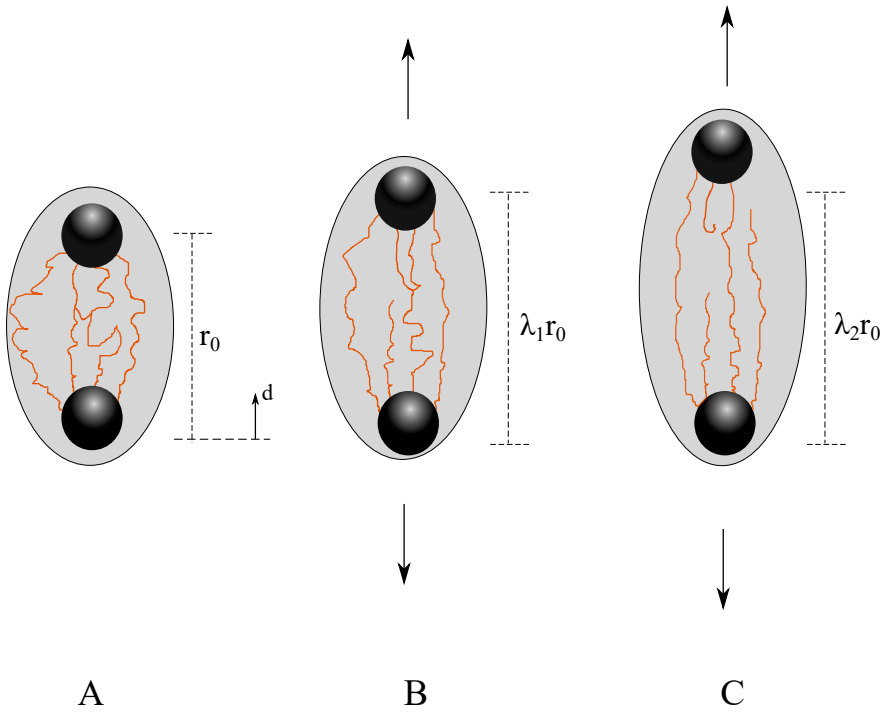

Figure 4.9. Illustration of detachment of shorter chains during primary loading.

network, $\bar{r}_{0\infty}$, is different than original network, $\bar{r}_{0o}$, the set of available chains differ from original to totally aged network.

The debonding or the sliding takes place if the force magnitude exceeds the effective interaction strength of polymer-filler bonds denoted by F_0^{eff} and F_∞^{eff}. This force is achieved when a chain reaches its maximal length which is expressed as $\nu\lambda_m\bar{r}_0$ where $\nu > 1$ is a material parameter that denotes a sliding ratio.

Chains whose length exceeds some upper limit could not be placed between the aggregates even from the purely geometrical point of view. First, the Gaussian distribution function of chains between two aggregates does not take into account the finite volume of the molecules which becomes relevant for long chains. Second, the probability of a long chain between two aggregates without intermediate bounds to their active sites is considerably less than the predicted value. Third, aggregates represent rigid geometrical obstacles for chains paths which are not considered by the Gaussian distribution but, considerably reduce the probability of long chain paths. Furthermore, long chains will probably intersect themselves and build internal crosslinks whose contribution is

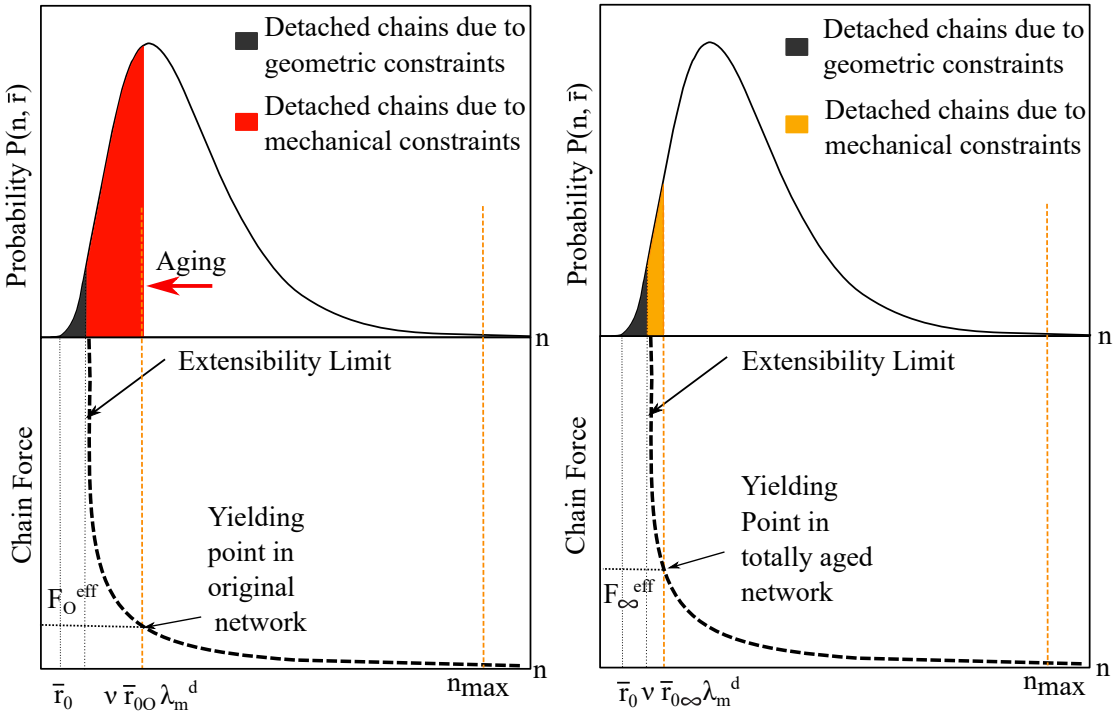

Figure 4.10. Distribution function and force developed by chains with an equal initial relative end-to-end distance $\bar{r_0}$ and pre-stretched by λ_m (mechanical constraint).

taken into account by the rubber network contribution. This justifies the assumption of the relative length upper limit n_{max} of chains connecting two aggregates. For simplicity n_{max} assumed to be constant in both networks.

Accordingly, the set of available relative lengths of chains bounded to aggregates in the direction $\boldsymbol{d}$ can be expressed by

$$D_o\left(\begin{matrix}\boldsymbol{d}\\ \lambda_m\end{matrix}\right)=\left\{n\,\middle|\,\nu\lambda_m^{\boldsymbol{d}}\bar{r}_{0o}\le n\le n_{max}\right\}\quad D_\infty\left(\begin{matrix}\boldsymbol{d}\\ \lambda_m\end{matrix}\right)=\left\{n\,\middle|\,\nu\lambda_m^{\boldsymbol{d}}\bar{r}_{0\infty}\le n\le n_{max}\right\}\qquad(4.19)$$

where maximum micro-stretch in direction d has been shown by $\lambda^{\boldsymbol{d}}{}_m$. It should be noted, the maximum stretch in each direction would not necessarily be the same in two networks.

We define $\lambda^o=\lambda_{rel}\lambda^\infty$ since the second network will be formed in the current configuration as a stress-free network, and thus take the current configuration as its reference point. Accordingly, by loading a sample that has been stored and aged at a certain pre-stretch level, we apply differ-

ent stretches on its two networks. This can be illustrated through two realistic aging conditions, relaxation and intermittent tests, as follow.

Relaxation test: In the case of relaxation test, the samples will be stored at a defined stretch, λ_{rel}, for a certain time. Thus, λ_{rel} would be equal to λ^o and obviously $\lambda^b = 1$. This satisfies the condition that totally aged network should be created stress-free and should not contribute to the stress-stretch relation at the storage pre-stretch. This is one of the fundamental assumptions of dual network hypothesis. This assumption is based on the idea that the new totally aged network does not have any directional preferences. Consequently, its chains' lengths should be constant for all directions. Therefore, we assume that all directions will have the same maximum damage as those in the principle directions and accordingly D_∞ can be rewritten as

$$D_\infty \left(\overset{\boldsymbol{d}}{\lambda_m} \right) := max \left(\lambda_{rel}, \overset{\boldsymbol{\infty:d}}{\lambda_m} \right), \tag{4.20}$$

where $\overset{\boldsymbol{\infty:d}}{\lambda_m}$ is the maximum stretch of a totally aged subnetwork in the direction $\boldsymbol{d}$.

Micro-sphere concept can paint a clear picture for this case. Based on this concept, at the beginning (point A in Fig.4.11) we have only unaged network in stress free state. Next, we stretch the virgin sample and put it inside the chamber (point B in Fig.4.11). At this stage, we still only have original network at stretched state which can be imagined as an ellipsoid with different stretches in different directions. During aging, the stretched original network will diminish while the aged network will be formed as an sphere at λ_{rel} (point C in Fig.4.11). Finally, after sufficient time passes, only totally aged network remains which is the new stress free state of the material (point D in Fig.4.11).

It would be noteworthy to look at evolution of λ_{max} during relaxation test as illustrated by Fig. 4.12.

Intermittent test: In this case, samples will be stored at reference configuration at a constant temperature. After certain time, they will be cooled down to room temperature and uniaxial tensile tests will be carried out on aged samples. In this case, since the totally aged network is created

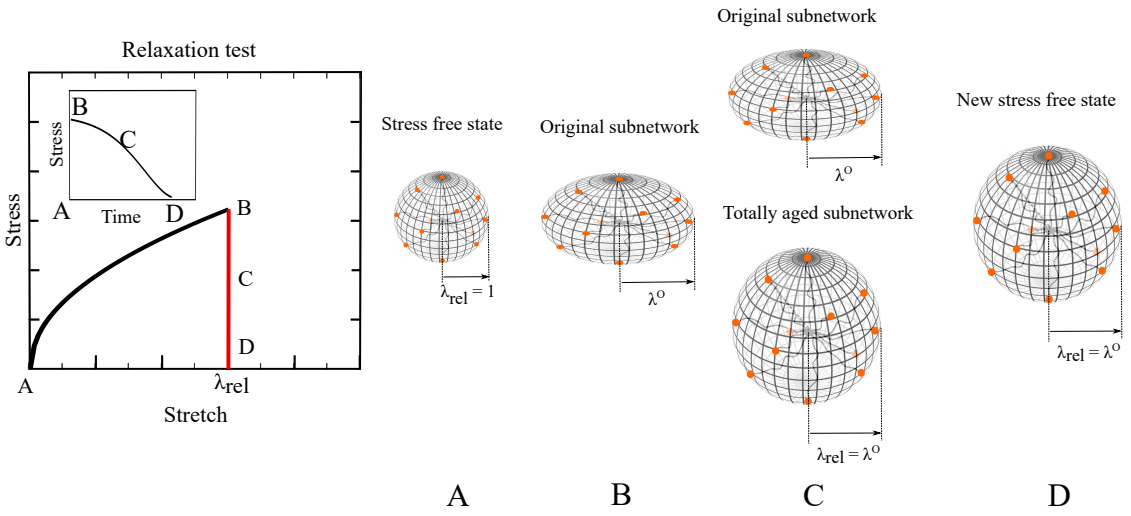

Figure 4.11. Micro-sphere representation of *s* and *b* networks during relaxation test.

at the reference configuration, namely $\lambda_{rel} = 1$ and $\lambda^{\infty} = \lambda^{o}$, the problem will be substantially reduced to loading of a two-network system very similar to hydrogel. Again, going back to micro-sphere concept, the new stress free state would be a micro-sphere just like the virgin material. Thus, if we draw similar figure as Fig. 4.11 for this case, there would be no difference in micro-spheres of aged and unaged material.

4.6.2 Network rearrangement

4.6.2.1 Chain rearrangement within a network

It can be assumed that the total number of active segments remains constant during deformation [100]. To formalize this idea, let's denote the total number of active chains with end-to-end distance $\bar{r}$ per unit referential volume in unaged and totally aged networks by $N_o(\bar{r})$ and $N_\infty(\bar{r})$, respectively. Then, the assumption of conservancy in number of active segments during loading leads to

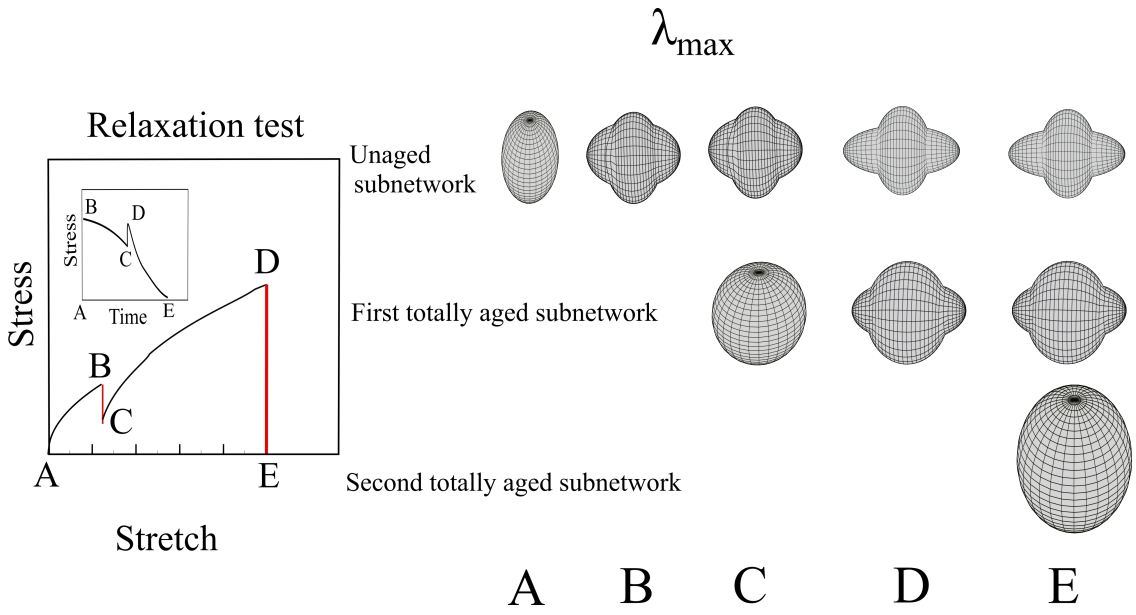

Figure 4.12. Evolution of λ_{max} during relaxation test.

$$\tilde{N}_o\left(\lambda_{mo}^{\boldsymbol{d}}\right) = N_{0o}\Phi_o\left(\lambda_{mo}^{\boldsymbol{d}}\right), \qquad \tilde{N}_\infty\left(\lambda_{m\infty}^{\boldsymbol{d}}\right) = N_{0\infty}\Phi_\infty\left(\lambda_{m\infty}^{\boldsymbol{d}}\right). \quad \text{where} \quad \Phi_o(x) = \left(\int_{D_o(x)} \tilde{P}_o(n)\, n dn\right)^{-1}, \quad \Phi_\infty(x) = \left(\int_{D_\infty(x)} \tilde{P}_\infty(n)\, n dn\right)^{-1} \tag{4.21}$$

Tilde parameters are normalized values. In addition, the variables N_{0o} and $N_{0\infty}$ are material parameters and represent the number of active chains per unit volume in each network at stress free state.

4.6.2.2 Chain transition between unaged and newly-formed aged networks

In addition to conservancy during loading in each network, there should be a conservation law of segments during aging. To be more clear, $N_{0\infty}$ is not an independent parameter and should be calculated based on N_{0o}. To calculate $N_{0\infty}$, we consider the transition of active segments between

unaged and newly-formed aged networks. This yields

$$\int\limits_{D_\infty(1)} N_{0\infty} P_\infty\left(n, \bar{r}_{0\infty}, q_\infty\right) n dn = \int\limits_{D_o(1)} N_{0o} P_o\left(n, \bar{r}_{0o}, q_o\right) n dn \tag{4.22}$$

Since N_{0o} and $N_{0\infty}$ are not functions of n, they can come out of the integral. Moreover, since limits of integral are constant, we would get

$$N_{0\infty} = C_1 N_{0o} \tag{4.23}$$

where

$$C_1 = \frac{\int\limits_{D_o(1)} P_o\left(n, \bar{r}_{0o}, q_o\right) n dn}{\int\limits_{D_\infty(1)} P_\infty\left(n, \bar{r}_{0\infty}, q_\infty\right) n dn} \tag{4.24}$$

4.7 Transition to Macro-model

4.7.1 3D generalization

Each network is considered to have a unique composition to describe a specific energy-dissipating damage mechanism. By combining Eq. (4.1) and Eq. (4.15), the strain energies of the unaged and totally aged networks with respect to their subnetworks can be written as

$$\Psi_{\mathrm{M}} = \rho_o(t)\Psi_o + \rho_\infty(t)\Psi_\infty \quad \rightarrow \quad \sum_{j=1}^{k} \overset{\boldsymbol{d}_j}{\psi_M}\, w_j = \rho_o(t) \sum_{j=1}^{k} \overset{\boldsymbol{d}_j}{\psi_o}\, w_j + \rho_\infty(t) \sum_{j=1}^{k} \overset{\boldsymbol{d}_j}{\psi_\infty}\, w_j$$

$$\rightarrow \quad \psi_{\mathrm{M}} = \rho_o(t)\psi_o + \rho_\infty(t)\psi_\infty \tag{4.25}$$

4.7.2 Final formulation

For an incompressible polymer matrix we have

$$\det \boldsymbol{F} = 1 \tag{4.26}$$

where $\boldsymbol{F}$ denotes the macro-scale deformation gradient. In view of Eq. (4.15) and Eq. (4.25), the first-Piola Kirchhoff stress tensor $\boldsymbol{P}$ can be written as

$$\boldsymbol{P} = \frac{\partial \Psi_M}{\partial \boldsymbol{F}} - p\boldsymbol{F}^{-T}, \quad \boldsymbol{F} = \boldsymbol{F}_o = \boldsymbol{F}_{rel}\boldsymbol{F}_\infty. \tag{4.27}$$

where p stands for an arbitrary scalar parameter which can be defined according to a particular boundary value problem. The contributions of the unaged and totally aged networks $\frac{\partial \Psi_o}{\partial \boldsymbol{F}}$ and $\frac{\partial \Psi_\infty}{\partial \boldsymbol{F}}$ can be derived from the formulation of the network evolution model [100, 23, 101]. Thus, following the method presented in [101] and in view of Eq. (4.12) and Eq. (4.15)

$$\frac{\partial \Psi_M}{\partial \boldsymbol{F}} = \sum_{i=1}^{k} w_i CT \left[N_{0o}\rho_o(t,T) \frac{\partial \overset{\boldsymbol{d}_i}{\psi_o}}{\partial \overset{\boldsymbol{d}_i}{\lambda_o}} \frac{\partial \overset{\boldsymbol{d}_i}{\lambda_o}}{\partial \underset{o}{\overset{\boldsymbol{d}_i}{\chi}}} \frac{\partial \underset{o}{\overset{\boldsymbol{d}_i}{\chi}}}{\partial \boldsymbol{F}_o} + N_{0\infty}(t)\,\rho_\infty(t,T) \frac{\partial \overset{\boldsymbol{d}_i}{\psi_\infty}}{\partial \overset{\boldsymbol{d}_i}{\lambda_\infty}} \frac{\partial \overset{\boldsymbol{d}_i}{\lambda_\infty}}{\partial \underset{\infty}{\overset{\boldsymbol{d}_i}{\chi}}} \frac{\partial \underset{\infty}{\overset{\boldsymbol{d}_i}{\chi}}}{\partial \boldsymbol{F}_\infty} \right], \tag{4.28}$$

where $\overset{\boldsymbol{d}_i}{\lambda}$, $\underset{o}{\overset{\boldsymbol{d}_i}{\chi}}$ and $\underset{\infty}{\overset{\boldsymbol{d}_i}{\chi}}$ denote the micro- and macro-stretches of original and newly-formed aged networks in the direction $\boldsymbol{d}_i$, respectively. Each term of this formulation can be further expanded as

$$\frac{\partial \psi^{\boldsymbol{d}}{}_o}{\partial \lambda_o{}^{\boldsymbol{d}_i}} = \Phi\left(\overset{\boldsymbol{d}_i}{\lambda_m}\right) \int\limits_{D_o(\lambda^{\boldsymbol{d}_i}{}_m)} P_o(n) \left.\frac{\partial \psi_c(n,x)}{\partial x}\right|_{x=\lambda^{\boldsymbol{d}_i}} dn, \tag{4.29}$$

$$\frac{\partial \psi^{\boldsymbol{d}}{}_\infty}{\partial \lambda^{\boldsymbol{d}_i}} = \Phi\left(\overset{\boldsymbol{d}_i}{\lambda_m}\right) \int\limits_{D_\infty(\lambda^{\boldsymbol{d}_i}{}_m)} P_\infty(n) \left.\frac{\partial \psi_c(n,x)}{\partial x}\right|_{x=\lambda^{\boldsymbol{d}_i}} dn, \tag{4.30}$$

where

$$\frac{\partial \psi_c\left(n, x\bar{r}\right)}{\partial x} = \bar{r} K_B T \hat{\beta}\left(\frac{x\bar{r}}{n}, n\right), \tag{4.31}$$

In the Eq. 4.31, $\hat{\beta}$ is the modified version of Langevin elastic force for a short chain.

$$\frac{\partial \lambda^{\boldsymbol{d}_j}}{\partial \chi^{\boldsymbol{d}_j}} = \frac{1}{1 - C^p}, \tag{4.32}$$

$$\frac{\partial \overset{\boldsymbol{d}_i}{\chi}}{\partial \boldsymbol{F}} = \frac{\partial \boldsymbol{d}\bar{\mathbf{C}}\boldsymbol{d}}{\partial \bar{\mathbf{F}}} : \frac{\partial \bar{\mathbf{F}}}{\partial \mathbf{F}} = 2\bar{\mathbf{F}}(\boldsymbol{d} \otimes \boldsymbol{d}) : J^{-\frac{1}{3}}\mathbb{I} = 2J^{-\frac{1}{3}}\bar{\mathbf{F}}(\boldsymbol{d} \otimes \boldsymbol{d}). \tag{4.33}$$

4.8 Parameter Sensitivity Analysis

In this section, a parameter sensitivity analysis is carried out to evaluate the contribution of each parameter to the model. To this end, by fitting the model to experimental data available in literature [1], a reference set for parameter values is created. Then, while all the parameters are kept constant, we change them one by one and trace their effect on predicted behavior. The proposed model has twelve material parameters ; i.e. q_o, q_∞, n_{max}, $\bar{r}_{0o}$, $\bar{r}_\infty$, ν, A_1, E_{a1}, E_{a2}, τ_1, τ_2 and N_{0o}, all of which has clear physical meaning. From mathematical point of view, the parameter N_{0o} just serves as a multiplication factor and thus has not been considered. Table 4.5 shows the reference set of values obtained from fitting to three curves. First, the relaxation test at 80^oC and $\epsilon = 50\%$. Second, intermittent tension test for unaged sample to obtain parameters of original network. Third, intermittent tension test for samples aged at 100^oC for 6 days. This aging status has been considered as an example of totally aged sample. Therefore, the parameters of totally aged network has been obtained from this one.

Using this set of values, we used aging condition of 80^oC and $\epsilon = 50\%$ to analyze the sensitivity of relaxation test to material parameters. Moreover, aged samples at 80^oC for 4 days has been taken

Table 4.5. Reference set of values for material parameters.

$N_{0o}CT$ $[MPa]$	q_o	q_∞	n_{max}	$\bar{r}_{0o}$	$\bar{r}_\infty$	ν	A_1	A_2	E_{a1} $[Jmol^{-1}]$	E_{a2} $[Jmol^{-1}]$	$\tau_1[s^-1]$	$\tau_2[s^-1]$
3.2	0.25	0.35	100	1.45	1.25	1.002	0.8283	0.1717	114150	32417	$9.153 * 10^{10}$	7.962

into account for parameter sensitivity analysis of intermittent test results. It should be obvious that for relaxation test, only parameters of decay function are of interest(since the others effects will cancel out during normalization of stress). Fig. 4.13, Fig. 4.14, Fig. 4.15, and 4.16 show the effect of these parameters in relaxation and intermittent tests.

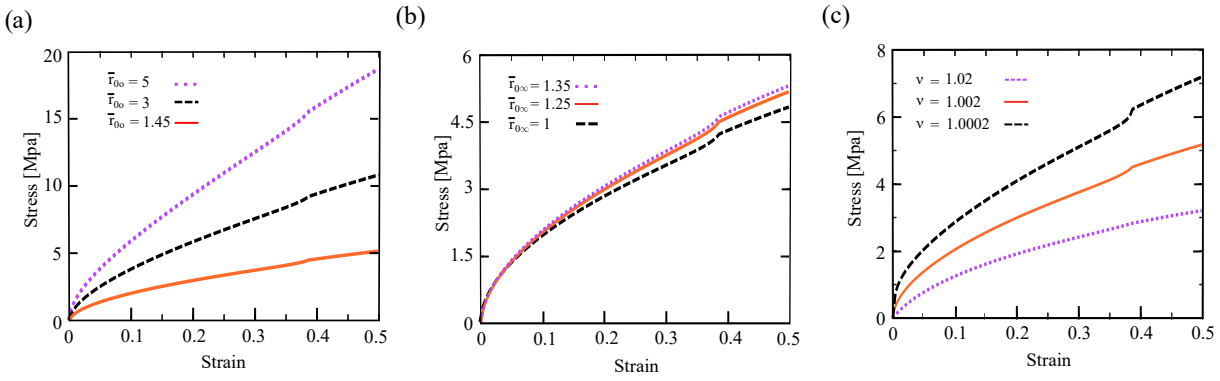

Figure 4.13. Sensitivity analysis of the material parameters included in the model. Solid red lines denote reference set of parameters. Dashed and dot lines depict model predictions due to modified values.

Regarding n_{max} we just choose a big enough value to prevent a cut off from important probability numbers. Thus, it does not affect the model in general and does not need analysing. With increasing $\bar{r}_\bullet$, the average chain length increases. Consequently, lower load is required to induce a certain deformation, as it is shown by Fig.4.13 a. Following the definition we introduced before, $\frac{1}{\nu}$ describes the strength of chain bonds in a specific network. In this regard, higher ν describes weaker chains, which yield faster and thus makes the matrix softer (see Fig.4.13 c).

The proposed decay function is consist of two parts with two different aging rates. The first part controls the higher rate while the second controls the lower one. Thus, the ratio between A_1 and A_2, control the rate of aging. As it can be seen, increasing A_1 causes the rate of aging

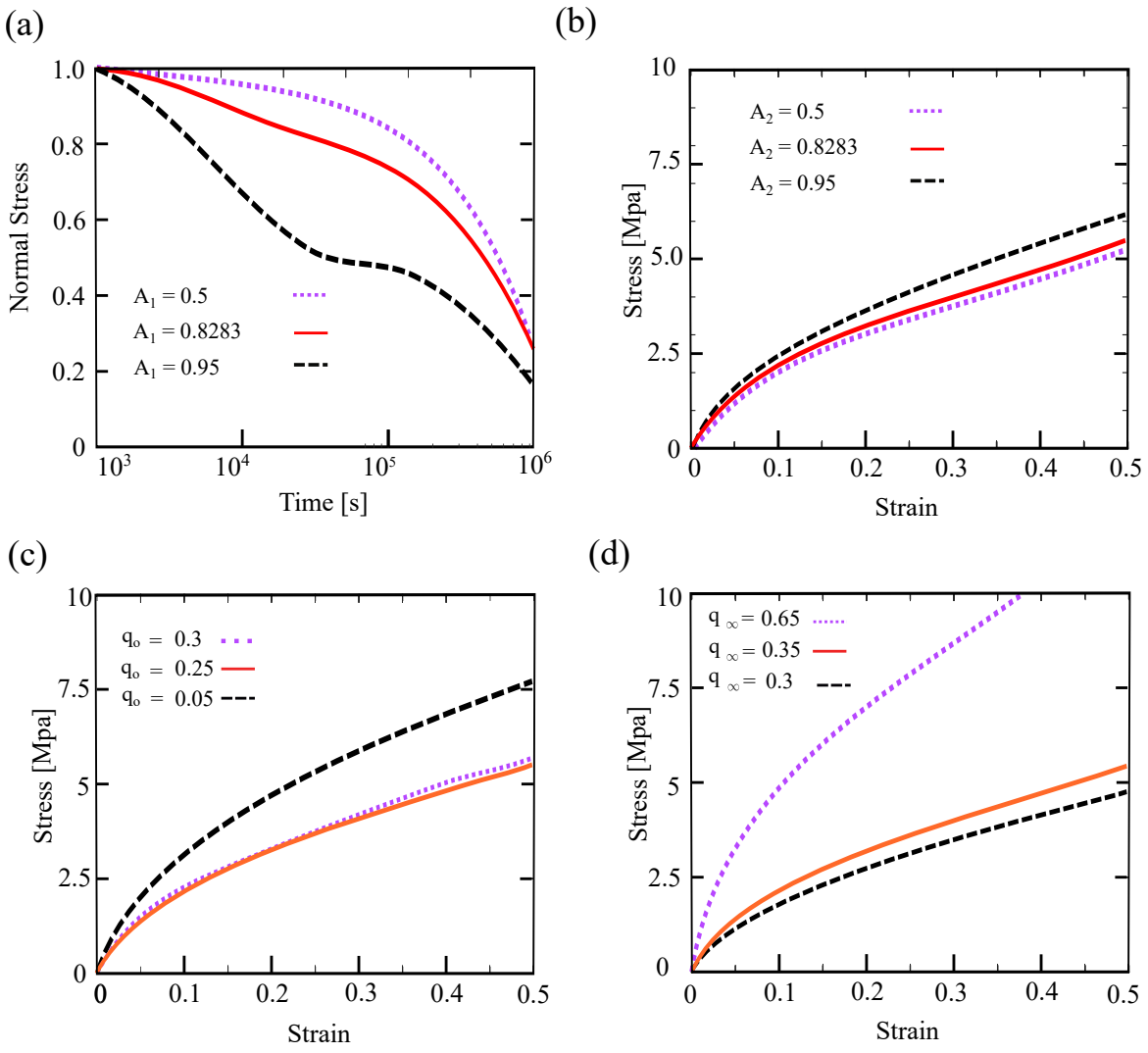

Figure 4.14. Sensitivity analysis of the material parameters included in the model. Solid red lines denote reference set of parameters. Dashed and dot lines depict model predictions due to modified values.

to increase drastically. As a result, we expect to see hardening in intermittent test which is the case here (see Fig. 4.14a and b) . Conversely, increasing A_2 should show the opposite results. Similarly, increasing τ_1 decreases the aging rate at the beginning but has no effect in the long run, while increasing τ_2 do the opposite (Fig. 4.15a and b). Therefore, we expect softening by the former and hardening by the latter. As it can be seen, intermittent test result hardly changed by τ_1 (Fig. 4.15c). The reason for this inconsistency is that the sample at the studying condition are aged samples. Hence, as it has been mentioned is not effected by τ_1 anymore. Finally, it should

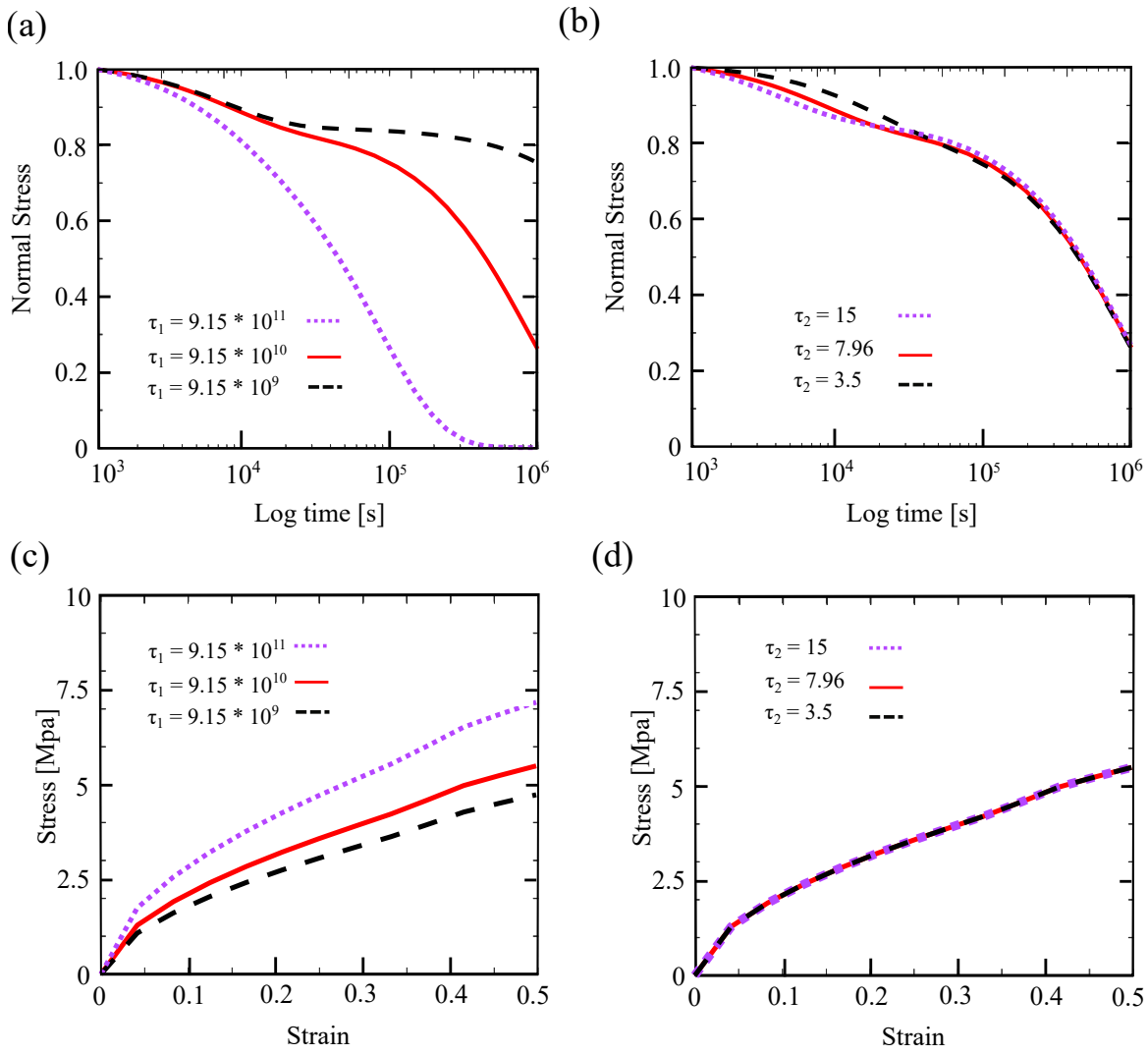

Figure 4.15. Sensitivity analysis of the material parameters included in the model. Solid red lines denote reference set of parameters. Dashed and dot lines depict model predictions due to modified values.

be obvious that by increasing the activation energies for aging reactions, we are causing a delay in aging phenomenon. Thus, the results of Fig. 4.16 should be justified.

Fig. 4.14, part c and d, shows the effect of strain energy parameters on the intermittent test results. First, the effect of q_o and q_∞ is considered. These parameters define the cross-link density of original and aged networks. Thus, their ratio is a measure for the respective rate of cross-linking to chain scission during aging. As $\frac{q_\infty}{q_o}$ increase, this rate will increase and thus we expect hardening and vice versa. Having this in mind, increasing q_o should cause softening while increasing q_∞ will

cause hardening. As it can be seen from Fig. 4.14c and Fig. 4.14d, this is the case here.

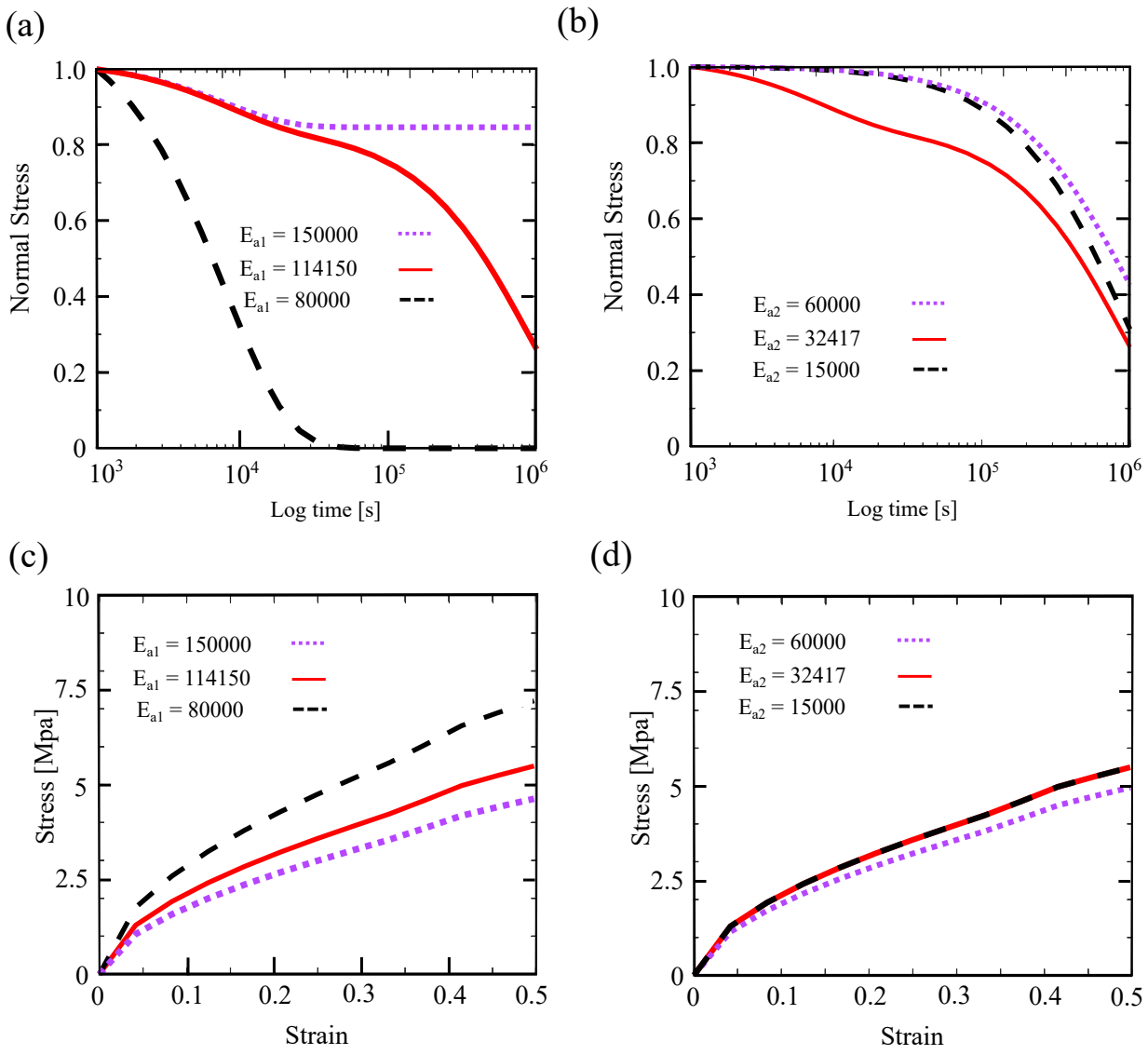

Figure 4.16. Sensitivity analysis of the material parameters included in the model. Solid red lines denote reference set of parameters. Dashed and dot lines depict model predictions due to modified values.

4.9 Validation

The predictions of the proposed model validated against a set of experimental data available in literature [1] to asses its capabilities. The material parameters are derived as discussed in the previous section. Once the material parameters are derived, model predictions are bench-marked against

experimental data with different temperatures, aging times, and strains (see Figure 4.17). With a marginal error, the model is able to predict the loading behavior of samples with different degrees of aging. Table 4.6 shows the average error that occurred in each temperature. The maximum error happens at $\theta = 100^oC$ for samples aged for 24 hours. Since the predictions for $\theta = 60^oC$ and $\theta = 80^oC$ have high accuracy, it can be deduced that the major source of error is the anomalies such as DLO. Thus, one of the approaches to reduce this error in future could be to take the effect of DLO into account.

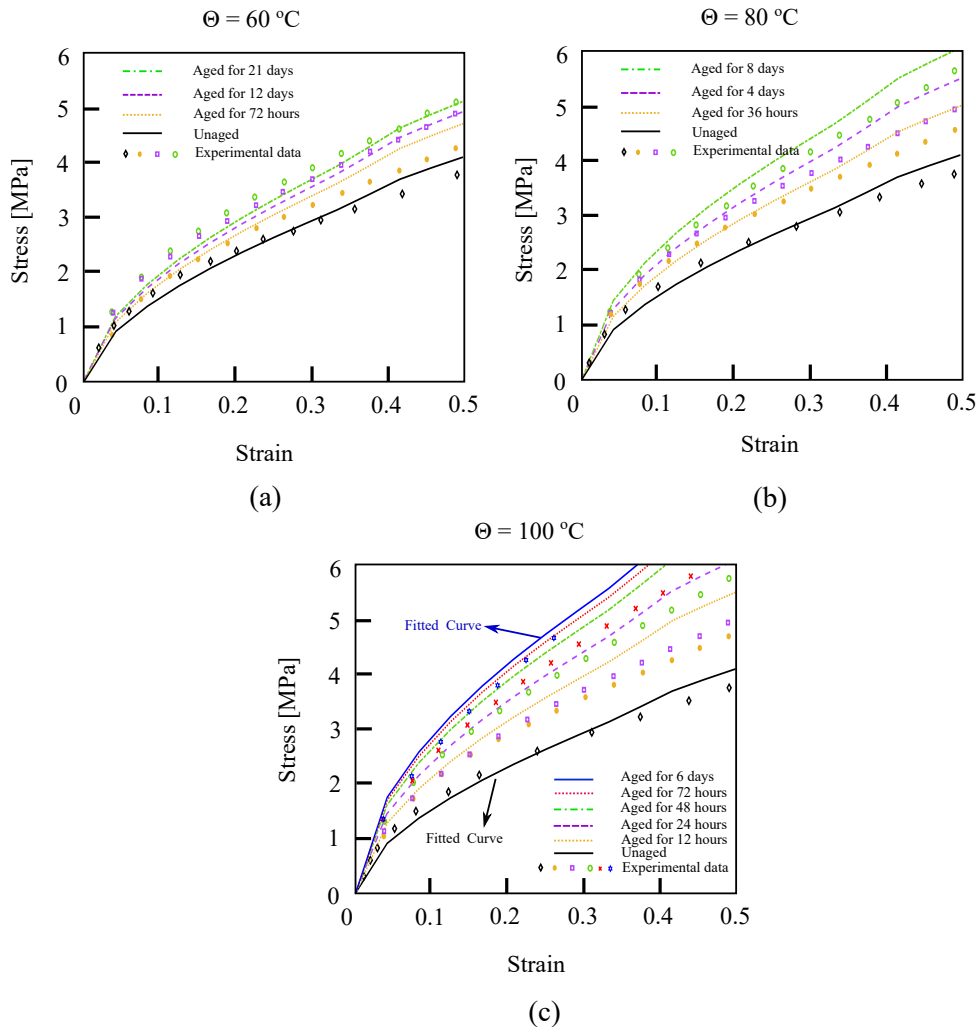

Figure 4.17. Prediction of experimental results (a) intermittent test at $\theta = 60^oC$ and (b) $\theta = 80^oC$ and (c) $\theta = 100^oC$.

In order to further evaluate our model, an experimental investigation has been carried out to

Table 4.6. Prediction error values.

Temperature	$\theta = 60^oC$	$\theta = 80^oC$	$\theta = 100^oC$
Average Error	7%	9%	15%

study the effect of aging on the constitutive behavior of rubber-like materials. To do so, black SBR sheets with 1/8" thickness has been ordered from *Rubbercal* company. Then, using a dumbbell shape punch, the samples has been punched based on the standard sizes specified in ASTM D412 standard. Samples has been aged at four different temperatures namely $45^oC, 60^oC, 80^oC$ and 95^oC and zero humidity. Using a *TESTRESOURCES* tensile test machine, the aged samples has been gone through different set of tensile and cyclic tests. The tensile failure tests has been used to evaluate the proposed model and the result is presented in the Fig. 4.18. As it can be seen from these results, all the model prediction is close to 10% error range.

Once validated, the model is used to describe different damage behaviors of elastomers through aging. First, the changes in the loading-unloading response of the material aged at 60^oC at different aging time has been compared (see Fig.4.19). As it can be seen, the model is able to predict the behavior with a marginal error. Moreover, using the model we predicted the changes in energy loss by varying the time and temperature of storage (see. Fig. 4.20). To quantify energy loss, we considered the area enclosed between first loading and unloading is proportional to energy loss. The model predict the correct trend in which the energy loss increases during aging.

Finally, it is important to check whether the model guarantees a stress-free ageing induced network rearrangement (cross-linking) under constant strain in time or not. To do so, a simple relaxation simulation has been done. As it can be seen in Fig. 4.21, the samples has been stretched to three times of their lengths and then they were let to relax at 95^oC. It is clear that the materials are relaxing till they reach zero-state stress. Then, no matter how long we wait, they remain in this state.

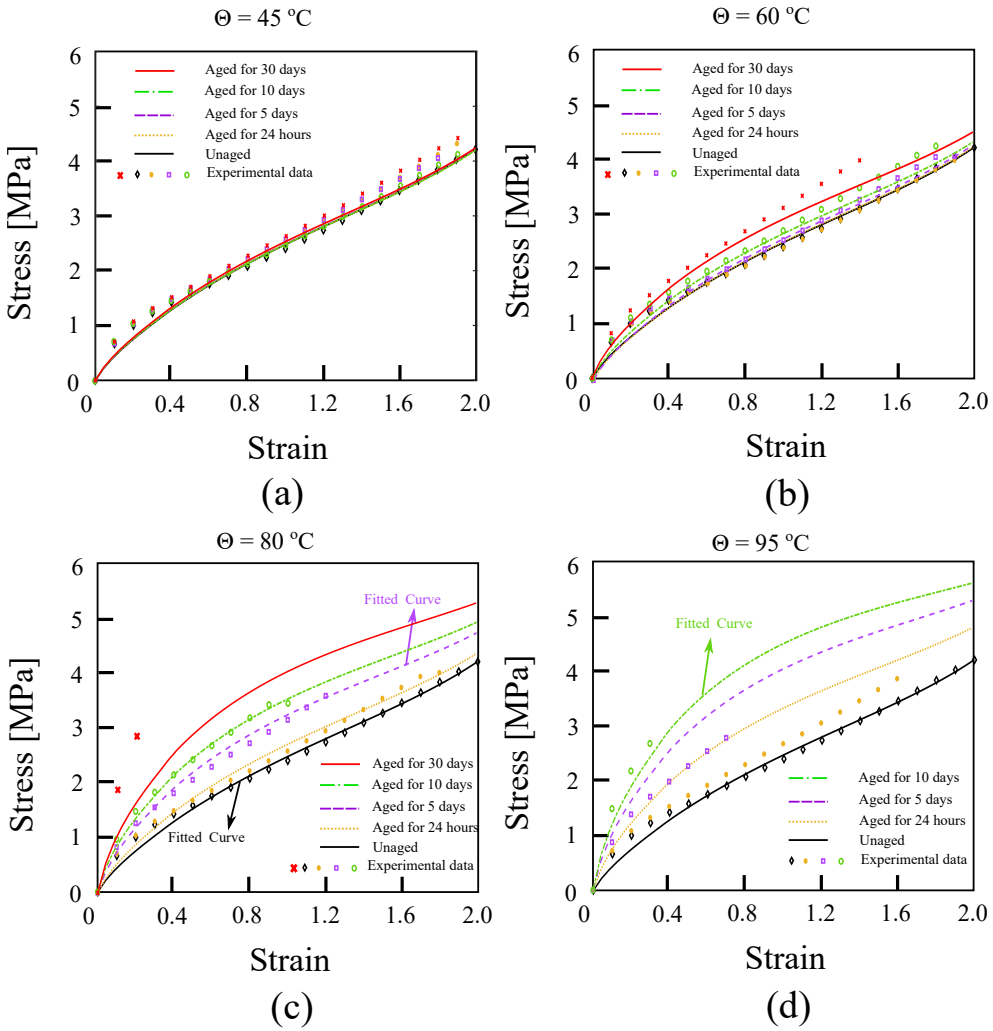

Figure 4.18. Prediction of experimental results (a) intermittent test at $\theta = 45^oC$ and (b) $\theta = 60^oC$ and (c) $\theta = 80^oC$ and (d) $\theta = 95^oC$.

4.10 Conclusion

In this section, we proposed different decay functions and compare their usability for modeling aging phenomenon in rubber-like materials. The proposed decay function is based on chemical reaction kinetics and proved to be a powerful tool in fitting relaxation experimental data. Then, a micro-mechanical model has been presented along with the best decay function. The model is able to predict the changes in the constitutive behavior of rubber-like materials during aging. The model is validated against the recent experimental data of Johlitz et al. as well as our own experimental data and shows good agreement with regard to relaxation and intermittent tests. Furthermore, the

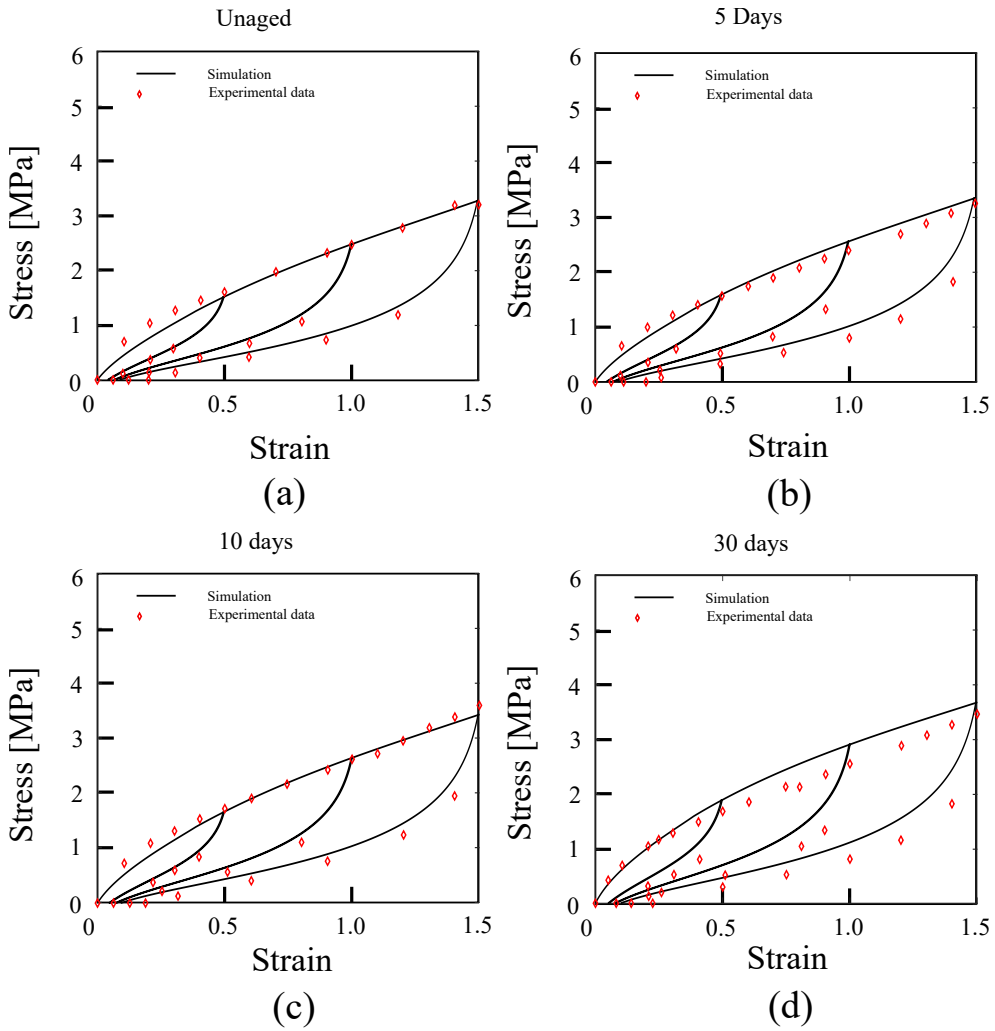

Figure 4.19. Prediction of loading-unloading behavior with respect to time.

proposed model is able to predict loading-unloading behavior with marginal error. Last but not least, the model is able to correctly predict the trend of increasing energy loss during aging. There are still some limitations in the model that should be addressed in the future. The most important one is the model inability to predict the behavior in inhomogeneous conditions.

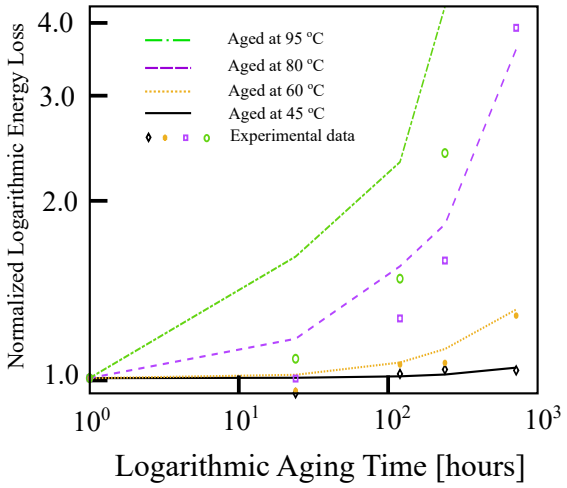

Figure 4.20. Prediction of changes in energy loss with respect to time, and temperature.

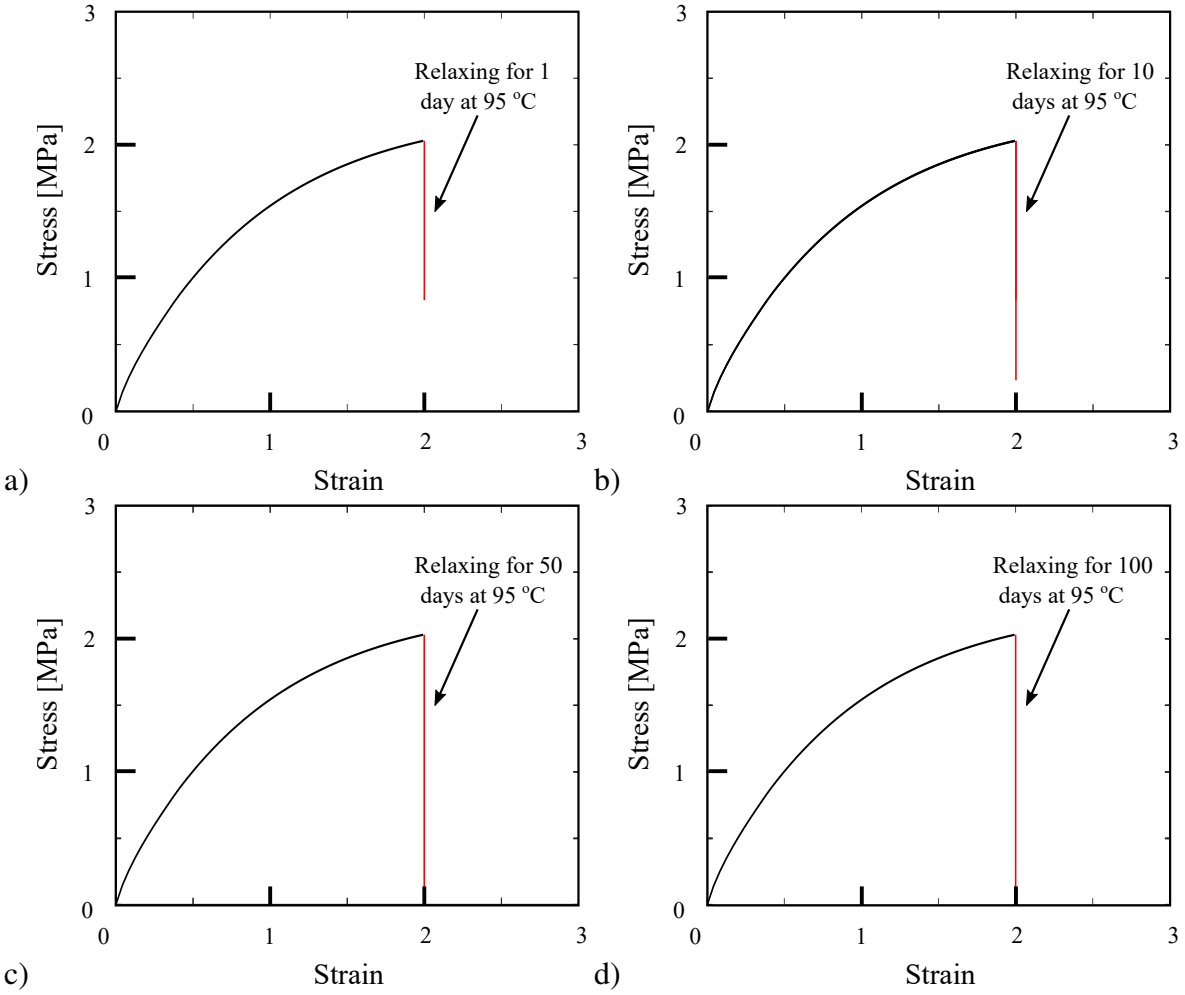

Figure 4.21. Relaxation test simulation at 95^oC for a) 1 day, b) 10 days, c) 50 days, and d) 100 days.

CHAPTER 5

PHOTO-OXIDATIVE AGING

5.1 Introduction

In the previous chapter, we studied the effect of thermo-oxidative aging on the constitutive behavior of cross-linked polymers. In this chapter, our goal is to provide a micro-mechanical model to predict the constitutive behavior of these polymers during photo-oxidative aging. However, the similarities between thermo- and photo-oxidation reactions and morphological changes of polymers [4] compelled us to provide a model that can model the constitutive behavior of polymers in both thermo- and photo-oxidative aging scenarios. The reason behind this decision comes from the fact that the photo-oxidative aging experiments are already happening in alleviated temperatures and thermo-oxidation aging is mixed in the procedure. This complication forced us to abandon the dual-network hypothesis of Tobolsky [21] and use a *continuous network idea*. One of the major assumptions in our model is the assumption of homogeneity. As it is known [4], photo-oxidation is a heterogeneous phenomenon. Thus, the assumption of homogeneity is our major source of error. Hence, providing a diffusion-micro-mechanical model would be a research avenue worth exploring for future studies.

The studies on the photo-oxidative aging phenomenon can be divided into experimental and modeling approaches. Though there are tremendous experimental studies in the area, the modeling studies are much more limited in comparison. Therefore, a need for studies in this direction is apparent.

Experimental studies have been done to relate the chemical changes to mechanical changes of

polymers during photo-oxidation degradation [102]. Moreover, Gupta et al. [103] used FTIR to evaluate the chemical degradation of polypropylene during photo-oxidative aging. They showed that a tremendous decrease would be observed in elongation at break and tensile strength during aging. Similarly, many other authors showed similar results for different polymers [104, 105, 106, 107, 108]. Furthermore, Schoolenberg et al. [109, 110] studied the effects of polymer type and irradiation condition on the morphology of surface cracks. These micro-cracks usually cause the initiation of fracture and the transition from ductile failure to brittle fracture during aging. Many researchers focused on the effect of orientation and external mechanical forces on degradation. Benachour and Rogers [111] showed that oriented polymer materials are less sensitive to photo-degradation. On the other hand, mechanical stretches such as uniaxial or bi-axial stretches enhance the effects of photo-degradation [112, 113, 114, 115]. Similar observations were reported by measurements of molecular weight using gel permeation chromatography and the fact that activation energy decreases with increasing tensile stresses. Most of these studies used carbonyl index as a quantitative measurement to monitor the state of photo-degradation. However, Rouillon et al. [116] showed that the methyl band is a better probe to study the photo-degradation of polypropylene. They further showed that the methyl absorbance could fit an increase in crystallinity, molecular weight, and micro-hardness. Therefore, there should be a comprehensive study of different groups before choosing it as a quantitative measure of aging.

One challenge in aging is to study the effect of neighboring polymers on each other during aging [117]. Kaczmarek [118] showed that photo-oxidation is accelerated in polystyrene and poly(vinyl acetate) blend compared to their pure states. He suggested that this effect is due to mutual interactions of free radicals, which can migrate to the second polymer and re-initiate degradation. Later on, he [119] showed that adding poly(vinyl acetate) to poly(vinyl chloride) has the opposite effect. He attributed this retarding effect to combined reactions between the active species formed in degradation processes. Considering these effects is out of the scope of our model. Therefore, one should consider that the proposed model is for the aging of pure state and might not be able to provide accurate results in combined situations.

To model combined aging, Gillen and Clough [120, 121] expanded the idea of time-temperature superposition and introduced the time-temperature-dose superposition idea. Using this shifting procedure, they have successfully extrapolated predictions that were in excellent agreement with 12 years of low dose rate aging results. Later, they introduced the matched accelerated condition method to calculate the remaining life of polymers in the study [122]. Audouin et al. [123] studied the effect of temperature on the photo-oxidation of polypropylene films. Additionally, they used kinetics of degradation reactions to propose a series of equations for calculating the induction periods of carbonyl and hydroxyl groups. Chinn et al. [124, 125] used the Tobolsky model to predict the permanent set during radiation-induced aging of polymers under high stress. Finally, Ishida et al. [126] assumed *degelation* to be the starting point of significant morphological change and end of service life for that polymer. Then, they calculate this period and consider it as the service life of that polymer.

This chapter will discuss the continuous network hypothesis, which is the necessary concept alongside the previously established ideas to model a combined thermo- photo-oxidative model. Later, a micro-mechanical model is developed and validated about experimental data designed exclusively for photo-oxidation bench-marking.

5.2 Continuous Network Hypothesis

Like thermo-oxidative aging, photo-oxidative aging encourages a series of chemical reactions that can generally be divided into chain scission and cross-linking reactions (see Fig. 4.1). Chain scission reactions break the chains and cause degradation of the original network. On the other hand, cross-linking reactions create a whole new polymer matrix. Therefore, it seems reasonable that by including the effects of these reactions on the micro-mechanical configuration of the polymer matrix, we should be able to model the constitutive behavior.

These reactions only affect cross-link density and end-to-end distance of chains; therefore q and $\bar{r}$. Thus, during aging probability distribution function of the polymer matrix will change over time (Eq. 4.14). The idea here is that if we can model the changes of q and $\bar{r}$ over time, we

should be able to calculate the energy of the polymer matrix at any time. To do so, first, we need to understand the kinetics of chemical reactions during photo-oxidative aging.

5.2.1 Kinetic Model

The kinetics of chemical reactions must be well-understood to describe the rate changes in cross-link density and end-to-end distance over time. The general scheme of photo-oxidation reactions can be written as [123]

$$\begin{aligned} \textit{Initiation:} \quad & POOH \rightarrow \alpha P^{\bullet} \\ \textit{Propagation:} \quad & P^{\bullet} + O_2 \rightarrow PO_2^{\bullet} \\ & PO_2^{\bullet} + PH \rightarrow POOH + P^{\bullet} \\ \textit{Termination:} \quad & PO_2^{\bullet} + PO_2^{\bullet} \rightarrow \text{Product} \end{aligned} \tag{5.1}$$

where P is a symbol for polymeric chemical compounds. Note that here, it is not our intention to describe each concentration of the compounds in 5.1. Here, simply as it has been discussed by Audouin et al. [123], following the classical chain mechanism (Scheme 1), we are simply trying to show the effect of temperature on photo-oxidation reaction's kinetics. Then, use that as a symbol for the idea behind our guess for the statistical model. The rate of chemical oxidation in the course of aging can be defined as 4.3. Moreover, by assuming homogeneous conditions and enough oxygen for the reactions to occur, here, k would be a function of temperature T and the light intensity I. According to the famous Arrhenius function, we will have

$$k = \tau_0 I^{\alpha} e^{-E_a'} \quad \leftarrow \quad E_a' = \frac{E_a}{RT} \tag{5.2}$$

Solving Eq.(4.3) for order 1 reactions and substituting it into Eq.(5.2), one can derive $[P]$

through following equation, often known as *linear Arrhenius relationship*

$$[P] = A_0 exp\left(-\tau_0 I^{\alpha} e^{-E'_a} t\right). \tag{5.3}$$

Where A_0 and τ_0 are functions of temperature to satisfy Eq.(4.3). Using the time-temperature superposition concept, we would have

$$[P] = A_0 exp\left(-\tau_0 I^{\alpha} e^{-E'_a} a_T t\right), \tag{5.4}$$

where A_0 is the weight factor of the decay function. Before that, it should be noted that Eq. (5.3) does not represent the concentration for all the reactions shown in (5.1). It simply is a representation of the classical chain mechanism (scheme 1). Therefore, using a similar analogy, the decay function for photo-oxidative aging can be derived following Eq. (5.4) as

$$\rho_0(t) = exp\left(-\tau_0 \Gamma^{\gamma} e^{-E'_{a_{ref}}} a_T t\right), \tag{5.5}$$

where Γ is a unit-less parameter that reflects the effect of UV. Note that γ is also a function of UV radiation; therefore, in the absence of UV, $\gamma = 0$ or $\Gamma^{\gamma} = 1$. Thus, in the absence of UV, the model automatically predicts thermo-oxidative aging results.

By assuming the rate of cross-link formation and scission correlated to their respective chemical reactions, we can derive the parameters governing the rate of photo-oxidative aging.

In most polymeric systems, homogeneous cross-link formation reduces the average end-to-end chain distance across the matrix while increasing the cross-link density. Bond scission usually induces the reverse effect. Representing the changes in the average end-to-end chain length in un-deformed material $\bar{r}$, one can write the normalized contribution of cross-link formation on end-

to-end distance by $-\bar{r}_c^*$ and that of scission by $+\bar{r}_s^*$ which yields

$$\bar{r}(t) = \bar{r}_{0o} - \bar{r}_c^* \left[1 - exp\left(-\tau_1 \exp\left(\frac{-E_{a_c}}{RT_{ref}}\right)\Gamma^{\alpha}(a_{T_2}t)\right)\right] + \bar{r}_s^* \left[1 - exp\left(-\tau_1 \exp\left(\frac{-E_{a_s}}{RT_{ref}}\right)\Gamma^{\beta}(a_{T_2}t)\right)\right]. \tag{5.6}$$

$$\bar{r}_c^* = \bar{r}_c + \bar{r}_{I1}, \qquad \bar{r}_s^* = \bar{r}_s + \bar{r}_{I2} \qquad \& \qquad \bar{r}_c^* < \bar{r}_s^* + \bar{r}_{o0} \tag{5.7}$$

where we assume $E_{a_c} = E_{a_s} = E_{a2}$ is the activation energy needed for photo-oxidation reactions. Moreover, $\bar{r}_c$ and $\bar{r}_s$ are relative weight factors that describe the contribution of cross-link formation and scission due to thermo-oxidation on $\bar{r}$, respectively. Similarly, $\bar{r}_{I1}$ and $\bar{r}_{I2}$ are the relative weight factors due to UV radiation. In our model, we considered the effect of each relative weight factor of UV to be equal in weight but opposite in sign and thus $\bar{r}_{I1} = -\bar{r}_{I2} = \frac{-\bar{r}_I}{2}$. The reason for this sign convention was our observation from the experimental analysis that the material starts to soften after an initial hardening phase. So, chain scission should be more important in time than cross-linking. Here, α and β define the rate of each reaction due to the UV effect. Using the same concept, one can define the contribution of cross-link formation and scission on cross-link density $Cr(t)$ as

$$Cr(t) = Cr_0 - Cr_c^* \left[1 - exp\left(-\tau_1 \exp\left(\frac{-E_{a_c}}{RT_{ref}}\right)\Gamma^{\alpha}(a_{T_2}t)\right)\right] + Cr_s^* \left[1 - exp\left(-\tau_1 \exp\left(\frac{-E_{a_s}}{RT_{ref}}\right)\Gamma^{\beta}(a_{T_2}t)\right)\right]. \tag{5.8}$$

$$Cr_c^* = Cr_c + Cr_{I1}, \qquad Cr_s^* = Cr_s + Cr_{I2} \tag{5.9}$$

Where $Cr = 1 - q$ is cross-link density. Just like before, Cr_c and Cr_s are the relative weight factors due to thermo-oxidation and $Cr_{I1} = -Cr_{I2} = \frac{-Cr_I}{2}$ are the relative weight factors due to photo-oxidation. Since Cr should always be smaller than one, two constraints should be imposed

on the parameters of the equation 5.8. These constraints are as follows

$$0 < Cr_0 < 1, \quad \text{and} \qquad \frac{Cr_I}{2} < Cr_c \tag{5.10}$$

As it can be seen, there is an obvious distinction between parameters that have an active role in thermo-oxidation with the ones that only come into effect in photo-oxidative aging. Thus, photo-oxidation parameters should be defined in a way that does not affect thermo-oxidation's results. Consequently, $\bar{r}_I$, Cr_I, α, β, and E_{a2} should all be a function of Γ. This means that in the case of thermo-oxidative aging where $\Gamma = 0$, these parameters would be zero.

From here on, every step of the model would be the same as sections 4.5 through 4.7. Therefore, for the sake of brevity, we will not repeat them here.

5.3 Parameter Sensitivity Analysis

A parameter sensitivity analysis has been carried out to evaluate the contribution of each parameter to the model. To this end, a reference set for parameters' values is created by fitting the model to our experimental data. Then, we change each parameter and trace their effects on predicted behavior while all the other parameters are kept constant. The proposed model has fifteen material parameters; i.e. N_{0o}, $\bar{r}_{0o}$, ν, Cr_0, $\bar{r}_c$, $\bar{r}_s$, Cr_c, Cr_s, E_a, $\bar{r}_I$, Cr_I, γ, α, β, and E_{a2}, all of which has clear physical meaning. As it can be seen from equations (5.6) and (5.8), we omitted parameters τ_0 and τ_1. This is because these parameters have only been there in the sense of dimensionality of the formulations and they can be considered as 1 since their effect can be considered in other parameters such as α and β.

In general, model parameters can be categorized into three types: original (virgin) network, thermo-oxidative aging, and photo-oxidative. Thus, in this sense, N_{0o}, $\bar{r}_{0o}$, ν, and Cr_0, are the four parameters that should be defined from deformation in an unaged state. $\bar{r}_c$, $\bar{r}_s$, Cr_c, Cr_s, and E_a are the five parameters to be defined by thermo-oxidative experimental results and the rest can be derived from photo-oxidative aging data.

One of the model's advantages is that its parameters are independent of each other between the three above-mentioned phases, virgin, thermo, and photo. Therefore, the fittings can be done in three stages i) on the unaged material, ii) on the thermo-oxidation only data, and finally, iii) on the combination of photo- and thermo-oxidation data or the photo-oxidation data alone if available. Therefore, we first use a genetic algorithm to fit the model on a set of loading-unloading data on the virgin material. Table 5.1 shows the results for this fitting.

Table 5.1. Reference set of values for material parameters influencing the virgin state.

$N_{0o}CT[MPa]$	Cr_0	$\bar{r}_{0o}$	ν
13.51	0.99	3.39	1.001

After fitting for the virgin material, we set those material parameters to be constant and use our algorithm to fit for the thermo-oxidative aging data at $95°C$ after 30 days. Table 5.2 shows the results for such a procedure.

Table 5.2. Reference set of values for thermo-oxidative material parameters.

Cr_c	Cr_s	$\bar{r}_c$	$\bar{r}_s$	$E_a[Jmol^{-1}]$
0.044	0.0188	0.6296	0.034	39656

Finally, we use the photo-oxidative aging results at spectral irradiance of $1.25W/m^2nm$ at $340nm$ and $80°C$ after 30 days of aging for our final fitting process to obtain the rest of the parameters. Therefore, UV irradiance is $1.25W/m^2$ which means that the unit-less value for $\Gamma = 1.25$. Table 5.2 shows the fitted values for this final stage.

Table 5.3. Reference set of values for photo-oxidative material parameters.

Cr_I	$\bar{r}_I$	γ	α	β	$E_{a2}[Jmol^{-1}]$
-0.0149	-1.148	1	-15	-20	27333

The effect of parameters presented in Table 5.1 and the effect of E_a has already been discussed in the previous chapter. Hence, they are not studied here. For analyzing the rest of the parameters, aged samples at $80°C$ for 30 days at the combined photo- and thermo-oxidative aging environment

has been taken into account. The results of these parameter sensitivity analysis has been represented in Fig 5.1 and Fig 5.2. In these figures solid black line is the reference values, the dashed blue line and red dotted line are for the lower and higher values of the parameter under study, respectively.

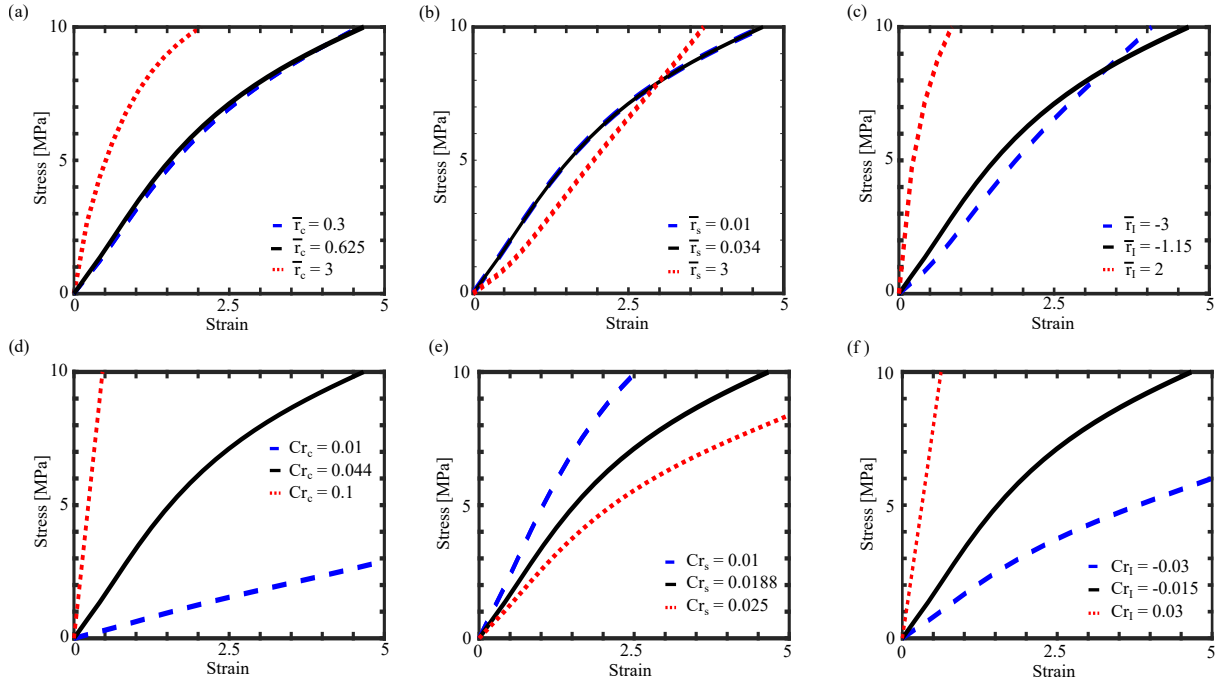

Figure 5.1. Sensitivity analysis of the material parameters included in the model.

Fig. 5.1, a-c, show the parameters that affect the end-to-end distance of the polymer matrix.As it is obvious, increasing $\bar{r}_c$ and $\bar{r}_I$ or decreasing $barr_s$ will reduce the total end-to-end distance which in turn cause hardening. The reason for this behavior is clear, as shorter chains are harder to stretch than longer ones. The same idea can be hold for cross-link density parameter (see Fig. 5.1 d-f).

Parameters that are shown in Fig. 5.2, all affect the amount of UV radiation. Increasing α means increasing the effect of cross-linking over chain scission (see Fig. 5.2 a). The opposite can be said about the effect of β. Increasing γ means to increase the ratio of aged network over unaged ones. Since aged network is harder than unaged one at the selected aging stage, increasing γ cause hardening. Lastly, since the final effect of UV radiation on our material is softening, the

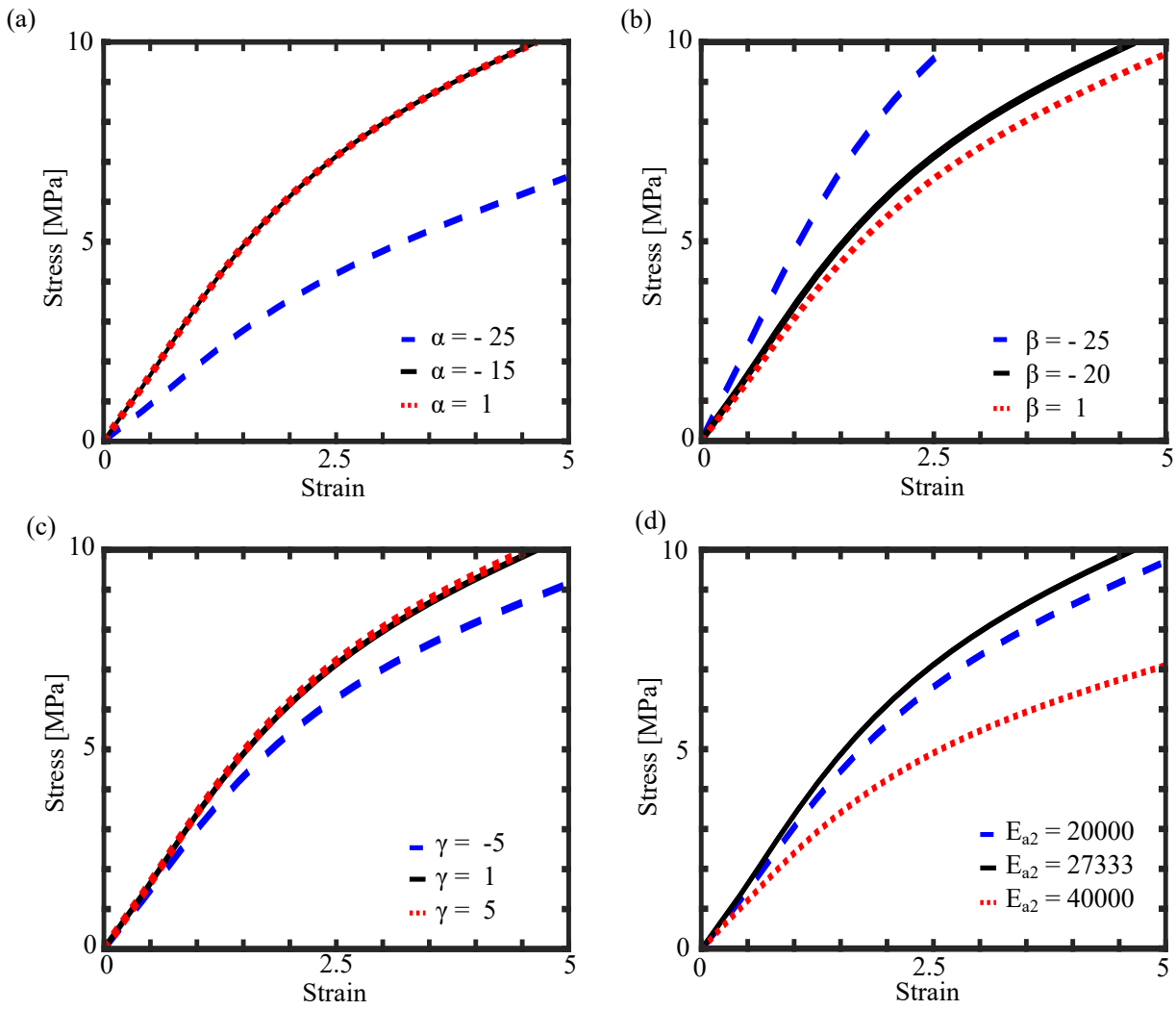

Figure 5.2. Sensitivity analysis of the material parameters included in the model.

parameters that enhance its effect will facilitate softening results, as is the case for increasing E_{a2}.

5.4 Material & Methods

To evaluate our model, an experimental study to investigate the effect of photo- and thermo-oxidation on the constitutive behavior of rubber-like materials has been carried out. We chose a common industrial polyurethane adhesive as an example of rubber-like polymer. Samples were prepared in accordance with ASTM D-412 standard by casting them in custom designed molds by means of injecting the adhesive in mold by a commercial applicator. Then, the samples were cured

in room temperature for 14 days. After that, they were carefully removed from the mold to avoid any damage prior to the tests. Then, samples were categorized and labeled for two different aging tests.

- Thermo-oxidative tests: For thermo-oxidative test, samples has been aged at three different periods (1 day, 10 days, and 30 days) and three different temperatures namely $60^oC, 80^oC$ and 95^oC and zero humidity.

- Photo-oxidative aging: Samples were separately aged in accordance to ASTM G-151 at an spectral irradiance of $1.25W/m^2nm$ at $340nm$ wavelength using a *Q-lab QUV* machine. The aging has been conducted at three different temperatures, $45^oC, 60^oC$ and 80^oC. Three different duration has been chosen for each temperature, namely 10 days, 2 months,and 5 months for 45^oC and the same periods as thermo-oxidative tests for the other two temperature.

Using a *TESTRESOURCES* universal tensile testing machine, the aged samples were characterized by different set of quasi-static tensile and cyclic tests. The tensile failure tests of photo-oxidative aged samples have been used to evaluate the proposed model. By fitting the model to some of the experimental data, a reference set for parameter values has been created. Table 5.1 to Table 5.3 show the reference set of values obtained from fitting to the curves obtained from thermo- and photo-oxidative aged samples. It should be noted here, that although the number of parameters seems high, they are not difficult to fit since they are independent from each other. As it has been shown in previous sections.

5.5 Results

Once the material parameters are derived, model predictions are bench-marked against photo-experimental data with different temperatures, aging times, and strains (see Fig. 5.3). With a marginal error, the model is capable of predicting the constitutive behavior of aged samples. Table 5.4 shows the average errors that occurred in each temperature. Since the photo-oxidation phe-

nomenon starts from the surface, it is highly dependent on diffusion factors which has not been considered in our model. This would be the major source of our errors.

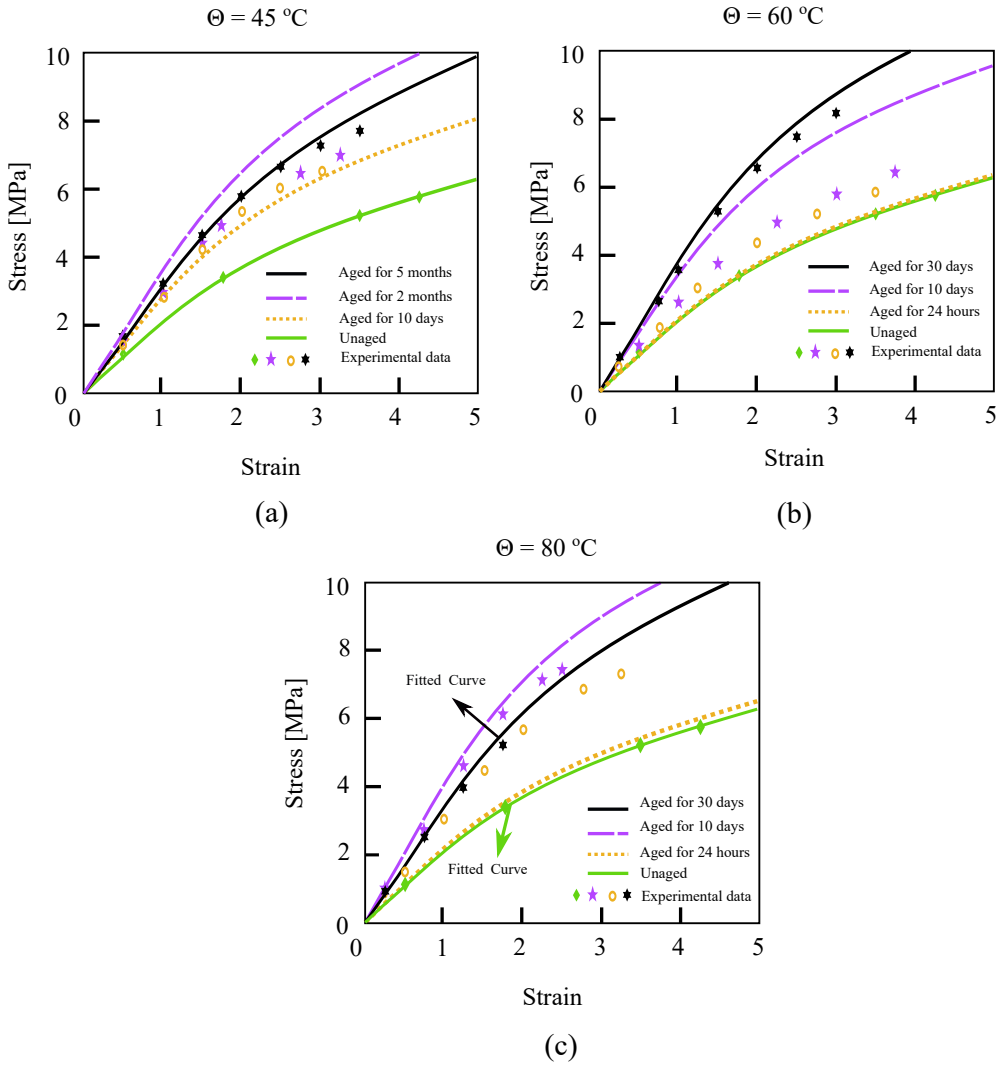

Figure 5.3. Prediction of photo-oxidation experimental results (a) intermittent test at $\theta = 45^oC$, (b) $\theta = 60^oC$, and (c) $\theta = 80^oC$.

Table 5.4. Prediction error values for photo-oxidative aging.

Temperature	$\theta = 45^oC$	$\theta = 60^oC$	$\theta = 80^oC$
Average Error	5.43%	9.68%	8.22%

To further assess our model capabilities, we checked its prediction for the case when UV irradiance is $0W/m^2$ which means that the unit-less value for $\Gamma = 0$. This should produce the prediction

for thermo-oxidative aging only. The predictions are presented in Fig. 5.4. As it can be seen, the model is able to predict the behavior with marginal error. Table 5.5 shows the average errors that occurred in each temperature.

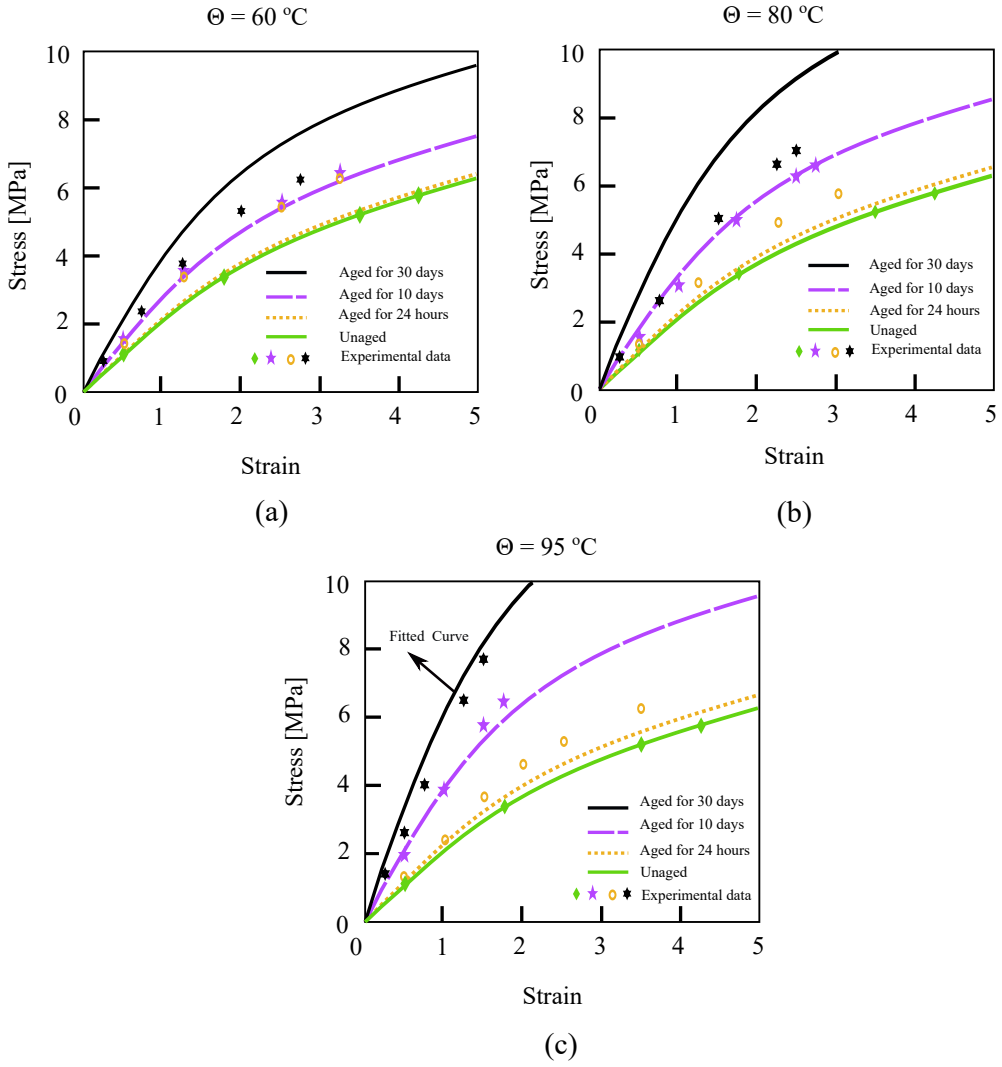

Figure 5.4. Prediction of thermo-oxidative aging experimental results (a) intermittent test at $\theta = 60^oC$, (b) $\theta = 80^oC$, and (c) $\theta = 95^oC$.

Table 5.5. Prediction error values for thermo-oxidation.

Temperature	$\theta = 60^oC$	$\theta = 80^oC$	$\theta = 95^oC$
Average Error	8.43%	11.17%	7.18%

Once validated, the model is used to describe different damage behaviors of elastomers through

aging. First, the changes in the loading-unloading response of the material aged at different aging temperatures and different aging time in photo-oxidation tests has been compared (see Fig.5.5). As it can be seen, the model is able to predict the behavior with a marginal error.

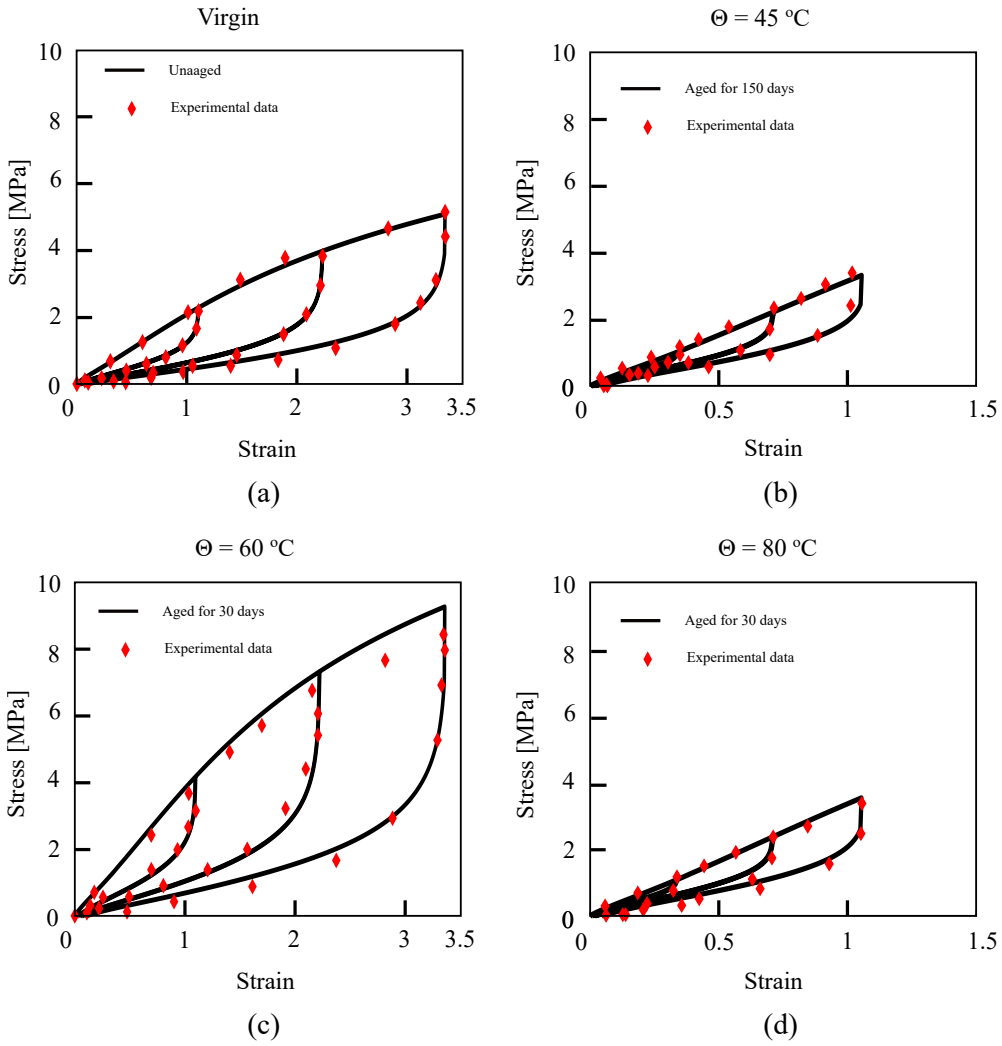

Figure 5.5. Prediction of loading-unloading behavior with respect to time.

Lastly, it should be noted that the model is capable to be used for any type of loading, one should just change the deformation gradient based on the loading in mind. The reason that we only focused on tension is the ease of experiments.

5.6 Conclusion

We proposed a micro-mechanical model to predict the changes in the constitutive behavior of elastomers during both photo-oxidative and thermo-oxidative aging. The proposed model is based on the concept of continuous network hypothesis and has seventeen material parameters. The model is validated against our own experimental data and shows good agreement with regard to both thermo-oxidative aging and photo-oxidative aging tests. The proposed model offers great opportunity for finite element simulation of elastomers. There are still some limitations in the model that should be addressed in the future. The most important one is to reduce the number of fitting parameters by using simpler distribution functions. Furthermore, diffusion and viscoelastic behavior should be added to the model which the modular platform nature of the proposed model allows the addition of such effects in future.

CHAPTER 6

Accumulated Damage

Ultraviolet light exposure does not always make an initial impact, with the exception of a sunburn. For automotive industry, one might not see the same effects as a burn but following prolonged periods of UV exposure and high temperatures, the interior and exterior can gradually experience damage. Areas exposed to direct sunlight can see interior temperatures from 60^oC to 95^oC. With time, cracks and fading along the dashboard, upholstery, paint and other less-visible components will be spotted. Extreme heat and regular UV exposure have potential to affect car's performance and passengers' safety on the road as well. Since belts and hoses can fray and crack and eventually detach due to degradation. Thus, understanding thermal and photo-oxidative degradation is of utmost importance in automotive industry. Till now, we have modeled thermo-oxidative aging, photo-oxidative aging and their combinations. What remain is understanding the history of their effects on each other. In this section, we model the accumulated damage from aging at one condition and then immediately going to a second one. This model will be a complimentary model to our previous models to provide a comprehensive case. Furthermore, another form of accumulated damage will be in the shape of cyclic damage. Thus, later on, we will define a method to model cyclic aging conditions as well.

6.1 Design of Experiments

To study the effect of aging in one condition on the other dual aging experiments in the form of $X + Y$ on polyurethane samples has been performed. The aging experiment was planned

considering following environment regimes:

- photo- to thermo-oxidation
- thermo- to photo-oxidation

The schematic diagrams representing dual-aging experiment profiles are reflected in Fig. 6.1. As it can be seen, in dual-environment aging, the temperature remained constant while other environment factors (UV) were swapped.

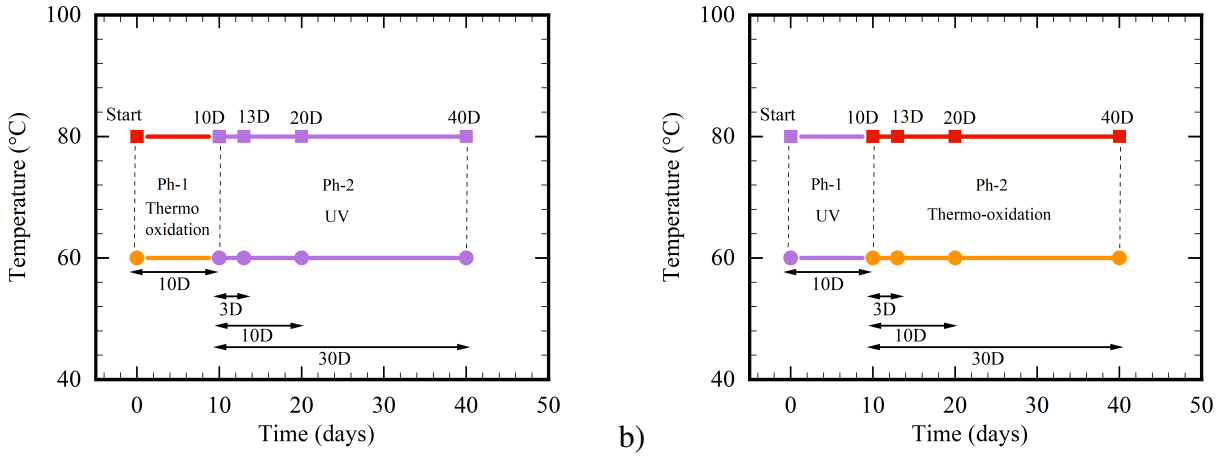

Figure 6.1. Schematic showing profile of dual effect aging conditions (a) UV dual-environment aging (thermo to photo) , and (b) Thermo-oxidative dual-environment aging (photo to thermo).

Dual effect aging experiment is designed in 60^{o}C and 80^{o}C. Samples were aged in same temperature for the complete aging duration. During this study, the specimens of understudy adhesives were subjected to a two-phase aging. The regime name is dictated by the phase-2 environment due to more aging time in second phase (see Fig. 6.1a, and Fig. 6.1b). For instance, in *photo-oxidative dual-aging* (see Fig. 6.1a), samples were kept in thermo-oxidation (phase-1) conditions for 10 days and then were shifted to phase-2 in photo-oxidation (UV) aging for 3, 10, and 30 days. Whereas, for *Thermo-oxidative dual-aging*, in phase-1, specimens were aged in photo-oxidation (UV) condition and after 10 days all batches were shifted to phase-2 which was thermo-oxidation (0%RH) aging condition for 3, 10, and 30 days (see Fig. 6.1b).

Table 6.1. Summary of methods used to maintain desired environmental conditions.

Environmental condition	Temperature	Method
	Thermo-oxidation	
0%RH	60°C, 80°C	Molecular sieves
	Photo-oxidation	
UV light	60°C, 80°C	UVA-340 fluorescent lamps

6.1.1 Dual aging Thermo + Photo

During photo-oxidative dual-effect aging in 60^{o}C, polyurethane based adhesive demonstrated dominant cross-link development at the end of aging period. Phase-1 aging in thermo-oxidative conditions in 60^{o}C shows initial softening attributed to initial cross-links reduction (see Fig. 6.2a). In phase-2 when the material was subjected to UV light, we observed a hardening trend which increased with increase in aging time. At the same time the material toughness reduced.

The polyurethane adhesive in 80^{o}C shows similar initial cross-link reduction during phase-1 aging (0%RH). Its only more severe than what we observed in 60^{o}C, which was expected in severe environment. 80^{o}C aged specimens indicated higher degradation in the form of chain-scission causing substantial decrease in failure stress and failure strain values. Material toughness also decreased considerably (see Fig. 6.3a,b). Tensile tests for all conditions show that with increase in time t, ϵ_f decreased.

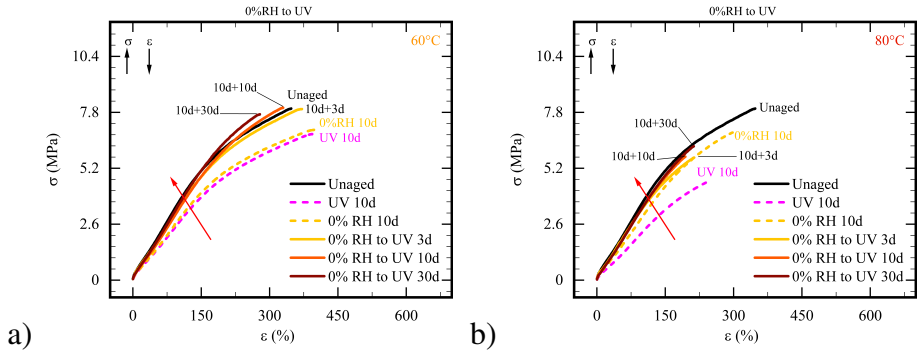

Figure 6.2. Polyurethane behavior during tensile tests after photo-oxidative dual-effect aging (thermo to photo) in (a) 60^{o}C, and (b) 80^{o}C

6.1.2 Dual aging Photo + Thermo

During thermo-oxidative dual-effect aging, polyurethane based adhesive continued to demonstrate dominant cross-link development at the end of aging period. In fact the constitutive behavior appeared to be exactly the same as that of photo-oxidative dual environment aging. But we do observe slightly opposite trends in toughness (see Fig. 6.3a,b). In lower temperature i.e., 60^{o}C, the cross-link formation appears dominant when materials were shifted from UV to thermo-oxidation environment. However, in 80^{o}C, during phase-2, the damage continues its impetus since chain scission due to higher temperature remained dominant over cross-link formation.

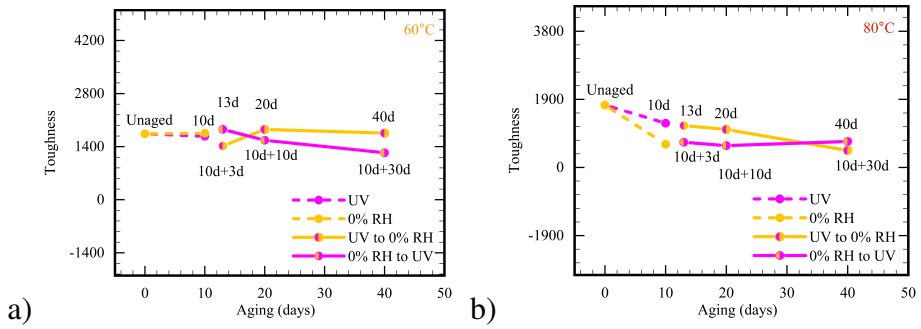

Figure 6.3. Polyurethane toughness compared for each aging regime during dual-effect aging in (a) 60^{o}C, and (b) 80^{o}C

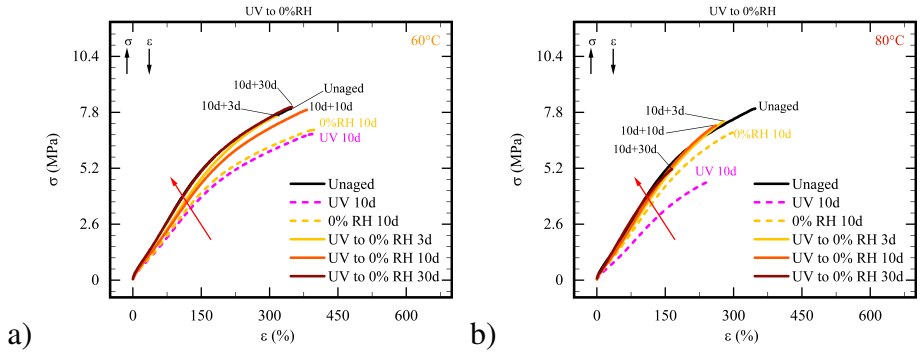

Figure 6.4. Polyurethane behavior during tensile tests after thermo-oxidative dual-effect aging (photo to thermo) in (a) 60^{o}C, and (b) 80^{o}C

6.2 Concept

Now that we have a model that can capture both thermo- and photo-oxidative aging behavior, we are looking to go a bit further and provide a model that can also capture the accumulative damage during aging. The first step in providing such a model was designing a suitable experiment for it. As already discussed in the experimental section, we aged the samples in one environmental condition (e.g., thermo-oxidation) to capture the accumulative damage. We immediately changed that condition to another type (e.g., photo-oxidation). By studying this experimental analysis, we decided to expand our previous model on continuous dual network aging and add the effects of synergism to it. At first glance, this may complicate the model by adding too much fitting parameters; but we were able to simplify the model further to prevent any complications.

Here, the idea is to use the first aging condition as the original (unaged) condition for the second aging condition and let the material age for the second process. Therefore, the process would be as follow. The unaged parameters would be used for the first aging condition X, then the output of this aging process would be the input for the second aging process Y. Using the same hypothesis as our previous aging models, we could model the dual $X + Y$ aging condition.

The proposed model has the same concept of continuous dual network hypothesis as our previous photo-oxidative model. Therefore, for the sake of brevity, we just focus on the parts that is different than the mentioned model.

Consider a model based on the same principle of continuous dual network with the same distribution that has already been discussed (Eq.(4.14). New experimental studies showed that end-to-end chain distance does not change extensively during aging and thus can be considered constant. Therefore, in the new model instead of having an equation like Eq. (5.6), we have:

$$\bar{r}(t) = \bar{r}_{0o} \tag{6.1}$$

But, again the similar equation as before is needed to represent crosslink density. This time, we consider another term for the synergistic effects of the thermo-oxidation and photo-oxidation

as well. In general, the formulation for calculating crosslink density seems too complex with too many parameters. But, it should be noted, in most cases not all of these parameters are needed. These parameters are just shown to represent what is needed for the most general case. Moreover, in the most general case, possible, the power of these formulation is their ease of fitting. As we are going to show for a general case in this section, we can break the fitting to a most basic experiments and formulation, then use those for predictions. Eq. (6.2) shows the new formulation needed to calculate crosslink density ($Cr(t)$):

$$Cr(t) = Cr_0 - Cr_c^* \left[1 - exp\left(-\tau_1 \exp\left(\frac{-E_{a_c}}{RT_{ref}}\right)\Gamma^{\alpha}(a_{TG}t)\right)\right] + Cr_s^* \left[1 - exp\left(-\tau_1 \exp\left(\frac{-E_{a_s}}{RT_{ref}}\right)\Gamma^{\beta}(a_{TG}t)\right)\right]. \tag{6.2}$$

$$Cr_c^* = Cr_c + Cr_{I1} + Cr_{Sy}, \qquad Cr_s^* = Cr_s + Cr_{I2} + Cr_{Sy} \tag{6.3}$$

where many parameters are the same as what has already discussed before. The two new parameters that needs discussion are Cr_{Sy} and a_{TG}. Cr_{Sy} is just a parameter to represent the synergistic effects between photo- and thermo-oxidation. If there is no synergy, this parameter is simply zero. a_{TG} is a modified version of shift factor and is given by:

$$a_{TG} = exp\left(-\frac{E_a}{RT}\left(\frac{T}{T_{ref}} - 1\right)\right)\Gamma^{\gamma^*}. \tag{6.4}$$

6.3 Mechanical Model

For the mechanical model of this section, we used the 8-chain model of Arruda-Boyce [127] along with the alteration theory of Diani et al. [128]. Based on these models, the first statistical mechanics approach to describing the force on a deforming polymeric network assumed Gaussian statistics to apply, that is the chains never approached their fully extended length $r_L = ln$ where n is the number of statistical links of length l in the chain between chemical crosslinks. Moreover,

Chain stretch is always given by the current chain length divided by the initial chain length.

$$\lambda_{\text{chain}} = \frac{r_{\text{chain}}}{r_0}. \tag{6.5}$$

The initial chain length has been obtained from random walk statistics as $r_0 = \sqrt{n}l$. Hence, for the locking chain length or the fully extended one, $r_L = ln$, the locking stretch becomes

$$\hat{\lambda}_{\text{L}} = \frac{r_{\text{L}}}{r_0} = \sqrt{n} \tag{6.6}$$

6.3.1 Langevin chain statistics

In statistical mechanics approach to rubber elasticity models, the polymer chain between two chemical crosslinks is modeled as a number n of rigid links of equal length l. This rigid link can represent one or several repeat molecular units on the actual material and it is the length of the actual chain which undergoes rigid body motion under strain. The initial chain length is denoted by r_0 and as defined before

$$r_0 = \sqrt{n}l \tag{6.7}$$

It is possible to find the most probable angular distribution of rigid links about the chain vector length at any value of the chain length. This probability is equal to the probability of the chain vector length following the use of Langevin statistics by Kuhn and Grün [129]. The chain vector length is denoted by r_{chain}. Following this method, Kuhn and Grün obtained an expression for the probability density function for chain lengths and subsequently the configurational entropy of a

stretched chain of current length r_{chain},

$$s_{\text{chain}} = k\left[c - N\left(\frac{r_{\text{chain}}}{nl}\beta + \ln\frac{\beta}{\sinh\beta}\right)\right] \tag{6.8}$$

where c is a constant, k is Boltzmann's constant and β is the inverse Langevin function. The entropy change on stretching the chains from the unstretched state is proportional to the work of deformation and may be written in terms of the chain length as

$$W = Nk\Theta n\left(\frac{r_{\text{chain}}}{nl}\beta + \ln\frac{\beta}{\sinh\beta}\right) - \Theta c' \tag{6.9}$$

where N is the chain density, c' is a combination of constants and the remaining terms are as defined previously. The incompressibility condition causes that the principle stresses can be determined from the work of deformation to within an arbitrary pressure, p

$$\sigma_i = \lambda_i\frac{\mathrm{d}W}{\mathrm{d}\lambda_i} + p \tag{6.10}$$

where the ,λ_i, are the principle stretches and the pressure may be determined from the boundary conditions. In order to eliminate the pressure term, the stress-stretch relations are frequently written in terms of the difference in two principle stresses

$$\sigma_1 - \sigma_2 = \lambda_1\frac{\mathrm{d}W}{\mathrm{d}\lambda_1} - \lambda_2\frac{\mathrm{d}W}{\mathrm{d}\lambda_2}. \tag{6.11}$$

Following stress-stretch relation for the 8-chain model we have

$$\sigma_1 - \sigma_2 = \frac{Nk\Theta}{3}nL^{-1}\left[\frac{\lambda_{\text{chain}}}{\sqrt{n}}\right]\frac{(\lambda_1^2 - \lambda_2^2)}{\lambda_{\text{chain}}}. \tag{6.12}$$

The stresses $\sigma_1 - \sigma_2$ defined by (6.12) is now combined with the damage theory of Marckmann et al. [130]. For an virgin, isotropic material, we may assume that $N = N_0$ and $n = n_0$. The parameter N changes depending on the maximum stretch applied in. Parameters N and n are

affected by the network alteration like in the Marckmann theory [130]:

$$N\left(\lambda_{\max}\right) \text{ and } \quad n\left(\lambda_{\max}\right) \cdot N\left(\lambda_{\max}\right) = N_0 n_0. \tag{6.13}$$

where $\lambda_{\max}(t) = \mathrm{Max}_{\tau\in[0,t]}\left[\lambda_{\max}(\tau)\right]$. It should be noted that we assume equivalent stretch in all directions. Current experiments supports the assumption of Diani on no physical observations on the evolution of the average length of the chains. Based on that observation, Diani introduced an arbitrary law for the changes of parameters N :

$$N(\lambda) = \left(\zeta(\lambda-1)^2+1\right) N_0 \tag{6.14}$$

The parameter ζ is the only damage parameter. For $\lambda = 1$ which corresponds to the initial state without damage. Relation (6.14) has been chosen to fit correctly the experimental data Diani had but there are no obvious reasons for this relation to work for all elastomers; it is more likely to depend on the nature and the distributions of the fillers, the nature of the gum and other factors.

6.4 Thermo-oxidation

We can use the presented model to consider thermo-oxidative aging cases only. In these cases, the model will simplify considerably as all the terms that are related to photo-oxidation are irrelevant. Therefore, the model will change to:

$$\begin{aligned} Cr(t)^{Th} = Cr_0 - Cr_c\left[1 - exp\left(-\tau_1 \exp\left(\frac{-E_{a_c}}{RT_{ref}}\right)(a_T t)\right)\right] + \\ Cr_s\left[1 - exp\left(-\tau_1 \exp\left(\frac{-E_{a_s}}{RT_{ref}}\right)(a_T t)\right)\right]. \end{aligned} \tag{6.15}$$

where a_T is a shift factor and is given by:

$$a_T = exp\left(-\frac{E_a}{RT}\left(\frac{T}{T_{ref}} - 1\right)\right). \tag{6.16}$$

Now, exactly like before to validate the proposed model, we have performed a series of experimental tests. Three of these experiments are used for fitting purposes and the rest are predictions. The fittings are "Unaged", "Aged for 30 days at 95^oC", and "Aged for 10 days at 80^oC". Figure 6.5 shows the result. As it can be seen, the predictions are all within the acceptable range.

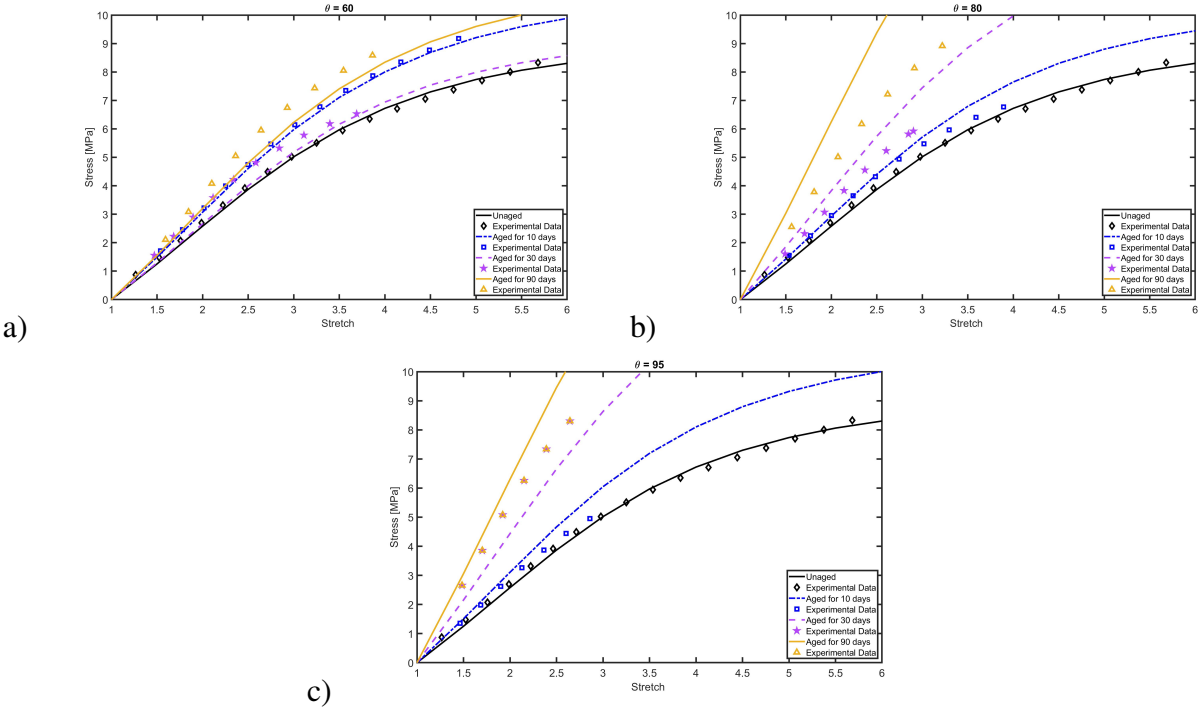

Figure 6.5. Prediction of thermo-oxidative aging experimental results (a) intermittent test at $\theta = 60^oC$, (b) $\theta = 80^oC$, and (c) $\theta = 95^oC$.

6.5 Photo-oxidation

Now, that we have the parameters for the thermo-oxidation, we can fit for a set of experimental data on combined thermo- and photo-oxidation aging. Figure 6.6 shows the results.

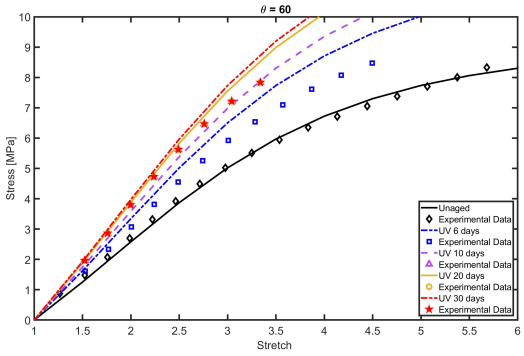

Figure 6.6. Prediction of photo-oxidative aging experimental results at $\theta = 60^oC$.

6.6 Synergistic Effect

Now, the way that the accumulation works, is that it works in a loop. It means that after each aging period, this aging period act as the new unaged condition for the next stage of aging. Let's explain further with an example. Let us assume we want to model an aging condition such as this: Aged in photo-oxidation for 6 days, then aged in thermo-oxidation for 16 days. The way that the model works is as follow, first it used the (6.2) to calculate the new Cr after 6 days of photo-oxidative aging; then, this new Cr act as Cr_0 for a 16 days thermo-oxidation.

The idea is, the model without any further fittings and based on the previous fittings should be able to predict all of these data. Therefore, we will use the parameters that we have obtained from previous sections and without any further fitting predict the experiments. As it can be seen from Fig. 6.7 and Fig. 6.8, the results are pretty good.

a)

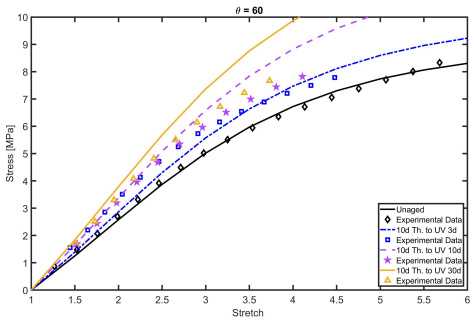

b)

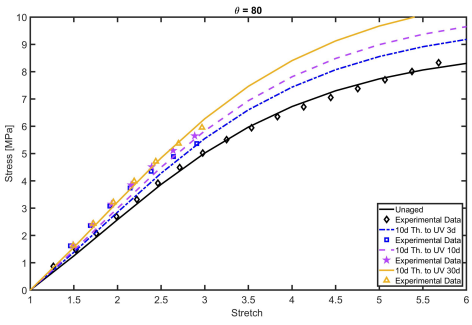

Figure 6.7. Prediction of dual aging experimental results (a) at $\theta = 60^oC$, and (b) $\theta = 80^oC$.

a)

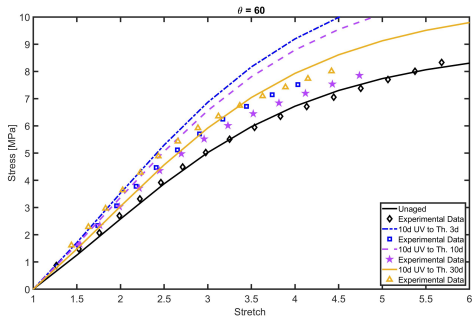

b)

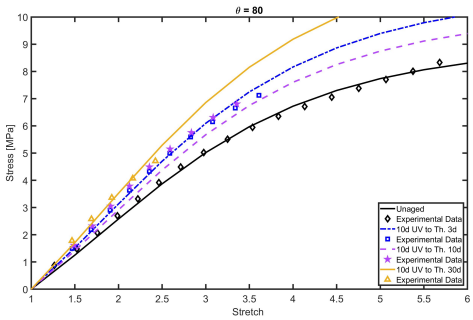

Figure 6.8. Prediction of dual aging experimental results (a) at $\theta = 60^oC$, and (b) $\theta = 80^oC$.

6.7 Thermal Cyclic

Thermal Cycle Test involves cycling automotive parts from high temperature to low temperatures to test their durability. Vehicles in real life may have to encounter varied temperatures and they are required to function to the best of their abilities across temperature. Furthermore, due to elevated operating temperatures of various automotive powertrain systems, environmental thermal testing is crucial at both the cold and hot extremes, as well as transition between those extremes for guaranteeing product quality and reliability. Thus, providing a model for thermal cyclic between these temperatures seems necessary.

The last model needed for capturing accumulated damage during aging would be a model for cyclic aging behavior. For cyclic behavior, one cannot simply accumulate subnetworks and add their contributions like the previous section. The reason for that is during each cycle, each network will create two subnetworks of its own and by this logic the number of subnetworks will grow exponentially. Therefore, calculating each network energy separately would be an impossible task. Thus, we started to look into experimental data collected in our group and experimental data available in literature to create a assumptions and a concept for modeling thermal cyclic aging.

Fig. 6.9 shows the experimental data collected during thermal cyclic experiments. Moreover, Fig. 6.10 shows the experimental thermo-oxidative aging data at single temperature condition over thermal cyclic data. Fig. 6.10 provides us with great information regarding thermal cyclic aging. As it can be seen from this figure, the thermo cyclic aging data are bounded between single aging

conditions. Meaning if we cycle between T_{min} and T_{max} alternatively, the aging results will not exceed the same experiment at T_{min} or T_{max} with the same duration. This finding gave us the idea for homogenization technique.

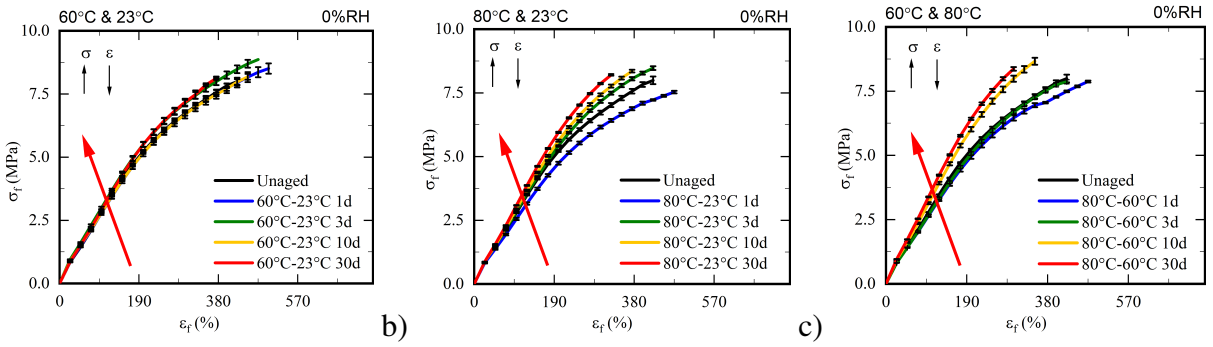

Figure 6.9. Experimental aging data of thermal cyclic between (a) $\theta = 60^oC\&23^oC$, (b) $\theta = 80^oC\&23^oC$, and (c) $\theta = 80^oC\&60^oC$.

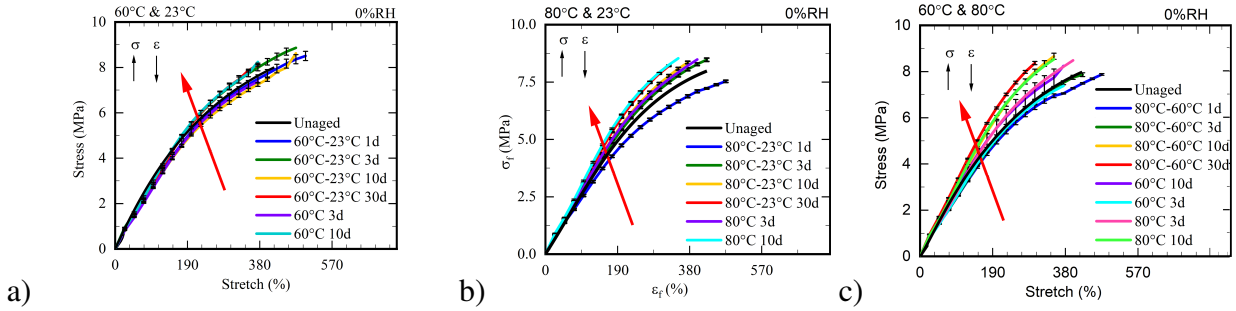

Figure 6.10. Thermo-oxidative aging data over the experimental aging data of thermal cyclic between (a) $\theta = 60^oC$ & 23^oC, (b) $\theta = 80^oC$ & 23^oC, and (c) $\theta = 80^oC$ & 60^oC.

Homogenization technique says that in case of alternating between two conditions over time, one can homogenize the whole process with an equivalent condition over the same period. For instance, in case of thermal cycling between two temperature of T_{min} and T_{max}, the solution would be finding the equivalent temperature that can represent the same effect over time. Now, the important assumption that we find from experimental data comes in to play. The equivalent temperature T_{equ} should be between T_{min} and T_{max}. Searching for a proper function for equivalent temperature yielded Eq. 6.17 as follows

$$T_{equ} = T_{min} + (T_{max} - T_{min}) \times \left(1 - exp\left(-\mu \left(\frac{T_{max} + T_{min}}{T_{max} - T_{min}}\right) t\right)\right), \tag{6.17}$$

where μ is a fitting parameter. Now, using the same formulation as previous section and fitting for thermo-oxidation aging data alone (see Fig. 6.11) one can fine the necessary parameters needed for modeling thermal cyclic aging using Eq. 6.17. Fig. 6.12 shows the prediction of the model for thermal cyclic model.

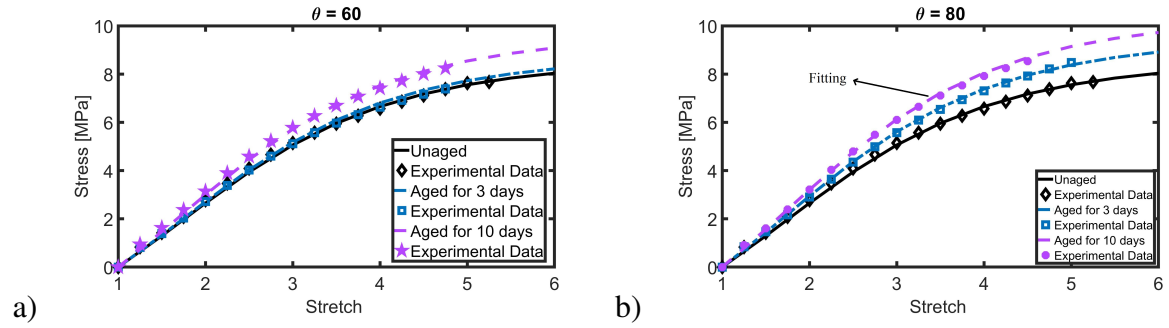

Figure 6.11. Fitting and prediction of thermo-oxidation experimental results (a) at $\theta = 60^oC$, and (b) $\theta = 80^oC$.

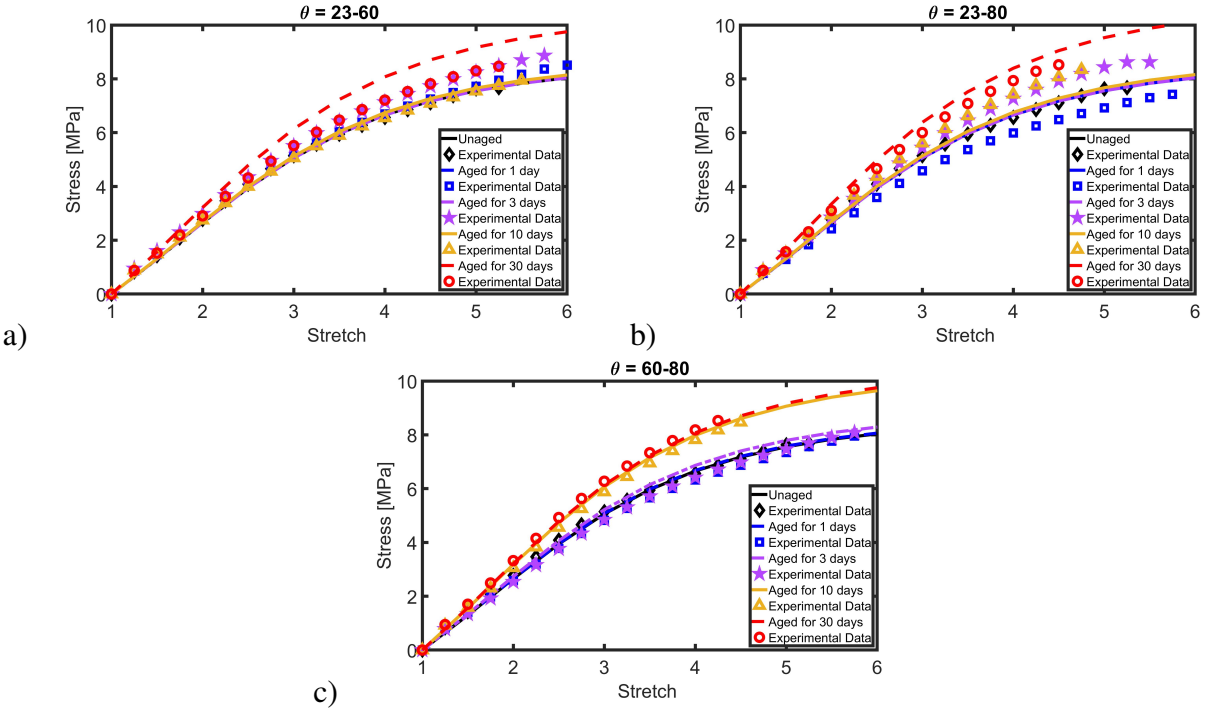

Figure 6.12. Predictions of thermal cyclic model for temperatures between (a) $\theta = 60^oC\&23^oC$, (b) $\theta = 80^oC\&23^oC$, and (c) $\theta = 80^oC\&60^oC$.

CHAPTER 7

SUMMARY AND FUTURE WORKS

The main objectives of this study were to develop a constitutive model for cross-linked polymers during different aging scenarios. In this chapter, the dissertation is briefly summarized for each section. In the first part of this dissertation, an introduction to cross-linked polymers with their applications were presented.

7.1 General Remarks

- In **chapter 4**, the effects of thermo-oxidation on the behavior of cross-linked polymers were studied. Subsequently, an in-depth study on the different decay functions to represent thermo-oxidation has been presented. Later on, combining the concepts of network evolution and dual network hypothesis, a micro-mechanical model to accurately predicting the inelastic behavior of elastomers during aging has been presented. Finally, the model capabilities has been assessed by comparing the model predictions with actual experimental data.

- In **chapter 5**, photo-oxidative aging phenomenon has been studied. Following the same procedure as in **chapter 4**, a micro-mechanical model for predicting the behavior of cross-linked polymers during photo-oxidation has been proposed. The model offers great versatility in capturing different phenomena in both photo- and thermo-oxidative aging. The validity of the model has been proved using our own experimental data.

- In **chapter 6**, the accumulated damage and the effect of one type of aging on the other has

been studied. Later on, cyclic aging conditions taken into account and we have shown the provided model are able to successfully model complicated aging scenarios as well.

7.2 Future Research

The proposed models are not yet complete and they need to be expanded in the future on many different fronts. These expansions are as follow:

- Add the effect of DLO to the proposed model to increase the accuracy of the model for thick samples, especially for the case of photo-oxidation.
- Try to reduce the number of material parameters to increase the capability of the model and its computational efficiency.
- Develop a 3D FEM model to capture complete behavior of polymers during aging.

BIBLIOGRAPHY

BIBLIOGRAPHY

[1] Michael Johlitz, Nico Diercks, and Alexander Lion. Thermo-oxidative ageing of elastomers: A modelling approach based on a finite strain theory. *International Journal of Plasticity*, 63:138–151, 2014.

[2] John A Shaw, Alan S Jones, and Alan S Wineman. Chemorheological response of elastomers at elevated temperatures: experiments and simulations. *Journal of the Mechanics and Physics of Solids*, 53(12):2758–2793, 2005.

[3] Jiří Vohlídal. Polymer degradation: A short review. *Chemistry Teacher International*, 3(2):213–220, 2021.

[4] Jan F Rabek. *Photodegradation of polymers: physical characteristics and applications*. Springer Science & Business Media, 2012.

[5] Mathew C Celina. Review of polymer oxidation and its relationship with materials performance and lifetime prediction. *Polymer Degradation and Stability*, 98(12):2419–2429, 2013.

[6] Kenneth T Gillen, R Bernstein, and M Celina. Challenges of accelerated aging techniques for elastomer lifetime predictions. *Rubber Chemistry and Technology*, 88(1):1–27, 2015.

[7] L Anand. A constitutive model for compressible elastomeric solids. *Computational Mechanics*, 18(5):339–355, 1996.

[8] Mary C Boyce and Ellen M Arruda. Constitutive models of rubber elasticity: a review. *Rubber chemistry and technology*, 73(3):504–523, 2000.

[9] A Dorfmann and Ray W Ogden. A constitutive model for the mullins effect with permanent set in particle-reinforced rubber. *International Journal of Solids and Structures*, 41(7):1855–1878, 2004.

[10] James E Mark and Burak Erman. *Rubberlike elasticity: a molecular primer*. Cambridge University Press, 2007.

[11] Leonard Mullins. Softening of rubber by deformation. *Rubber chemistry and technology*, 42(1):339–362, 1969.

[12] L.R.G. Treloar. *The physics of rubber elasticity*. Oxford University Press, USA, 1975.

[13] Jianyou Zhou, Liying Jiang, and Roger E Khayat. A micro-macro constitutive model for finite-deformation viscoelasticity of elastomers with nonlinear viscosity. *Journal of the Mechanics and Physics of Solids*, 2017.

[14] Vahid Morovati and Roozbeh Dargazany. Improved approximations of non-gaussian probability, force and energy of a single polymer chain. *Physical Review E*, 2019.

[15] Vahid Morovati, Hamid Mohammadi, and Roozbeh Dargazany. A generalized approach to improve approximation of inverse langevin function. In *ASME 2018 International Mechanical Engineering Congress and Exposition*. American Society of Mechanical Engineers, 2018.

[16] RS Rivlin. Large elastic deformations of isotropic materials iv. further developments of the general theory. *Phil. Trans. R. Soc. Lond. A*, 241(835):379–397, 1948.

[17] Raymond William Ogden. Large deformation isotropic elasticity–on the correlation of theory and experiment for incompressible rubberlike solids. *Proc. R. Soc. Lond. A*, 326(1567):565–584, 1972.

[18] E.M. Arruda and M.C. Boyce. A three-dimensional constitutive model for the large stretch behavior of rubber elastic materials. *Journal of the Mechanics and Physics of Solids*, 41(2):389–412, 1993.

[19] Julie Diani, Bruno Fayolle, and Pierre Gilormini. A review on the mullins effect. *European Polymer Journal*, 45(3):601–612, 2009.

[20] Sanjay Govindjee and Juan Simo. A micro-mechanically based continuum damage model for carbon black-filled rubbers incorporating mullins' effect. *Journal of the Mechanics and Physics of Solids*, 39(1):87–112, 1991.

[21] AV Tobolsky, IB Prettyman, and JH Dillon. Stress relaxation of natural and synthetic rubber stocks. *Rubber Chemistry and Technology*, 17(3):551–575, 1944.

[22] R. Dargazany, V.N. Khiêm, and M. Itskov. A generalized network decomposition model for the quasi-static inelastic behavior of filled elastomers. *International Journal of Plasticity*, 63:94, 2015.

[23] R. Dargazany and M. Itskov. Constitutive modeling of the mullins effect and cyclic stress softening in filled elastomers. *Physical Review E*, 88(1):012602, 2013.

[24] Gerhard A. Holzapfel. *Nonlinear Solid Mechanics: A Continuum Approach for Engineering*. John weily & Sons, 2005.

[25] Junuthula Narasimha Reddy. *An introduction to continuum mechanics*. Cambridge university press, 2013.

[26] W Michael Lai, David H Rubin, David Rubin, and Erhard Krempl. *Introduction to continuum mechanics*. Butterworth-Heinemann, 2009.

[27] B. D. Coleman and W. Noll. The thermodynamics of elastic materials with heat conduction and viscosity. *Archive for Rational Mechanics and Analysis*, 13:167, 1963.

[28] B. Coleman and M. E. Gurtin. Thermodynamics with internal state variables. *The Journal of Chemical Physics*, 47:593, 1967.

[29] Craig L Beyler and Marcelo M Hirschler. Thermal decomposition of polymers. *SFPE handbook of fire protection engineering*, 2(7), 2002.

[30] K Horie, Máximo Barón, RB Fox, J He, M Hess, J Kahovec, T Kitayama, P Kubisa, E Maréchal, W Mormann, et al. Definitions of terms relating to reactions of polymers and to functional polymeric materials (iupac recommendations 2003). *Pure and Applied Chemistry*, 76(4):889–906, 2004.

[31] Hans Helmut Gunter Jellinek et al. *Aspects of degradation and stabilization of polymers*. Elsevier Scientific Pub. Co., 1977.

[32] Hayden K Webb, Jaimys Arnott, Russell J Crawford, and Elena P Ivanova. Plastic degradation and its environmental implications with special reference to poly (ethylene terephthalate). *Polymers*, 5(1):1–18, 2012.

[33] Teng Cui. *Mechanical Aging of Thermoset Polymer*. PhD thesis, University of Toronto (Canada), 2016.

[34] JE Guillet. Studies of the mechanism of polyolefin photodegradation. *Pure and Applied Chemistry*, 52(2):285–294, 1980.

[35] Miloš Netopilík, Miroslav Kubín, Jiří Vohlídal, Ivo Kössler, and Pavel KratochvíL. Degradation of polystyrene by shear stress in isopropylphenyl phosphate solution. *Journal of applied polymer science*, 40(7-8):1115–1130, 1990.

[36] HG Barth and FJ Carlin Jr. A review of polymer shear degradation in size-exclusion chromatography. *Journal of liquid chromatography*, 7(9):1717–1738, 1984.

[37] Gottfried W Ehrenstein and Sonja Pongratz. *Beständigkeit von Kunststoffen*. Hanser München, 2007.

[38] Joanne Budzien, Dana R Rottach, John G Curro, Chi S Lo, and Aidan P Thompson. A new constitutive model for the chemical aging of rubber networks in deformed states. *Macromolecules*, 41(24):9896–9903, 2008.

[39] A Lion and M Johlitz. On the representation of chemical ageing of rubber in continuum mechanics. *International Journal of Solids and Structures*, 49(10):1227–1240, 2012.

[40] Akhtar S. Khan, Oscar Lopez-Pamies, and Rehan Kazmi. Thermo-mechanical large deformation response and constitutive modeling of viscoelastic polymers over a wide range of strain rates and temperatures. *International Journal of Plasticity*, 22(4):581 – 601, 2006.

[41] Georges Ayoub, Fahmi Zaïri, Moussa Naït-Abdelaziz, and JM Gloaguen. Modelling large deformation behaviour under loading–unloading of semicrystalline polymers: application to a high density polyethylene. *International Journal of Plasticity*, 26(3):329–347, 2010.

[42] Akhtar Khan and Haoyue Zhang. Finite deformation of a polymer: experiments and modeling. *International Journal of Plasticity*, 17(9):1167–1188, 2001.

[43] Akhtar S Khan, Muneer Baig, Syed Hamid, and Hao Zhang. Thermo-mechanical large deformation responses of hydrogenated nitrile butadiene rubber (hnbr): Experimental results. *International Journal of Solids and Structures*, 47(20):2653–2659, 2010.

[44] Jacques Verdu. *Oxydative ageing of polymers*. John Wiley & Sons, 2012.

[45] Mat Celina, Kenneth T Gillen, and RA Assink. Accelerated aging and lifetime prediction: review of non-arrhenius behaviour due to two competing processes. *Polymer Degradation and stability*, 90(3):395–404, 2005.

[46] Kenneth T Gillen, Mathew Celina, Roger L Clough, and Jonathan Wise. Extrapolation of accelerated aging data-arrhenius or erroneous? *Trends in polymer science*, 8(5):250–257, 1997.

[47] J Wise, KT Gillen, and RL Clough. An ultrasensitive technique for testing the arrhenius extrapolation assumption for thermally aged elastomers. *Polymer Degradation and Stability*, 49(3):403–418, 1995.

[48] Kenneth T Gillen, Mathias Celina, and Michael R Keenan. Methods for predicting more confident lifetimes of seals in air environments. *Rubber chemistry and technology*, 73(2):265–283, 2000.

[49] Kenneth T Gillen, Mathew Celina, and Robert Bernstein. Validation of improved methods for predicting long-term elastomeric seal lifetimes from compression stress–relaxation and oxygen consumption techniques. *Polymer Degradation and Stability*, 82(1):25–35, 2003.

[50] KT Gillen, M Celina, and R Bernstein. Review of the ultrasensitive oxygen consumption method for making more reliable extrapolated predictions of polymer lifetimes. In *ANTEC... conference proceedings*, volume 2, pages 2289–2293. Society of Plastics Engineers, 2004.

[51] Kenneth T Gillen, Robert Bernstein, and Mathew Celina. Non-arrhenius behavior for oxidative degradation of chlorosulfonated polyethylene materials. *Polymer degradation and stability*, 87(2):335–346, 2005.

[52] L Steinke, U Veltin, M Flamm, A Lion, and M Celina. Numerical analysis of the heterogeneous ageing of rubber products. *Constitutive Models for Rubber*, 7:155–160, 2011.

[53] M Celina, J Wise, DK Ottesen, KT Gillen, and RL Clough. Oxidation profiles of thermally aged nitrile rubber. *Polymer Degradation and Stability*, 60(2-3):493–504, 1998.

[54] N Rabanizada, F Lupberger, M Johlitz, and A Lion. Experimental investigation of the dynamic mechanical behaviour of chemically aged elastomers. *Archive of Applied Mechanics*, 85(8):1011–1023, 2015.

[55] RJ Pazur, I Lopez-Carreon, CG Porter, A Herzig, and M Johlitz. Thermal ageing of peroxide-cured nbr, part i: Effect on bulk properties. In *Constitutive Models for Rubber XI: Proceedings of the 11th European Conference on Constitutive Models for Rubber (ECCMR 2019), June 25-27, 2019, Nantes, France*, pages 581–586. CRC Press, 2019.

[56] M. Gigliotti, M. Minervino, M.C. Lafarie-Frenot, and J.C. Grandidier. Effect of thermo-oxidation on the local mechanical behaviour of epoxy polymer materials for high temperature applications. *Mechanics of Materials*, 101:118 – 135, 2016.

[57] R. Behnke and M. Kaliske. Numerical modeling of thermal ageing in steady state rolling tires. *International Journal of Non-Linear Mechanics*, 2018.

[58] T Ha-Anh and Toan Vu-Khanh. Prediction of mechanical properties of polychloroprene during thermo-oxidative aging. *Polymer testing*, 24(6):775–780, 2005.

[59] Michael Johlitz. On the representation of ageing phenomena. *The Journal of Adhesion*, 88(7):620–648, 2012.

[60] Benedikt Dippel, Michael Johlitz, and Alexander Lion. Ageing of polymer bonds: a coupled chemomechanical modelling approach. *Continuum Mechanics and Thermodynamics*, 26(3):247–257, 2014.

[61] Christoph Naumann and Joern Ihlemann. Simulation of oxidative ageing processes in elastomeric components. *KGK-KAUTSCHUK GUMMI KUNSTSTOFFE*, 67(10):68–75, 2014.

[62] C Naumann and J Ihlemann. A dynamic network model to simulate chemical aging processes in elastomers. *Constitutive Models for Rubber IX*, page 39, 2015.

[63] Bruno Musil, Michael Johlitz, and Alexander Lion. On the ageing behaviour of nbr: chemomechanical experiments, modelling and simulation of tension set. *Continuum Mechanics and Thermodynamics*, pages 1–17, 2018.

[64] A Herzig, M Johlitz, RJ Pazur, I Lopez-Carreon, and CG Porter. Thermal ageing of peroxide-cured nbr, part ii: Diffusion-limited oxidation and constitutive modelling. In *Constitutive Models for Rubber XI: Proceedings of the 11th European Conference on Constitutive Models for Rubber (ECCMR 2019), June 25-27, 2019, Nantes, France*, pages 587–592. CRC Press, 2019.

[65] Shabnam Konica and Trisha Sain. A thermodynamically consistent chemo-mechanically coupled large deformation model for polymer oxidation. *Journal of the Mechanics and Physics of Solids*, page 103858, 2019.

[66] C Schlomka, J Ihlemann, and C Naumann. Simulation of oxidative aging processes in elastomer components using a dynamic network model. In *Constitutive Models for Rubber X*, pages 77–82. CRC Press, 2017.

[67] Hamid Mohammadi and Roozbeh Dargazany. A micro-mechanical approach to model thermal induced aging in elastomers. *International Journal of Plasticity*, 118:1–16, 2019.

[68] Hamid Mohammadi and Roozbeh Dargazany. Micro-mechanical model for thermo-oxidative aging of elastomers. In *ASME 2018 International Mechanical Engineering Congress and Exposition*, pages V009T12A028–V009T12A028. American Society of Mechanical Engineers, 2018.

[69] H Mohammadi, A Bahrololoumi, Y Chen, and R Dargazany. A micro-mechanical model for constitutive behavior of elastomers during thermo-oxidative aging. In *Constitutive Models for Rubber XI: Proceedings of the 11th European Conference on Constitutive Models for Rubber (ECCMR 2019), June 25-27, 2019, Nantes, France*, pages 542–547. CRC Press, 2019.

[70] Hamid Mohammadi, Vahid Morovati, Emad Poshtan, and Roozbeh Dargazany. Understanding decay functions and their contribution in modeling of thermal-induced aging of cross-linked polymers. *Polymer Degradation and Stability*, page 109108, 2020.

[71] Amir Bahrololoumi and Roozbeh Dargazany. Hydrolytic aging in rubber-like materials: A micro-mechanical approach to modeling. In *ASME 2019 International Mechanical Engineering Congress and Exposition*. American Society of Mechanical Engineers Digital Collection, 2019.

[72] Amir Bahrololoumi, Vahid Morovati, Emad A. Poshtan, and Roozbeh Dargazany. A multiphysics constitutive model to predict quasi-static behaviour: Hydrolytic aging in thin cross-linked polymers. *International Journal of Plasticity*, 2020.

[73] D Beurle, M , André, U Nackenhorst, and R Desmorat. Micro-mechanically based modelling of homogeneous ageing of elastomers. In *Constitutive Models for Rubber XI: Proceedings of the 11th European Conference on Constitutive Models for Rubber (ECCMR 2019), June 25-27, 2019, Nantes, France*, pages 566–571. CRC Press, 2019.

[74] C. Miehe, S. Göktepe, and F. Lulei. A micro-macro approach to rubber-like materials - part i: the non-affine micro-sphere model of rubber elasticity. *Journal of the Mechanics and Physics of Solids.*, 52:2617, 2004.

[75] Mariacristina Gagliardi, Pietro Lenarda, and Marco Paggi. A reaction-diffusion formulation to simulate eva polymer degradation in environmental and accelerated ageing conditions. *Solar Energy Materials and Solar Cells*, 164:93–106, 2017.

[76] Pellegrino Musto, Giuseppe Ragosta, Mario Abbate, and Gennaro Scarinzi. Photo-oxidation of high performance epoxy networks: correlation between the molecular mechanisms of degradation and the viscoelastic and mechanical response. *Macromolecules*, 41(15):5729–5743, 2008.

[77] Yoichi Kodera and Benjamin J McCoy. Distribution kinetics of radical mechanisms: reversible polymer decomposition. *AIChE journal*, 43(12):3205–3214, 1997.

[78] Kenneth T Gillen, Robert Bernstein, and Dora K Derzon. Evidence of non-arrhenius behaviour from laboratory aging and 24-year field aging of polychloroprene rubber materials. *Polymer Degradation and Stability*, 87(1):57–67, 2005.

[79] Kenneth T Gillen and Roger L Clough. Quantitative confirmation of simple theoretical models for diffusion-limited oxidation. In *Radiation Effects on Polymers*. ACS Publications, 1991.

[80] Kenneth T Gillen and Roger L Clough. Rigorous experimental confirmation of a theoretical model for diffusion-limited oxidation. *Polymer*, 33(20):4358–4365, 1992.

[81] L Audouin, V Langlois, J Verdu, and JCM De Bruijn. Role of oxygen diffusion in polymer ageing: kinetic and mechanical aspects. *Journal of Materials science*, 29(3):569–583, 1994.

[82] J Wise, KT Gillen, and RL Clough. Quantitative model for the time development of diffusion-limited oxidation profiles. *Polymer*, 38(8):1929–1944, 1997.

[83] LM Rincon-Rubio, X Colin, L Audouin, and J Verdu. A theoretical model for the diffusion-limited thermal oxidation of elastomers at medium temperatures. *Rubber chemistry and technology*, 76(2):460–482, 2003.

[84] M Celina and KT Gillen. Advances in exploring mechanistic variations in thermal aging of polymers. In *Service Life Prediction of Polymeric Materials*, pages 45–56. Springer, 2009.

[85] X Colin, C Marais, and J Verdu. Kinetic modelling and simulation of gravimetric curves: application to the oxidation of bismaleimide and epoxy resins. *Polymer Degradation and Stability*, 78(3):545–553, 2002.

[86] F Gugumus. Effect of temperature on the lifetime of stabilized and unstabilized pp films. *Polymer Degradation and Stability*, 63(1):41–52, 1999.

[87] M Celina, AC Graham, KT Gillen, RA Assink, and LM Minier. Thermal degradation studies of a polyurethane propellant binder. *Rubber chemistry and technology*, 73(4):678–693, 2000.

[88] Maristella Gussoni, Fulvia Greco, Marina Mapelli, Alessandra Vezzoli, Elisabetta Ranucci, Paolo Ferruti, and Lucia Zetta. Elastomeric polymers. 2. nmr and nmr imaging characterization of cross-linked pdms. *Macromolecules*, 35(5):1722–1729, 2002.

[89] P.J. Flory. *Statistical Mechanics of Chain Molecules.* Carl Hanser Verlag, Munich., 1989.

[90] L.R.G. Treloar. *The Physics of Rubber Elasticity*. Oxford University Press, 2005.

[91] V Morovati, MA Saadat, S Alazhary, and R Dargazany. A physically motivated model for inelastic response of double network hydrogels. In *Constitutive Models for Rubber XI: Proceedings of the 11th European Conference on Constitutive Models for Rubber (ECCMR 2019), June 25-27, 2019, Nantes, France*, page 92. CRC Press, 2019.

[92] Vahid Morovati, Mohammad Ali Saadat, and Roozbeh Dargazany. Necking of double-network gels: Constitutive modeling with microstructural insight. *Physical Review E*, 102(6):062501, 2020.

[93] M.F. Beatty. An average-stretch full-network model for rubber elasticity. *Journal of Elasticity*, 70:65, 2003.

[94] R. Dargazany. *Multi-Scale Constitutive Modeling of Carbon Black Filled Elastomers*. PhD thesis, Faculty of Mechanical Engineering, RWTH Aachen University, 2011.

[95] Leila Khalili, Vahid Morovati, Roozbeh Dargazany, and jiaqi Lin. Micro-mechanical modeling of visco-elastic behavior of elastomers with respect to time-dependent response of single polymer chains. *Constitutive Models for Rubber X*, 10:523, 2017.

[96] S. Heo and Y. Xu. Constructing fully symmetric cubature formulae for the sphere. *Mathematics of Computation*, 70:269, 2000.

[97] A.E. Ehret, M. Itskov, and H. Schmid. Numerical integration on the sphere and its effect on the material symmetry of constitutive equations- a comparative study. *International Journal for Numerical Methods in Engineering*, 81:189, 2010.

[98] Vahid Morovati, Hamid Mohammadi, and Roozbeh Dargazany. A generalized approach to generate optimized approximations of the inverse langevin function. *Mathematics and Mechanics of Solids*, 24(7):2047–2059, 2019.

[99] Vahid Morovati, Jiaqi Lin, Roozbeh Dargazany, Weiyi Lu, and Mahdi Moghimi Zand. A micro-mechanical model for inelastic response of double network hydrogels. *Journal of the Mechanical Behavior of Biomedical Materials*, 109:266–277, 2017 (submitted).

[100] R. Dargazany and M. Itskov. A network evolution model for the anisotropic Mullins effect in carbon black filled rubbers. *International Journal of Solids and Structures*, 46:2967, 2009.

[101] R. Dargazany, V.N. Khiêm, U. Navrath, and M. Itskov. Network evolution model of anisotropic stress softening in filled rubber-like materials; parameter identification and finite element implementation. *Journal of Mechanics of Materials and Structures*, 7(8):861, 2013.

[102] Ricardo Baumhardt-Neto and Marco-A De Paoli. Mechanical degradation of polypropylene: effect of uv irradiation. *Polymer degradation and stability*, 40(1):59–64, 1993.

[103] AP Gupta, UK Saroop, and Vidya Gupta. Studies on the photo-oxidation of pp and pp/mlldpe blend systems: Thermal, physicochemical, and mechanical behavior. *Journal of applied polymer science*, 106(2):917–925, 2007.

[104] H Aglan, M Calhoun, and L Allie. Effect of uv and hygrothermal aging on the mechanical performance of polyurethane elastomers. *Journal of applied polymer science*, 108(1):558–564, 2008.

[105] J-F Larché, P-O Bussière, and J-L Gardette. Photo-oxidation of acrylic-urethane thermoset networks. relating materials properties to changes of chemical structure. *Polymer degradation and stability*, 96(8):1438–1444, 2011.

[106] Grégory Mertz, Fatima Hassouna, Philippe Leclère, Abdesselam Dahoun, Valérie Toniazzo, and David Ruch. Correlation between (nano)-mechanical and chemical changes occurring during photo-oxidation of filled vulcanised styrene butadiene rubber (sbr). *Polymer degradation and stability*, 97(11):2195–2201, 2012.

[107] Pierre-Olivier Bussiere, Agnes Rivaton, Sandrine Thérias, and Jean-Luc Gardette. Multiscale investigation of the poly (n-vinylcarbazole) photoageing mechanism. *The Journal of Physical Chemistry B*, 116(2):802–812, 2012.

[108] Rudinei Fiorio, Sara Villanueva Díez, Alberto Sánchez, Dagmar R D'hooge, and Ludwig Cardon. Influence of different stabilization systems and multiple ultraviolet a (uva) aging/recycling steps on physicochemical, mechanical, colorimetric, and thermal-oxidative properties of abs. *Materials*, 13(1):212, 2020.

[109] GE Schoolenberg. A fracture mechanics approach to the effects of uv-degradation on polypropylene. *Journal of materials science*, 23(5):1580–1590, 1988.

[110] GE Schoolenberg and HDF Meijer. Ultra-violet degradation of polypropylene: 2. residual strength and failure mode in relation to the degraded surface layer. *Polymer*, 32(3):438–444, 1991.

[111] D Benachour and CE Rogers. Effect of deformation on the photodegradation of low density polyethylene. In *ABSTRACTS OF PAPERS OF THE AMERICAN CHEMICAL SOCIETY*, volume 183, pages 70–POLY. AMER CHEMICAL SOC 1155 16TH ST, NW, WASHINGTON, DC 20036, 1982.

[112] Jiří Czernỳ. Thermo-oxidative and photo-oxidative aging of polypropylene under simultaneous tensile stress. *Journal of Applied Polymer Science*, 16(10):2623–2632, 1972.

[113] Ricardo Baumhardt-Neto and Marco-Aurelio De Paoli. Photo-oxidation of polypropylene under load. *Polymer degradation and stability*, 40(1):53–58, 1993.

[114] B O'donnell and JR White. Stress-accelerated photo-oxidation of polypropylene and glass-fibre-reinforced polypropylene. *Polymer degradation and stability*, 44(2):211–222, 1994.

[115] Li Tong and JR White. Photo-oxidation of thermoplastics in bending and in uniaxial compression. *Polymer degradation and stability*, 53(3):381–396, 1996.

[116] C Rouillon, P-O Bussiere, E Desnoux, S Collin, C Vial, S Therias, and J-L Gardette. Is carbonyl index a quantitative probe to monitor polypropylene photodegradation? *Polymer Degradation and Stability*, 128:200–208, 2016.

[117] Xuan Liu, Xiao-Peng Ren, and Rui Yang. Infectious behavior in photo-oxidation of polymers. *Chinese Journal of Polymer Science*, 38(3):248–256, 2020.

[118] Halina Kaczmarek. Photodegradation of polystyrene and poly (vinyl acetate) blends—ii. irradiation of ps/pvac blends by fluorescent lamp. *European polymer journal*, 31(12):1175–1184, 1995.

[119] Halina Kaczmarek, Renata Drag, Małgorzata Świątek, and Dagmara Ołdak. The influence of uv-irradiation on poly (vinyl chloride) modified by poly (vinyl acetate). *Surface science*, 507:877–882, 2002.

[120] Kenneth T Gillen and Roger L Clough. Time-temperature-dose rate superposition: a methodology for extrapolating accelerated radiation aging data to low dose rate conditions. *Polymer Degradation and Stability*, 24(2):137–168, 1989.

[121] Kenneth T Gillen and Roger L Clough. Predictive aging results in radiation environments. *Radiation Physics and Chemistry*, 41(6):803–815, 1993.

[122] Kenneth T Gillen and Mathew Celina. Predicting polymer degradation and mechanical property changes for combined radiation-thermal aging environments. *Rubber Chemistry and Technology*, 91(1):27–63, 2018.

[123] L Audouin, S Girois, L Achimsky, and J Verdu. Effect of temperature on the photooxidation of polypropylene films. *Polymer degradation and stability*, 60(1):137–143, 1998.

[124] Sarah Chinn, Steve DeTeresa, April Sawvel, Al Shields, Bryan Balazs, and Robert S Maxwell. Chemical origins of permanent set in a peroxide cured filled silicone elastomer–tensile and 1h nmr analysis. *Polymer degradation and stability*, 91(3):555–564, 2006.

[125] A Maiti, RH Gee, T Weisgraber, S Chinn, and RS Maxwell. Constitutive modeling of radiation effects on the permanent set in a silicone elastomer. *Polymer degradation and stability*, 93(12):2226–2229, 2008.

[126] Takato Ishida, Ryoma Kitagaki, Hideaki Hagihara, and Yogarajah Elakneswaran. Challenges in prediction of significant structural changes during photochemical "degelation" of acrylic-urethane network. *Polymer*, 186:122035, 2020.

[127] E.M. Arruda and M.C. Boyce. A three-dimensional constitutive model for the large stretch behavior of rubber elastic materials. *Journal of the Mechanics and Physics of Solids.*, 41:389, 1993.

[128] J. Diani, M. Brieu, and J.M. Vacherand. A damage directional constitutive model for Mullins effect with permanent set and induced anisotropy. *European Journal of Mechanics A-Solids*, 25:483, 2006.

[129] W. Kuhn and F. Grün. Statistical behavior of the single chain molecule and its relation to the statistical behavior of assemblies consisting of many chain molecules. *Journal of Polymer Science Part A: Polymer Chemistry*, 1(3):183–199, 1946.

[130] G. Marckmann, E. Verron, L. Gornet, G. Chagnon, P. Charrier, and P. Fort. A theory of network alteration for the Mullins effect. *Journal of the Mechanics and Physics of Solids.*, 50:2011, 2002.